ORGANIC AND HYBRID OPTOELECTRONIC DEVICES: UNDERSTANDING KEY LOSS MECHANISMS.

James William Ryan

Dipòsit Legal: T 277-2015

UNIVERSITAT ROVIRA I VIRGILI
ORGANIC AND HYBRID OPTOELECTRONIC DEVICES: UNDERSTANDING KEY LOSS MECHANISMS.
James William Ryan
Dipòsit Legal: T 277-2015

UNIVERSITAT ROVIRA I VIRGILI
ORGANIC AND HYBRID OPTOELECTRONIC DEVICES: UNDERSTANDING KEY LOSS MECHANISMS.
James William Ryan
Dipòsit Legal: T 277-2015

James William Ryan

Organic and Hybrid Optoelectronic Devices: Understanding Key Loss Mechanisms

Doctoral Thesis

Supervised by Prof. Emilio Palomares Gil

Institut Català d'Investigació Química

UNIVERSITAT ROVIRA I VIRGILI

Tarragona

2013

UNIVERSITAT ROVIRA I VIRGILI
ORGANIC AND HYBRID OPTOELECTRONIC DEVICES: UNDERSTANDING KEY LOSS MECHANISMS.
James William Ryan
Dipòsit Legal: T 277-2015

Emilio Palomares Gil, Group Leader at the Institute of Chemical Research of Catalonia (ICIQ), Tarragona and Research Professor at the Catalan Institution for Research and Advanced Studies (ICREA), Barcelona.

CERTIFIES:

That the present research study, entitled “Organic and Hybrid Optoelectronic Devices: Understanding Key Loss Mechanisms” presented by James William Ryan for the award of the degree of Doctor, has been carried out under my supervision in ICIQ and that he fulfills the requirements to obtain the degree with “International Distinction”

Tarragona May 2013

Prof. Dr. Emilio Palomares Gil

UNIVERSITAT ROVIRA I VIRGILI

ICIQ
Institut Català d’Investigació Química

UNIVERSITAT ROVIRA I VIRGILI
ORGANIC AND HYBRID OPTOELECTRONIC DEVICES: UNDERSTANDING KEY LOSS MECHANISMS.
James William Ryan
Dipòsit Legal: T 277-2015

Table of Contents

Chapter 1 Introduction

Chapter 2 Experimental Procedures

Chapter 3 The Effect of Donor Layer Thickness and a MoO_3 Hole Transport Layer on Device Performance in Squaraine/C_{60} Bilayer Solar Cells

Chapter 3 (cont.)

Chapter 4 Small Molecule Solar Cells Based on a Series of Water Soluble Zinc Phthalocyanine Donors

Chapter 5 The Origin of the Open-Circuit Voltage in Hybrid PbS Quantum Dot/C60 Bilayer Solar Cells

Chapter 6 Towards Low-Temperature Preparation of Hybrid Light-Emitting Diodes

Dedicated to Mam, Dad, Paul and Asami

UNIVERSITAT ROVIRA I VIRGILI
ORGANIC AND HYBRID OPTOELECTRONIC DEVICES: UNDERSTANDING KEY LOSS MECHANISMS.
James William Ryan
Dipòsit Legal: T 277-2015

Chapter 1
Introduction

1. Motivation

Energy is one of the biggest challenges facing society in the 21st century.[1,2] Over the past century society has grown exponentially and has relied heavily on the combustion of fossil fuels to attain the energy required to drive industry, and facilitate everyday requirements such as generating light and heat. However, this is not a sustainable approach, as fossil fuels are a limited resource.[3] Furthermore, the burning of fossil fuels has adverse affects on the environment.[4,5] Alternative energy sources are clearly required to meet the goals of renewable, sustainable and environmentally friendly energy.[3,6,7] Nuclear energy a realistic alternative to fossil fuels, however it has severe dangers associated with it, highlighted by the disasters at Chernobyl, Three Mile Island and, more recently, Fukushima nuclear power plants. Reducing the reliance on both fossil fuels and nuclear energy by replacing them with renewable energy sources is therefore critical for reducing the damage imposed on the environment and providing future generations a habitable planet.

Renewable energy sources (RES) such as solar, tidal, geothermal, biofuels and wind provide appealing alternatives to fossil fuels and nuclear energy.[7-10] Current RES supply approximately 14% of the total world energy demand. This percentage is due to increase with governments now accepting the need for renewable energy sources based on a combination of environmental, economic, societal and political concerns.[3,7,11-14] Regardless of motivation, RES are generating more attention,

promising minimal environmental impact and secondary wastes, and offering sustainable energy based on the current, and ideally future, economic needs.[15] Of the different RES available, solar energy is by far the most abundant, so plentiful in fact that in one hour the sun provides enough energy to power society's needs for one year.[16] It is no surprise therefore that nature takes advantage of this in the form of photosynthesis, with plants and bacteria doing so for the past three billion years.

Together with the need for renewable and sustainable sources for generating electricity, there also exists the need to reduce energy consumption on the whole, using more efficient technologies. Moreover, next-generation technologies should ideally be comprised of affordable earth abundant materials and demand limited energy to be produced in order to ensure economic and environmentally sustainability.[17] Lighting represents a key area where such technology prove crucial, as it is consumes a significant portion of the total energy bill yet does so by predominantly inefficient methods. The incandescent light-bulb is a perfect example, with only 5% of the electricity consumed being used to light the bulb, with the other 95% of electricity being lost to heat. Very recently the use of this incandescent light bulbs has been phased out in Europe, with further restrictions due to be introduced over the coming years.[18] Although, the issue of efficiency is being dealt with, several environmental concerns still exist.[19-21]

Organic semiconductors are promising materials for addressing these key energy challenges as they are earth-abundant materials that can be utilized efficiently to either generate energy in the form of electricity or in the opposite manner can emit light through an applied bias.[22,23] Organic semiconductors also have very favourable material properties that lend themselves to low-cost and high throughput fabrication methods.[24-26]

2. Solar Energy

The sun is a tremendous source of energy, supplying the earth with 120,000 terawatts per annum, which is 10,000 times more energy than is used on earth in the same time span. This energy can be utilized in the form of heat,[27] direct electricity,[28] or it can be stored in the form of gas,[29] or chemical bonds.[30] Nature has elegantly utilized the sun's energy through photosynthesis for over 3 billion years to harvest its ubiquitous energy supply and over time has perfected the process. Mankind in comparison to nature is new to the field of harnessing the sun's energy. The first realization of light generating electricity was in 1839 with Becquerel's discover of the photovoltaic effect, where he found that electrodes in an acidic solution can generate current by shining light on them, in particular ultraviolet light.[31] The photovoltaic effect, where a photon of energy is directly converted into electricity is the most advance form of solar energy generation. Following Becquerel's discovery, other approaches were taken to utilise the photovoltaic effect but none led to high power conversion efficiencies.[32] That is until 1954 when researchers at Bell laboratories produced a solar cell based on a diffused Si p-n junction with a power conversion efficiency (PCE) of 6%.[33] Since then improvements have seen single crystal Si (*c*-Si) solar cells reach efficiencies of ~26%, multicrystalline and amorphous Si (*m*-Si and *a*-Si, respectively) solar cells have also been studied in great detail with efficiencies scaling downwards with fabrication costs, PCE ~21% and ~13% respectively.[34-37] *a*-Si, while having significantly lower efficiency does have the advantage of producing thin film solar cells *via* roll-to-roll (R2R) methods, which significantly reduces fabrication costs. Other inorganic solar cells (ISCs) have also shown much promise, *for example*, CdTe and $Cu(InGa)Se_2$.[38,39] However, serious drawbacks exist for these devices as they present environmental concerns and use rare-earth materials.[40,41] Organic semiconductors on the other hand are earth-abundant and non-toxic and offer the potential to increase their efficiencies beyond that of *a*-Si.

2.1 Organic Solar Cells

2.1.1 Overview

In 1986 C.W Tang published the first heterojunction organic solar cell (OSC) and since then the design principles have changed very little.[42] Previous attempts at using organic molecules at photovoltaic material had focused on similar device architectures as inorganic materials, which proved unsuccessful, due to the low dielectric constant of organic molecules. The active layer materials employed by Tang were CuPc as the donor layer and a perylene tetracarboxylic derivative as the acceptor, with the devices producing a photo-conversion efficiency of approximately 1%. Although the first example used small molecule donor and acceptors it would be polymer donors together with fullerene acceptors that would go on to dominate the field until very recently. Before 2007, evaporated devices using small molecule donors had achieved less than 2% PCE and received little attention.[43] Furthermore, little progress had been made for solution processable small molecules due to a difficulty in forming good film morphologies when blended with fullerene derivatives.[44] However, since then the field of small molecule organic solar cells has really taken off, with efficiencies now approaching 7%,[45,46] polymer:fullerene devices in comparison have also improved in efficiency, exceeding 9%,[47] but the gap is certainly closing. Small molecules also offer several advantages over polymers such as facile synthesis and purification methods, highly tunable optical properties, mono-dispersity and reproducibility.[48,49] The final two points being key limitations of polymer semiconductors whose properties usually change from batch to batch due to difficulties in controlling the chain length. Also within in each batch there is a range of chain lengths, such poly-dispersity does not exist in the case of small molecules. Polymers are also limited to solution processing as the high temperatures used for sublimation required will degrade the polymer, while small molecules can be solution processed and/or vacuum processed via sublimation

depending on their configuration. A disadvantage of sublimation however is the higher costs involved in making and breaking vacuum, although it must be noted that industry is developing large scale assembly lines which can bring the costs down significantly. Vacuum processing also eliminates the use of solvents (typically organic chlorinated solvents) from the assembly line and gives rise to purer and more reproducible active layers.

2.1.2 Photogeneration in Organic Semiconductors

The main difference between organic and inorganic solar cells lies in the manner in which charges are generated under illumination. Organic semiconductors have inherently small dielectric constants in comparison to inorganic semiconductors and it is this difference that strongly dictates the charge generation mechanism for each type of device. For a conventional inorganic semiconductor (CSC), when a photon is absorbed, free charge carriers are generated simultaneously while for organic semiconductors, the Coloumbically bound electron-hole pair (exciton) is generated. Here we will refer to an organic semiconductor as an excitonic semiconductor (XSC) to prevent confusing it with the abbreviation for an organic solar cell (OSC). For either type of semiconductor the attraction between the photogenerated electron-hole pair has the potential energy:

$$V = \frac{q^2}{4\pi\varepsilon_r\varepsilon_0 r_C} \qquad \textbf{(1)}$$

where q is the electronic charge, ε_r is the dielectric constant of the material, ε_0 is the vacuum permittivity (8.85 x 10^{-12} C^2 J^{-1} m^{-1}), and r_C is the critical distance between the two charges. When V is less than the thermal energy of the carrier, k_BT, then the charge carriers will have enough energy to separate. Organic semiconductors have inherently small dielectric constants which leads to a small

value for V. Inorganic semiconductors on the other hand have sufficiently high dielectric constants leading to V being less than k_BT and thus allowing free charge carrier generation.

The nature of the chemical bonds in CSCs and XSCs also differs and has consequences on device operation. CSCs are highly ordered with atoms bound by strong covalent bonds that extend in three dimensions. This high degree of order leads to a highly delocalised electron wave function. Organic semiconductors on the other hand, have weak van der Waals forces acting between neighbouring molecules, which leads to the electron wave function being highly localised on individual molecules.[50] The bonding orbitals also differ between organic and inorganic semiconductors, with organic semiconductors being tightly bound and relying on p to p* transitions. Inorganic semiconductors are generally elements from the 3rd-5th row of the periodic table, meaning the electrons are not as strongly bound. These differences influence the Bohr radius, r_B, of each respective material.

The Bohr radius of the lowest electronic state of a semiconductor with hydrogen-like wavefunctions (Si, *for example*) is:

$$r_B = r_0 \varepsilon_r \left(\frac{m_e}{m_{eff}} \right) \qquad \textbf{(2)}$$

where, r_0 is the Bohr radius for a hydrogen atom in its ground state (0.53 Å), m_e is the mass of a free electron in vacuum and m_{eff} is the effective mass of the electron in the semiconductor. Typically m_{eff} is less than m_e in CSCs but greater than m_e in XSCs. The effective mass decreases as the carrier becomes more delocalised and its transport more wave-like. The larger effective mass as well as

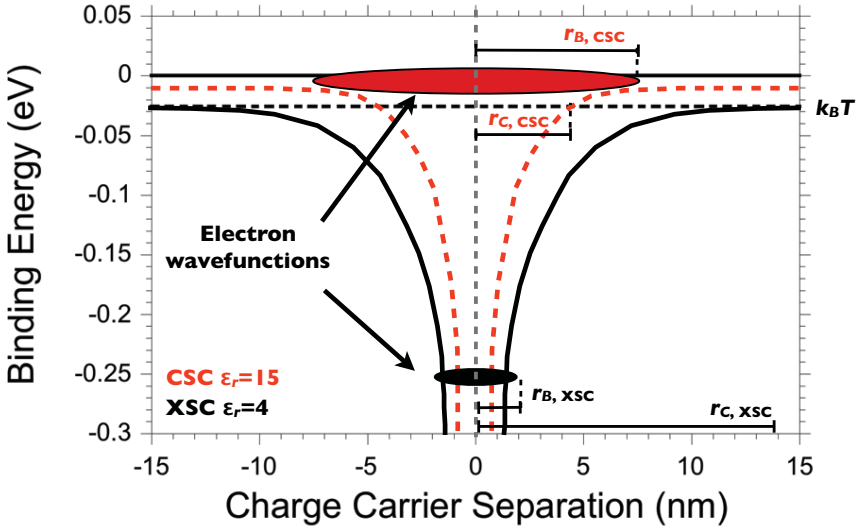

Figure 1 A schematic illustration of the differences between CSCs and XSCs. The key points being that the electronic wave functions and critical radius of charge carrier separation differ considerably. The result is that γ is considerably less than 1 for a CSC and considerably larger than 1 for an XSC.

the higher dielectric constant of CSCs leads to r_B values significantly larger than XSCs.

Gregg has presented an easy way to distinguish between conventional and excitonic semiconductors by considering the Bohr radius of the lowest electronic state and the critical distance between the two charges after photogeneration(both are plotted schematically in Figure 1.[51] The critical distance is obtained by rearranging Equation 1, with V equal to k_BT:

$$r_C = \frac{q^2}{4\pi\varepsilon_r\varepsilon_0 k_B T} \qquad \textbf{(3)}$$

A quantity γ is assigned to determine whether a semiconductor behaves as a conventional or excitonic semiconductor:

$$\gamma = \frac{r_c}{r_B} \approx \left(\frac{q^2}{4\pi e_r k_B r_0 m_e}\right)\left(\frac{m_{eff}}{\varepsilon^2 T}\right) \quad \textbf{(4)}$$

Where γ > 1 indicates an excitonic semiconductor and γ < 1 indicates a conventional semiconductor.

Attempts at using organic semiconductors in solar cells had originally focused on using them in Schottky cells,[52] but to no great success due to the difficulty in separating the exciton into free charges. Nature however has a way of separating the charges extremely successfully through the use of donor-acceptor pairs, where a sufficient offset in energy levels between the donor and acceptor molecules exists to separate the strongly bound charges into free carriers.[30] The same basic idea has been employed in OSCs to great success, starting from Tang's first demonstration in 1986 using a donor/acceptor type II (staggered) heterojunction. Figure 2 compares the architecture and energy respective energy levels of a Schottky cell with a type II heterojunction. Having now introduced the principle differences between organic and inorganic semiconductors in terms of charge generation, the basic operating principles of organic solar cells can be explained.

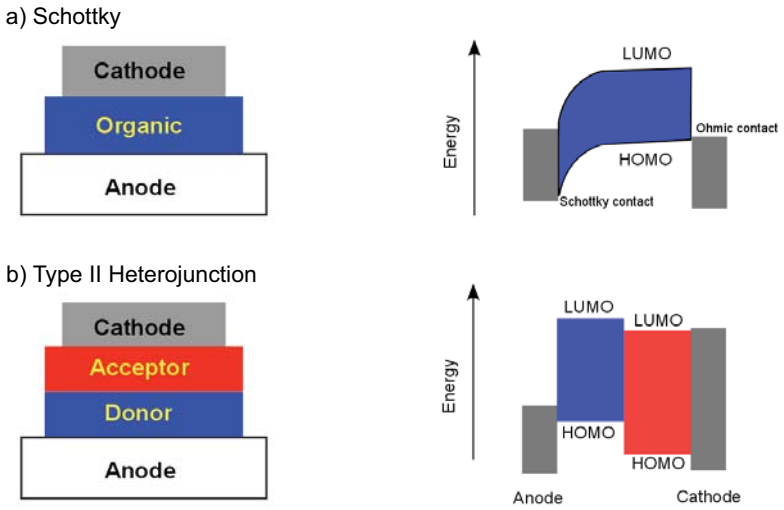

Figure 2 Schematic diagram of a) Schottky-type diode and b) type-II heterojunction comprising of a electron donor and electron acceptor layer. The key requirement for electron transfer is that the difference in both LUMO energies exceeds the binding energy of the exciton.

2.1.3 Organic Solar Cell Device Operation

The operating mechanism of an organic solar cell is a multi-step process. Here we describe the basic device operation of organic solar cells. For convenience sake we describe the steps a donor molecule undergoes, but the same process also occurs for the acceptor, albeit that the acceptor donates a hole to the donor. An OSC thus operates in the following manner, which is also illustrated in Figure 3:

1) Absorption of a photon and generation of an exciton
2) Migration of the exciton to the donor-acceptor interface
3) Charge separation
4) Charge Collection at respective electrode

Competing processes also occur during the abovementioned steps that lead to losses in efficiency.

1) Geminate recombination – the exciton has a limited lifetime, if it cannot reach a donor/acceptor interface in time it will then recombine
2) No injection – if the offset between the excited state energy of the donor and electron affinity of the acceptor is not sufficient there will be no injection, leaving the electron to decay to its ground state
3) Non-geminate recombination – after charge separation the free electron can still recombine with a hole at the donor-acceptor interface.
4) Non-geminate recombination during transport – if the film has any defects or trap states the free charges may combine with them
5) Surface recombination – depending on the device architecture and film nanostructure (i.e. presence of pinholes) charges may recombine at the wrong electrode

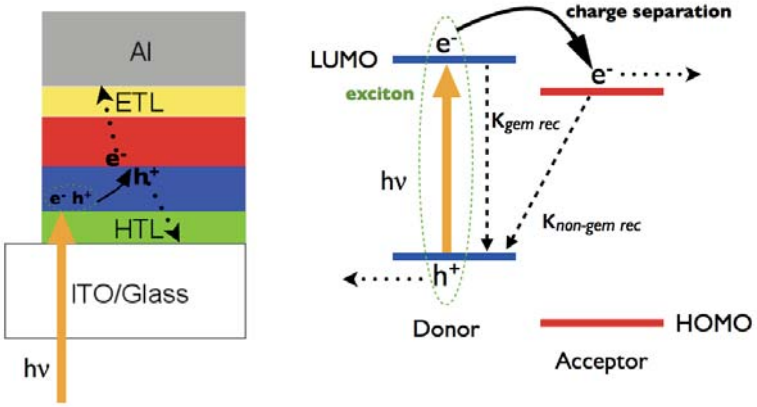

Figure 3 Schematic description of the charge generation, transport and separation processes that occur in photocurrent generation. Also depicted are the key loss processes, geminate and non-geminate (bimolecular) recombination.

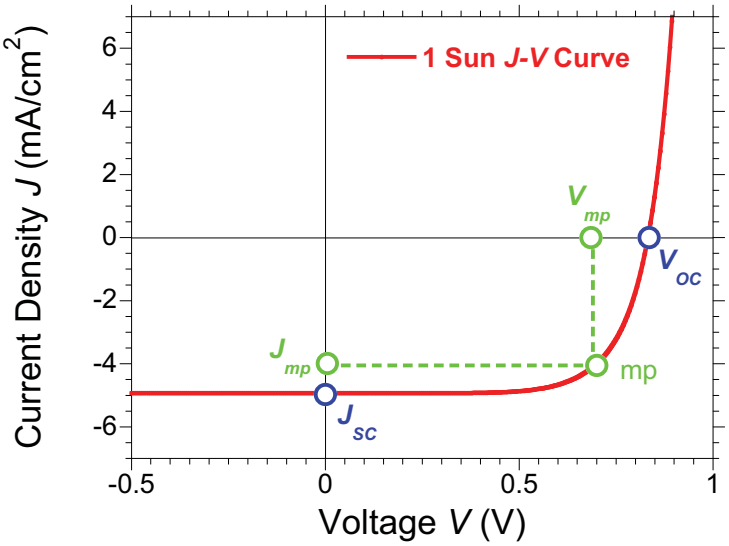

Figure 4 Typical *JV* curve showing the figures of merit used to calculate the device efficiency. V_{OC} and J_{SC} correspond to the open-circuit voltage and short-circuit current respectively. The fill factor is calculated using the voltage and current density values at the devices maximum power coordinate.

The current-voltage behavior of a solar cell under illumination is illustrated in Figure 4, showing the key figures of merit. The photoconversion efficiency (η) is calculated using the following formula:

$$\eta = \frac{V_{OC} * J_{SC} * FF}{P_{In}} \qquad \textbf{(5)}$$

where, J_{SC} is the current density at short-circuit, V_{OC} is the open circuit voltage, FF is the fill factor, which is a measure of squareness of the *J-V* curve and P_{In} is the incident power of the lamp. The J_{SC} of the device is determined by the absorption properties of the active layer and can be affected by geminative losses, extraction problems, or mis-alignment of the donor-acceptor energy levels that can prevent

charge separation at the donor/acceptor interface. The FF is determined from the ratio of the current density times the voltage at the maximum power point divided by J_{SC} times V_{OC}:

$$FF = \frac{V_{mp} * J_{mp}}{V_{OC} * J_{SC}} \quad \textbf{(6)}$$

The FF can be limited by several reasons, such as a miss-match in charge carrier mobilities of the donor and acceptor material, large series resistance (R_s) or low parallel (shunt) resistance (R_p), poor contacts or recombination (geminate and/or non-geminate).[53-57]

The V_{OC} is perhaps the most debated figure of merit in OSCs, with its origins still under discussion.[58-61] Unlike inorganic solar cells, the V_{OC} in OSCs is in general field independent, with the origin of the V_{OC} determined by the potential energy differences at the donor/acceptor interface, together with the kinetics of the charge carriers. The potential energy at the donor/acceptor interface derives from the differences between the highest occupied molecular orbital (HOMO) of the donor and lowest unoccupied molecular orbital (LUMO) of the acceptor. By definition the V_{OC} is the voltage at which no net-current flows (I = 0 A) but there is of course current being generated within the device, but this photocurrent is being balanced by recombination current in the device. The recombination rate scales with the equilibrium charge carrier concentrations and therefore exponentially with the energy levels, with changes in energetics having a large influence on V_{OC}. Simply the more charge we generate, the faster the charges recombine. Increasing applied bias, leads to an increase in potential energy within the device and thus an increase in the recombination current. Recent studies have shown that the V_{OC} can be

accurately estimated in OSCSs by simply taking into account the flux of photogenerated charges and the flux of charge recombining non-geminately:[62-64]

$$J_{tot} = J_{gen} + J_{loss} \quad \textbf{(7)}$$

where, J_{gen} is the generation current density, which in a device with neglible field-dependent generation can be assumed to be J_{SC} and J_{loss} is the current density lost to non-geminate recombination. J_{loss} is obtained by considering the ratio between the charge carrier density, n, and the charge carrier lifetime τ_n:

$$J_{loss} = \frac{edn}{\tau_n} \quad \textbf{(8)}$$

where e is the elementary charge and d is the active layer thickness. This simple approximation is important in understanding the importance of charge carrier kinetics has on controlling the open-circuit voltage.

2.1.4 Device Architecture

OSCs rely on the use of a donor-acceptor interface to separate the photogenerated charges and generating photocurrent.[65] In the above description of OSCs we have presented a very simple bilayer structure, but this provides very limited interfacial area for charge separation to occur. Increasing the interfacial area should allow improved free charge generation and higher photocurrents. Several different options are available regarding device architecture,[65] with the principle examples illustrated in Figure 5. First lets look at the classic bilayer or planar heterojunction (PHJ) device. The advantage of a bilayer device is that the photogenerated exciton can migrate to the interface in a facile manner, undergo charge separation and the electron (hole) can be transported through a pure acceptor (donor) layer to the cathode (anode), leaving very few problems in charge generation or charge

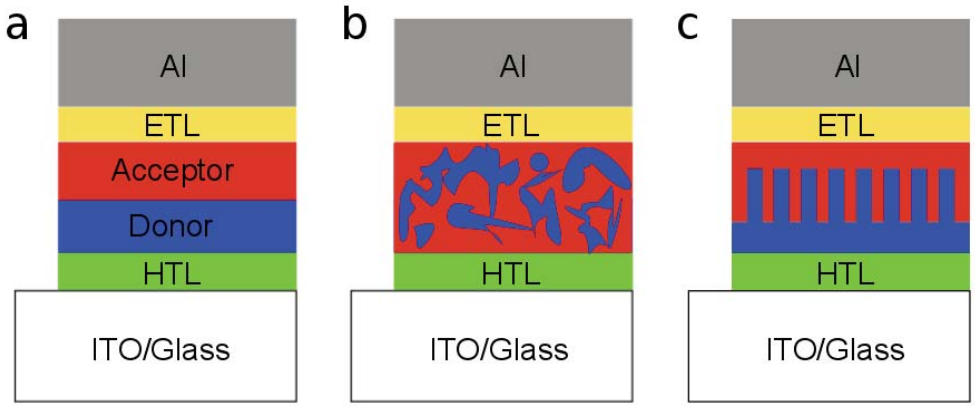

Figure 5 Illustration of the three of the principle device architectures in OSCs: a) Planar-, b) bulk- and c) ordered-heterojunction. Here we depict aluminium as the cathode and ITO as the transparent anode.

collection. However, the typical exciton diffusion length of an organic molecule is extremely low, being on the order of 10 nm. This is significantly lower than the thickness required for an organic film to absorb all of the sun's photons, typically 1 μm. This means that any exciton generated more than 10 nm away from the donor/acceptor interface will recombine before reaching the interface.

Bulk heterojunction (BHJ) morphologies provide a route towards higher photocurrents through intermixing the donor and acceptor components in order to maximize the interfacial area.[25,66,67] Most commonly BHJ devices are solution processed but they can also be processed through co-evaporation.[46,68] Focusing first on solution processed BHJs, both molecules are processed from the same solution so they must both be compatible and have good solubility in the solvent of choice. Furthermore, the solvent must allow for good phase separation between the two materials so that donor-rich domains and acceptor-rich domains are formed. It is also possible to have one molecule form well-defined domains and be surrounded by a matrix of the other molecule. The dimensions of the domains should ideally

be on the order of the exciton diffusion length so that every photogenerated exciton is close enough to a donor-acceptor interface. Also, the morphology of the active layer must provide pathways between the donor/acceptor interface and each respective electrode. Having good pathways between each domain and its respective electrode allows the use of thicker films than those used for bilayers, which allows more light to be absorbed and if there are no collection problems, higher photocurrent. A side effect of having a higher interfacial area is that there will be more free charge carriers generated in a three dimensional space, providing a higher rate of bimolecular recombination. In a PHJ on the other hand, the charges are only generated at a defined surface, and are extracted rapidly due to the device architecture and the free pathway to the electrodes. This has recently been demonstrated comparing evaporated PHJ and BHJ devices.[69,70] Surface recombination is also a big issue for BHJ devices so the use of an electron transport layer (ETL) and hole transport layer (HTL) is of great importance as the donor and acceptor domains will be in contact with the "wrong" electrode, increasing the chance charges recombining at the wrong electrode. The term blocking layer rather than transport layer is more appropriate for these layers as their role is to act as a barrier or selective membrane to prevent unwanted charges reaching the electrode. One approach to isolate BHJ from the electrodes is to employ a p-*i*-n structure, where a thin layer of donor is placed between the anode and the BHJ, while a thin acceptor layer of the acceptor is placed between the cathode and the BHJ. The thin p and n layers can thus act as barriers for surface recombination as well as contribute to the photocurrent. This architecture that combines both PHJ and BHJ principles has led to high efficiencies recently with evaporated small molecule based OSCs.[46,71]

The most common HTL is PEDOT:PSS,[72] while transition metal oxides (TMO) are also a popular choice,[73] especially MoO_3,[74] as well as V_2O_5,[75] and NiO.[76] In a

bilayer device, the most commonly used ETL is bathocuproine (BCP).[77,78] The role of BCP is to protect C_{60} from the metal contact, as the metal can induce gap states in the C_{60}. Interestingly, mid-gap states are also produced in BCP but in this case they act to facilitate electron transport between C_{60} and the metal contact.[78]

Obtaining a well-structured BHJ is not trivial, as it is difficult to control the domain size of both donor and acceptor. As they are processed together it is also extremely challenging as they must have similar solubility in a given solvent, and phases separate in the required manner. Several parameters must be optimized such as solvent, concentration, processing methods and settings, as well as the post-deposition techniques such as annealing either *via* a thermal or solvent vapour method, or a combination of both. Thermal annealing involves heating the film or complete device at a certain temperature to allow one or both components to arrange in a more favourable configuration.[72,79-81] Here the molecules may adopt different packing geometries and/or become crystalline, domain sizes can grow and even the surface energy can change.[82,83] The reason for the changes is that after spin-coating the molecules are "frozen" in a morphology that is not energetically favourable, while the free energy available to the system at room temperature is not sufficient to overcome this unfavourable situation. Applying heat therefore can increase the amount of free energy sufficiently and improve the films electronic properties. Solvent vapour annealing (SVA) induces similar effects,[84] and is done by immersing the films in a vessel saturated with solvent vapour.[85] The donor and/or acceptor domains then rearrange due to a combination of the solvent molecules trapped in the film and those present in the atmosphere.

Ideally the BHJ should be ordered to ensure a) that every exciton generated can reach the donor-acceptor interface, b) that every free charge should be transported to the contacts and c) that no charge reaches the wrong contact. An interdigitated

morphology can address all these issues where the digits or pillars have the optimum width to maximize photogeneration, and the maximum length to ensure all charge carriers can be transported along their lengths to reach the electrodes. Between the intrinsic layer and each electrode there is a pristine layer of the donor or acceptor molecule, preventing unwanted surface recombination. Several approaches have been demonstrated through the use of templates, stamps or *via* self-assembly.[86-88] The use of templates is problematic, as the templates must be etched after use, which can dope or degrade the active layer exposed. The most elegant demonstration of controlling the morphology through self-assembly has been presented by Matsuo and coworkers, where they utilized a porphyrin derivative that is soluble at first, but following thermal annealing of the deposited film, the molecule undergoes a reverse Diels-Alder reaction, rendering it insoluble.[89] Next a blend of the same porphyrin and a fullerene derivative with excellent packing properties is deposited, and then annealed. The freshly deposited porphyrin derivatives then undergo the same reverse Diels-Alder reaction and become insoluble, with the added advantage of forming self-assembled columns on top of the primary porphyrin layer. The fullerene, having the excellent packing properties, stacks between the porphyrin columns thus forming a well-ordered inderdigitated BHJ.

This brief overview of the basic device operating mechanisms of OSCs and the characteristics of different device architectures, has illustrated that there are many factors to consider when trying to design and optimize a device. The molecules themselves need to have a combination of properties, including high absorption, good mobility, good film forming properties films, and be to stable under working conditions. Furthermore, the donor and acceptor molecules must be compatible both optically and electronically. If they are used in solution processed bulk heterojunction they must be compatible in the same solvent, and be able to form

well-ordered morphologies. Furthermore, we must take into account other aspects of the device such as the contacts and transport/blocking layers employed that may have adverse affects on the performance. Studying these issues in more detail through a combination of material and optoelectronic techniques will provide more insights into the limiting factors of OSCs. These findings can then help OSCs to improve even further and reach their full potential as next-generation renewable and sustainable light harvesting devices.

3. Organic Light Emitting Diodes

Organic materials have been known to conduct electricity since the 1950s. In 1963 Pope applied these phenomenon to produce electroluminescence from a single crystal of anthracene.[50] This was the start of the field of organic lighting, however to produce light, a large DC current was required to drive the electroluminescence. The driving voltage was in excess of 100 V, which is neither energetically favourable nor safe. Also, at this high voltage there is a significant amount of background noise generated from the device. It was not until the late 1980's that organic lighting made a practical breakthrough. Tang, in 1987 reported on an organic light emitting diode, which generated electroluminescence greater than 1000 Cd/A at a driving voltage of less than 10 V.[90] The pioneering work of Tang still serves as the prototype structure for OLEDs. This OLED architecture consisted of a hole transport layer of aromatic diamine and an emissive layer of 8-hydroxyquinolinealuminium (Alq3) sandwiched between a metal cathode and transparent conducting anode (TCO), Mg-Ag and ITO respectively. Figure 6 illustrates a basic OLED and its method of operation.

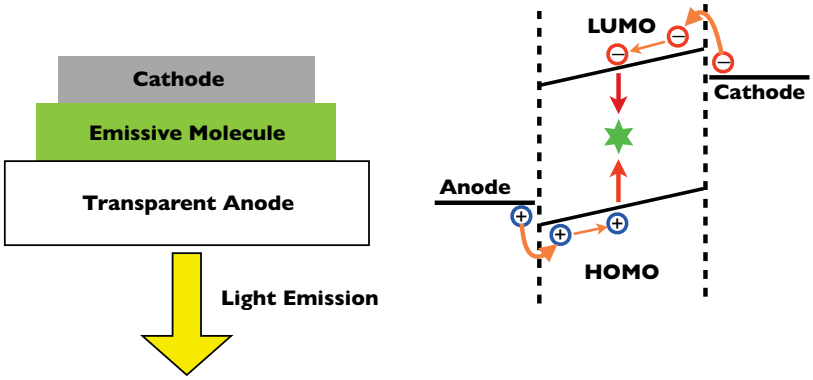

Figure 6 Basic OLED device architecture and working mechanism. Charges are injected into the emissive organic layer, *i.e.* electrons from the cathode into the LUMO and holes from the anode into the HOMO. The excess charge carriers generated recombine with each other (geminate recombination), releasing the energy in the form of light.

Twenty-three years have passed since Tang's report and significant progress has been made in the field of OLEDs. In fact there are now electronic devices on the market that contain OLED displays however OLEDs have yet to enter the lighting market. The main reasons for this are the cost of fabrication and device lifetimes. Most OLEDs rely on several vacuum deposition steps, which are costly in terms of time and expenses. One promising route towards low-cost solution processable OLEDs is the use of conjugated polymers. Burroughs et al. first discovered electroluminescence in conjugated polymers in 1990.[91] Semiconducting polymers are of great interest, especially to the material scientist and product designer, as they offer the material properties of a plastic and the electronic properties of a metal. While, polymer OLEDs have the advantage of containing a solution processable emissive layer they still share a problem with small molecule OLEDs. The problem being on the choice of electrodes utilised. Generally low work-function cathodes are required. Unfortunately these low work-function electrodes are moisture sensitive and susceptible to degradation in the presence of oxygen. Even relatively stable Mg-Ag cathodes have been found to degrade gradually in air due to oxygen.[92,93] In order to protect the OLED from contamination it is therefore

necessary to incorporate an encapsulation layer to protect the device from air and moisture. This layer can cost up to 40% of the total price of production for an OLED. Recently hybrid organic-inorganic light emitting devices (HyLEDs) employing air stable transition metal oxides (TMO) have been developed.[94-96] These hybrid OLEDs can eliminate or at least minimise the requirements for encapsulation. HyLEDs use an inverted architecture, which allows the use of a high work function, air-stable top electrode and transition metal oxide transport layers. The TMO layers are the key feature of the devices as they protect the emissive organic layer from oxygen and water. These hybrid devices are thus very attractive to industry as they can eliminate the costly encapsulation layer and allow low-cost roll-to-roll (R2R) processing. Note that the same arguments made here for hybrid OLEDs can also be made for OSCs.

The general architecture of a HyLED consists of an emissive conjugated polymer layer sandwiched between an electron transport layer (TiO_2, ZnO, ZrO_2),[96-98] and a hole transport layer (MoO_3),[99] with ITO serving as the bottom electrode and Au as the top electrode. The conjugated light-emitting polymer (LEP) typically employed in HyLEDs to date has been the green emitting F8BT.

Bolink and Snaith have discussed the operating mechanism of HyLEDs previously.[100,101] They found the devices are hole dominated by a large hole current for two reasons. Firstly, there is Ohmic contact between MoO_3 and F8BT which allows facile hole-injection from Au into the LUMO of F8BT. Secondly, a large barrier to injection exists between the LUMO of F8BT and the conduction band of ITO. Due to this large barrier it is difficult to inject electrons into F8BT. Holes are injected first and travel towards the ETL where a build-up of charge develops creating a localised electric field. When the potential difference becomes great enough electrons are able to overcome the energy barrier. Once injected into the

polymer the electrons are in an excited state and spontaneously relax to the ground state with the excess energy radiated as light. The wavelength of emission depends solely on the energy difference between the LEPs HOMO-LUMO levels. Several approaches have been taken to improve the injection of electrons into the LUMO of the LEP by using a larger band-gap ETL,[97] inserting a thin Cs_2Co_3 hole-blocking layer,[102,103] and depositing a self-assembled dipole monolayer.[104] Current efficiencies of 2.7 Cd/A, 8 Cd/A and 2.8 Cd/A have been obtained for each respective approach.

In summary, HyLEDs are promising alternatives to standard OLEDs and offer a way to reduce fabrication costs significantly by reducing the need for a costly encapsulation process. The metal oxide layers can also be used to change the electronic properties of the organic emissive layer. Tuning the electronic properties of the metal oxide layer therefore provides a route for improved performance.

4. Aims and Overview of the Thesis

The thesis sets out to understand key loss mechanisms in planar heterojunction solar cells to provide design rules for future high efficiency solar cells. Small molecules are employed in each case as less is known about their device operating physics as opposed to polymer based devices. Furthermore, it includes a study on hybrid organic-inorganic light emitting diodes, the results of which are also applicable to organic solar cells.

In each study we ask questions that are relevant and of great importance to advancing the field.

Chapter 2 details the experimental procedures employed in the main body of the thesis.

In *Chapter 3* we study the origin of the open circuit voltage in squaraine/C60 bilayer device. Furthermore, the influence of a MoO_3 hole transport layer on device performance is probed. Transient optoelectronic techniques are employed to study devices under working conditions to understand the distribution of charge carriers in the active layer together with the charge carrier recombination kinetics. These studies, together with device simulations, provide an explanation for the trends in open-circuit voltages observed.

Chapter 4 is focused on a series of water-soluble zinc phthalocyanine (wsZnPc) donor molecules. The use of chlorinated solvents in processing OSC active layers but has inherent health issues and environmental dangers. Removing the use of these solvents is vital for a truly environmentally friendly technology. An issue with water-soluble phthalocyanines is their failure to generate any photocurrent. We find that by tuning the number of sulfonate substituents on the molecule, we can "unlock" the photocurrent, attributing the interface energetics between the wsZnPc and C_{60} acceptor to be the limiting factor in these devices.

Chapter 5 is based on understanding the origin of the open-circuit voltage in hybrid organic-inorganic devices based on PbS colloidal quantum dot (CQD) donors and a fullerene acceptor. The devices fabricated were, like in previous chapters bilayers, with C_{60} acting as the acceptor. Charge carrier densities and charge carrier lifetimes were obtained through the use of transient optoelectronic measurements of devices under working conditions. Comparing the dependence of charge carrier lifetime on charge carrier density could then be used to reconstruct the experimental current/voltage curve perfectly, using a method originally applied to organic bulk heterojunction solar cells. This result shows that non-geminate recombination is the key factor that is limiting the open-circuit in these devices.

Chapter 6 deals with hybrid organic-inorganic light emitting diodes that utilize transition metal oxide transport layers and a high work function gold top electrode. The advantage of this is that these materials are air-stable and will act to protect the active layer from degradation. This architecture thus removes the need of a costly encapsulation process, thus driving the fabrication costs down. We concentrated here on understanding the role of processing temperature of the ZnO electron transport layer on device performance, as the previous values in the literature were too high to be industrially viable. We find that the temperature can be reduced significantly while still maintaining respectable device performance.

5. References

1. N. Armaroli and V. Balzani, *Angewandte Chemie International Edition*, 2007, **46**, 52-66.
2. A. Demirbas, *Energy Sources Part B-Economics Planning and Policy*, 2008, **3**, 41-49.
3. N. S. Lewis and D. G. Nocera, *Proceedings of the National Academy of Sciences*, 2006, **103**, 15729-15735.
4. R. E. H. Sims, H. H. Rogner and K. Gregory, *Energy Policy*, 2003, **31**, 1315-1326.
5. I. Dincer, *Energy Policy*, 1999, **27**, 845-854.
6. F. Manzano-Agugliaro, A. Alcayde, F. G. Montoya, A. Zapata-Sierra and C. Gil, *Renewable and Sustainable Energy Reviews*, 2013, **18**, 134-143.
7. N. L. Panwar, S. C. Kaushik and S. Kothari, *Renewable and Sustainable Energy Reviews*, 2011, **15**, 1513-1524.
8. I. B. Fridleifsson, *Renewable & Sustainable Energy Reviews*, 2001, **5**, 299-312.
9. P. Michalak and J. Zimny, *Renewable & Sustainable Energy Reviews*, 2011, **15**, 2330-2341.
10. A. J. Ragauskas, C. K. Williams, B. H. Davison, G. Britovsek, J. Cairney, C. A. Eckert, W. J. Frederick, J. P. Hallett, D. J. Leak, C. L. Liotta, J. R. Mielenz, R. Murphy, R. Templer and T. Tschaplinski, *Science*, 2006, **311**, 484-489.
11. K. S. Gallagher, *Daedalus*, 2013, **142**, 59-77.

12. S. Ruiz Romero, A. Colmenar Santos and M. A. Castro Gil, *Renewable Energy*, 2012, **43**, 322-330.
13. A. Tolon-Becerra, X. Lastra-Bravo and F. Bienvenido-Barcena, *Renewable Energy*, 2011, **36**, 2067-2077.
14. J. K. Kaldellis, M. Kapsali, E. Kaldelli and E. Katsanou, *Renewable Energy*, 2013, **52**, 197-208.
15. M. Z. Jacobson, *Energy & Environmental Science*, 2009, **2**, 148-173.
16. T. R. Cook, D. K. Dogutan, S. Y. Reece, Y. Surendranath, T. S. Teets and D. G. Nocera, *Chemical Reviews*, 2010, **110**, 6474-6502.
17. J. Y. Tsao, M. E. Coltrin, M. H. Crawford and J. A. Simmons, *Proceedings of the Ieee*, 2010, **98**, 1162-1179.
18. http://ec.europa.eu/energy/efficiency/ecodesign/doc/committee/2008_12_08_technical_briefing_household_lamps.pdf, 2008.
19. R. Clear and S. Berman, *Journal of the Illuminating Engineering Society*, 1994, **23**, 138-152.
20. T. Gessmann and E. F. Schubert, *Journal of Applied Physics*, 2004, **95**, 2203-2216.
21. J. L. Pautrat, E. Hadji, J. Bleuse and N. Magnea, *Journal of Electronic Materials*, 1996, **25**, 1388-1393.
22. A. W. Hains, Z. Liang, M. A. Woodhouse and B. A. Gregg, *Chemical Reviews*, 2010, **110**, 6689-6735.
23. N. T. Kalyani and S. J. Dhoble, *Renewable & Sustainable Energy Reviews*, 2012, **16**, 2696-2723.
24. C. Zhong, C. Duan, F. Huang, H. Wu and Y. Cao, *Chemistry of Materials*, 2011, **23**, 326-340.
25. B. Walker, C. Kim and T.-Q. Nguyen, *Chemistry of Materials*, 2011, **23**, 470-482.
26. J. You, L. Dou, K. Yoshimura, T. Kato, K. Ohya, T. Moriarty, K. Emery, C.-C. Chen, J. Gao, G. Li and Y. Yang, *Nat Commun*, 2013, **4**, 1446.
27. S. A. Kalogirou, *Progress in Energy and Combustion Science*, 2004, **30**, 231-295.
28. B. O'Regan and M. Gratzel, *Nature*, 1991, **353**, 737-740.

29. M. G. Walter, E. L. Warren, J. R. McKone, S. W. Boettcher, Q. Mi, E. A. Santori and N. S. Lewis, *Chemical Reviews*, 2010, **110**, 6446-6473.
30. I. McConnell, G. Li and G. W. Brudvig, *Chemistry & Biology*, 2010, **17**, 434-447.
31. A. E. Becquerel, *Comptes rendus*, 1839, **9**, 561–567.
32. A. W. Copeland, O. D. Black and A. B. Garrett, *Chemical Reviews*, 1942, **31**, 177-226.
33. D. M. Chapin, C. S. Fuller and G. L. Pearson, *Journal of Applied Physics*, 1954, **25**, 676-677.
34. A. Goetzberger, C. Hebling and H. W. Schock, *Materials Science & Engineering R-Reports*, 2003, **40**, 1-46.
35. A. F. B. Braga, S. P. Moreira, P. R. Zampieri, J. M. G. Bacchin and P. R. Mei, *Solar Energy Materials and Solar Cells*, 2008, **92**, 418-424.
36. M. Konagai, *Japanese Journal of Applied Physics*, 2011, **50**, 030001 - 030013.
37. T. Saga, *Npg Asia Materials*, 2010, **2**, 96-102.
38. X. Z. Wu, *Solar Energy*, 2004, **77**, 803-814.
39. B. J. Stanbery, *Critical Reviews in Solid State and Materials Sciences*, 2002, **27**, 73-117.
40. R. W. Miles, K. M. Hynes and I. Forbes, *Progress in Crystal Growth and Characterization of Materials*, 2005, **51**, 1-42.
41. M. Marwede, W. Berger, M. Schlummer, A. Maeurer and A. Reller, *Renewable Energy*, 2013, **55**, 220-229.
42. C. W. Tang, *Applied Physics Letters*, 1986, **48**, 183-185.
43. B. P. Rand, J. Genoe, P. Heremans and J. Poortmans, *Progress in Photovoltaics*, 2007, **15**, 659-676.
44. M. T. Lloyd, J. E. Anthony and G. G. Malliaras, *Materials Today*, 2007, **10**, 34-41.
45. Y. Sun, G. C. Welch, W. L. Leong, C. J. Takacs, G. C. Bazan and A. J. Heeger, *Nature Materials*, 2012, **11**, 44-48.
46. Y.-H. Chen, L.-Y. Lin, C.-W. Lu, F. Lin, Z.-Y. Huang, H.-W. Lin, P.-H. Wang, Y.-H. Liu, K.-T. Wong, J. Wen, D. J. Miller and S. B. Darling, *Journal of the American Chemical Society*, 2012, **134**, 13616-13623.
47. W. Li, A. Furlan, K. H. Hendriks, M. M. Wienk and R. A. J. Janssen, *Journal of the American Chemical Society*, 2013, **135**, 5529-5532.

48. Y. Lin, Y. Li and X. Zhan, *Chemical Society Reviews*, 2012, **41**, 4245-4272.
49. A. Mishra and P. Bäuerle, *Angewandte Chemie International Edition*, 2012, **51**, 2020-2067.
50. M. Pope and C. E. Sweneberg, *Electronic Processes in Organic Crystals and Polymers*, 2nd edn., Oxford University Press, New York, 1999.
51. B. A. Gregg and M. C. Hanna, *Journal of Applied Physics*, 2003, **93**, 3605-3614.
52. G. A. Chamberlain, *Solar Cells*, 1983, **8**, 47-83.
53. J. Wagner, M. Gruber, A. Wilke, Y. Tanaka, K. Topczak, A. Steindamm, U. Hormann, A. Opitz, Y. Nakayama, H. Ishii, J. Pflaum, N. Koch and W. Brutting, *Journal of Applied Physics*, 2012, **111**, 054509-054512.
54. W. Tress, A. Petrich, M. Hummert, M. Hein, K. Leo and M. Riede, *Applied Physics Letters*, 2011, **98**, 063301.
55. J. A. Barker, C. M. Ramsdale and N. C. Greenham, *Physical Review B*, 2003, **67**, 075205.
56. A. Petersen, A. Ojala, T. Kirchartz, T. A. Wagner, F. Würthner and U. Rau, *Physical Review B*, 2012, **85**, 245208.
57. C. Schwarz, S. Tscheuschner, J. Frisch, S. Winkler, N. Koch, H. Bässler and A. Köhler, *Physical Review B*, 2013, **87**, 155205.
58. V. Chauhan, R. Hatton, P. Sullivan, T. Jones, S. W. Cho, L. Piper, A. deMasi and K. Smith, *Journal of Materials Chemistry*, 2010, **20**, 1173-1178.
59. N. Li, B. E. Lassiter, R. R. Lunt, G. Wei and S. R. Forrest, *Applied Physics Letters*, 2009, **94**, 023307.
60. A. Maurano, R. Hamilton, C. G. Shuttle, A. M. Ballantyne, J. Nelson, B. O'Regan, W. Zhang, I. McCulloch, H. Azimi, M. Morana, C. J. Brabec and J. R. Durrant, *Advanced Materials*, 2010, **22**, 4987-4992.
61. M. D. Perez, C. Borek, S. R. Forrest and M. E. Thompson, *Journal of the American Chemical Society*, 2009, **131**, 9281-9286.
62. C. G. Shuttle, R. Hamilton, B. C. O'Regan, J. Nelson and J. R. Durrant, *Proceedings of the National Academy of Sciences*, 2010, **107**, 16448-16452.
63. D. Credgington and J. R. Durrant, *The Journal of Physical Chemistry Letters*, 2012, **3**, 1465-1478.

64. B. Conings, L. Baeten, H.-G. Boyen, D. Spoltore, J. D'Haen, M. K. V. Bael and J. V. Manca, *Applied Physics Letters*, 2012, **100**, 203905.
65. D. Venkataraman, S. Yurt, B. H. Venkatraman and N. Gavvalapalli, *Journal of Physical Chemistry Letters*, 2010, **1**, 947-958.
66. J. Nelson, *Materials Today*, 2011, **14**, 462-470.
67. J. Roncali, *Accounts of Chemical Research*, 2009, **42**, 1719-1730.
68. D. Wynands, M. Levichkova, K. Leo, C. Uhrich, G. Schwartz, D. Hildebrandt, M. Pfeiffer and M. Riede, *Applied Physics Letters*, 2010, **97**, 073503.
69. A. Foertig, A. Wagenpfahl, T. Gerbich, D. Cheyns, V. Dyakonov and C. Deibel, *Advanced Energy Materials*, 2012, **2**, 1483-1489.
70. A. Sánchez-Díaz, L. Burtone, M. Riede and E. Palomares, *The Journal of Physical Chemistry C*, 2012, **116**, 16384-16390.
71. G. Chen, H. Sasabe, Z. Wang, X.-F. Wang, Z. Hong, Y. Yang and J. Kido, *Advanced Materials*, 2012, **24**, 2768-2773.
72. J. Yang and T. Q. Nguyen, *Organic Electronics*, 2007, **8**, 566-574.
73. E. L. Ratcliff, B. Zacher and N. R. Armstrong, *Journal of Physical Chemistry Letters*, 2011, **2**, 1337-1350.
74. Y. Kinoshita, R. Takenaka and H. Murata, *Applied Physics Letters*, 2008, **92**, 243309.
75. I. Hancox, L. A. Rochford, D. Clare, P. Sullivan and T. S. Jones, *Applied Physics Letters*, 2011, **99**, 013304.
76. J. R. Manders, S.-W. Tsang, M. J. Hartel, T.-H. Lai, S. Chen, C. M. Amb, J. R. Reynolds and F. So, *Advanced Functional Materials*, 2013, doi: 10.1002/adfm.201202269.
77. S. Y. Wang, E. I. Mayo, M. D. Perez, L. Griffe, G. D. Wei, P. I. Djurovich, S. R. Forrest and M. E. Thompson, *Applied Physics Letters*, 2009, **94**, 23304.
78. T. Sakurai, S. Toyoshima, H. Kitazume, S. Masuda, H. Kato and K. Akimoto, *Journal of Applied Physics*, 2010, **107**, 043707.
79. R. Hamilton, C. G. Shuttle, B. O'Regan, T. C. Hammant, J. Nelson and J. R. Durrant, *The Journal of Physical Chemistry Letters*, 2010, **1**, 1432-1436.
80. J. Sakai, T. Taima, T. Yamanari and K. Saito, *Solar Energy Materials and Solar Cells*, 2009, **93**, 1149-1153.

81. B. Walker, A. B. Tomayo, X. D. Dang, P. Zalar, J. H. Seo, A. Garcia, M. Tantiwiwat and T. Q. Nguyen, *Advanced Functional Materials*, 2009, **19**, 3063-3069.
82. V. Palermo, M. B. J. Otten, A. Liscio, E. Schwartz, P. A. J. de Witte, M. A. Castriciano, M. M. Wienk, F. Nolde, G. De Luca, J. Cornelissen, R. A. J. Janssen, K. Mullen, A. E. Rowan, R. J. M. Nolte and P. Samori, *Journal of the American Chemical Society*, 2008, **130**, 14605-14614.
83. W. Chen, M. P. Nikiforov and S. B. Darling, *Energy & Environmental Science*, 2012, **5**, 8045-8074.
84. G. Wei, S. Wang, K. Sun, M. E. Thompson and S. R. Forrest, *Advanced Energy Materials*, 2011, **1**, 184-187.
85. A. Viterisi, F. Gispert-Guirado, J. W. Ryan and E. Palomares, *Journal of Materials Chemistry*, 2012, **22**, 15175-15182.
86. D. Chen, W. Zhao and T. P. Russell, *Acs Nano*, 2012, **6**, 1479-1485.
87. W. W. H. Wong, T. B. Singh, D. Vak, W. Pisula, C. Yan, X. L. Feng, E. L. Williams, K. L. Chan, Q. H. Mao, D. J. Jones, C. Q. Ma, K. Mullen, P. Bauerle and A. B. Holmes, *Advanced Functional Materials*, 2010, **20**, 927-938.
88. A. Tada, Y. Geng, Q. Wei, K. Hashimoto and K. Tajima, *Nature Materials*, 2011, **10**, 450-455.
89. Y. Matsuo, Y. Sato, T. Niinomi, I. Soga, H. Tanaka and E. Nakamura, *Journal of the American Chemical Society*, 2009, **131**, 16048-16050.
90. C. W. Tang and S. A. Vanslyke, *Applied Physics Letters*, 1987, **51**, 913-915.
91. J. H. Burroughes, D. D. C. Bradley, A. R. Brown, R. N. Marks, K. Mackay, R. H. Friend, P. L. Burns and A. B. Holmes, *Nature*, 1990, **347**, 539-541.
92. H. Aziz, Z. Popovic, C. P. Tripp, N. X. Hu, A. M. Hor and G. Xu, *Applied Physics Letters*, 1998, **72**, 2642-2644.
93. J. McElvain, H. Antoniadis, M. R. Hueschen, J. N. Miller, D. M. Roitman, J. R. Sheats and R. L. Moon, *Journal of Applied Physics*, 1996, **80**, 6002-6007.
94. H. J. Bolink, H. Brine, E. Coronado and M. Sessolo, *Advanced Materials*, **22**, 2198-+.
95. S. A. Haque, S. Koops, N. Tokmoldin, J. R. Durrant, J. S. Huang, D. D. C. Bradley and E. Palomares, *Advanced Materials*, 2007, **19**, 683-+.

96. K. Morii, M. Ishida, T. Takashima, T. Shimoda, Q. Wang, M. K. Nazeeruddin and M. Gratzel, *Applied Physics Letters*, 2006, **89**.

97. N. Tokmoldin, *Advanced Materials*, 2009, **21**, 1–4.

98. H. J. Bolink, E. Coronado, D. Repetto and M. Sessolo, *Applied Physics Letters*, 2007, **91**, 223501/223501-223501/223503.

99. Y. Nakayama, K. Morii, Y. Suzuki, H. Machida, S. Kera, N. Ueno, H. Kitagawa, Y. Noguchi and H. Ishii, *Advanced Functional Materials*, 2009, **19**, 3746-3752.

100. H. J. Bolink, E. Coronado, D. Repetto, M. Sessolo, E. M. Barea, J. Bisquert, G. Garcia-Belmonte, J. Prochazka and L. Kavan, *Advanced Functional Materials*, 2008, **18**, 145-150.

101. D. Kabra, M. H. Song, B. Wenger, R. H. Friend and H. J. Snaith, *Advanced Materials (Weinheim, Germany)*, 2008, **20**, 3447-3452.

102. H. J. Bolink, E. Coronado and M. Sessolo, *Chemistry of Materials*, 2009, **21**, 439-441.

103. K. Morii, M. Omoto, M. Ishida and M. Graetzel, *Japanese Journal of Applied Physics*, 2008, **47**, 7366-7368.

104. J. S. Park, B. R. Lee, J. M. Lee, J. S. Kim, S. O. Kim and M. H. Song, *Applied Physics Letters*, **96**.

Chapter 2
Experimental Procedures

General measurements and information regarding experimental procedures that are used in more than one chapter are presented here. Device preparation is adequately explained in each results-based chapter, and varies from chapter to chapter so it has been excluded from this chapter. All relevant information regarding HyLED device fabrication and characterization are present in Chapter 6, so they too have been excluded from this chapter.

1. Materials Characterisation

1.1 Absorption

UV-Vis measurements were carried out on a Shimadzu UV-1700PC spectrophotometer equipped with a photomultiplier detector, double beam optics, and D_2 and W light source. Or in the case of UV-Vis-NIR measurements, they were carried out on a Lamba 1050 PerkinElmer spectrophotometer equipped with a PMT, InGaAs and PbS detectors system, double beam optics, double monochromator and D_2 and W light sources.

1.2 Photoluminescence

Films and solutions were probed using an Aminco-Bowman Series 2 Luminescence spectrofluorimeter equipped with a high voltage PMT detector and continuum Xe light source.

1.3 Atomic Force Microscopy

Atomic Force Microscopy (AFM) of the samples was performed in intermittent contact mode using a Molecular Imaging (now Agilent) PicoPlus SPM II. Samples were measured in ambient conditions using Nanosensors NCHR-Point Probe Plus probes with a typical force constant of 42 N m^{-1}, a resonant frequency of 330 kHz and mean tip radius of 7 nm.

2. Solar Cell Device Characterisation

2.1 Current-Voltage Characteristics

Devices were measured in the dark and under AM 1.5G conditions using an Abet Solar 2000 solar simulator applying bias and recording the current using a Keithley 2400 digital source meter. A Labview interface was used to control the source meter and record the *I-V* curves. 1 Sun conditions were obtained using a calibrated silicon diode (NREL) and lower light conditions were simulated using neutral density filters. All devices were measured in a sealed holder under a N_2 atmosphere.

2.2 Incident Photon to Current Efficiency

A homebuilt system was used to record the incident photon to current efficiency (IPCE) consisting of a 150 W Oriel xenon lamp, connected to a Spectral Products Cm110 monochromator to scan the Uv-Vis spectrum. A Keithley 2400 digital source meter was used to record the current at each specific wavelength, and a Gentec Solo2 power monitor probed the power of the incident light.

2.3 Charge Extraction

Charge extraction (CE) was employed to probe the charge density within the active layer of the device under working conditions using a homebuilt system. Devices were held at open circuit by applying bias from either a focused array of LEDs or

an external power source (Keithley 2400 digital source meter). In the case of applying bias from a power source, the devices were still subject to illumination. Once the device reached steady state it was then short-circuited with the LEDs switched off simultaneously (switch-off time / relay = 300 ns), leaving the charge stored in the active layer to decay through a small 50 Ω resistor. A Yokogawa 2052 digital oscilloscope was used to record the voltage decay across the resistor. Using Ohm's law the voltage transient could be turned into a current transient, which was subsequently integrated to calculate the total charge in the active layer at each applied bias (light or electrical). In general the device is measured from open circuit voltage values corresponding to >1 Sun conditions to 0 V or extending into the negative when required. In some instances the lifetime of the voltage transient is on the same order as the non-geminate recombination rate. Therefore we use an iterative procedure using a procedure written in Matlab to calculate the incurred charge losses during extraction. The procedure is adapted from an original source gratefully given to us by the group of Prof. James Durrant at Imperial College London. All CE data shown in the subsequent experimental chapters have been corrected for using this procedure. The device layout is illustrated in Figure 1.

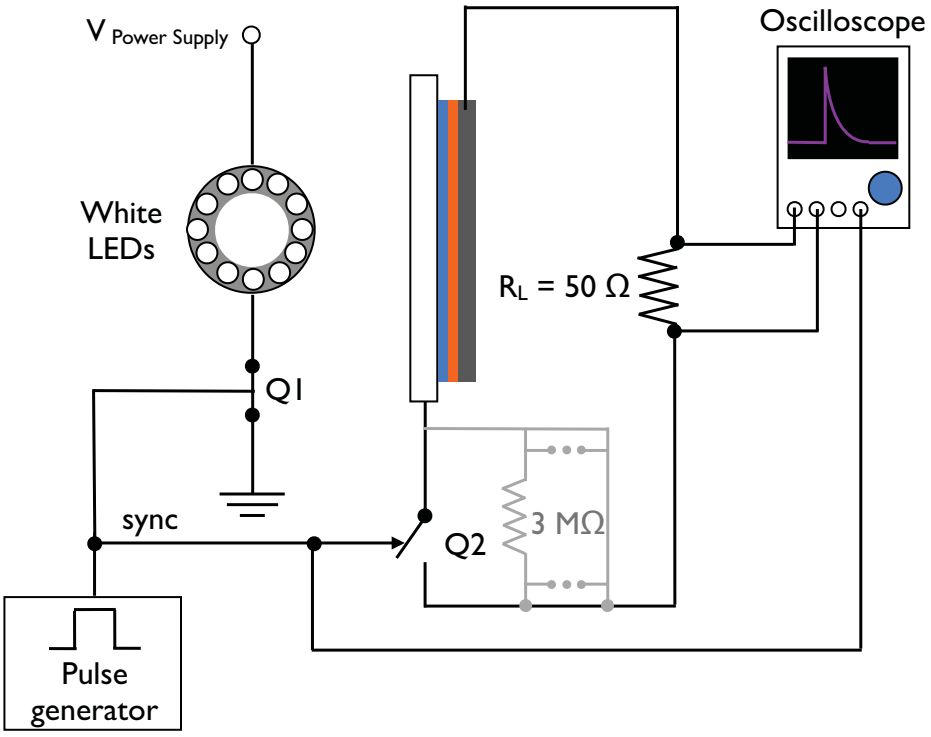

Figure 1 Schematic diagram of the CE setup

3.4 Transient Photovoltage

Transient photovoltage (TPV) measurements were carried out on working devices through applying a light bias (the same ring of LEDs used in CE) and holding the device at steady state through a high resistance. Once the device reached steady state conditions, a low-intensity laser pulse (PTI GL-3300 Nitrogen Laser) irradiated the sample to allow a small excess number of charge carriers to be generated. As the device is being held at open-circuit, the excess charge generated has no choice but to recombine. The transient decay of the charge carriers is recorded using a Yokogawa 2052 digital oscilloscope. Sweeping from high-applied bias (high illumination) to low-applied bias (low illumination) allows a correlation between charge carrier lifetime and voltage to be made. The irradiation wavelength

was chosen to be close to but not at the maximum of the donor absorption spectrum. A graded neutral density filter was used to control the intensity of the small perturbation, usually keeping the value between 5 and 10 mV.

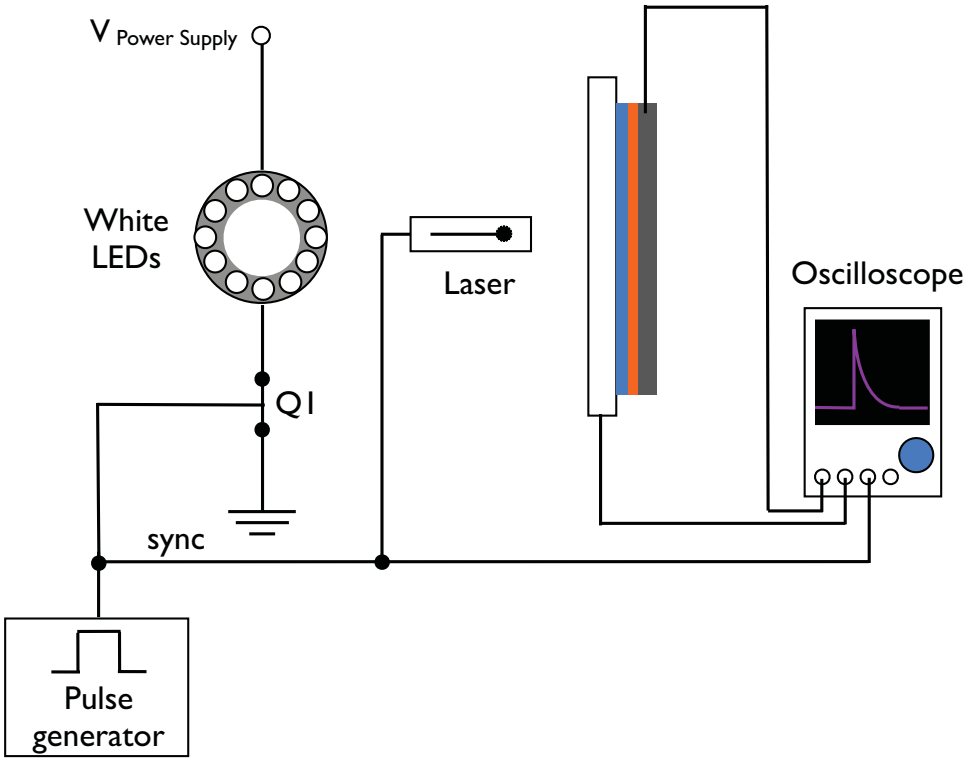

Figure 1 Schematic diagram of the TPV setup

Chapter 3
The Effect of Donor Layer Thickness and a MoO_3 Hole Transport Layer on Device Performance in Squaraine/ C_{60} Bilayer Solar Cells

1. Introduction

Organic solar cells (OSCs) are edging closer to realizing their potential as low-cost energy harvesters certified efficiencies of 9.2% for a single junction,[1] and now as high as 10.6% for tandem devices.[2] In recent years small molecule based OSCs (SMOSCs) have made particular progress and are steadily catching up on their polymer counterparts, with record efficiencies now approaching 8%.[3] Now that small molecular weight organic semiconductors have demonstrated their ability to produce efficient devices, further progress is expected especially as they offer several favourable characteristics compared to their polymers, such as more facile synthesis and purification methods, high tunability and the ability to be fabricated *via* solution processing and/or highly reproducible vacuum-based methods. Although much progress has been made in both polymer and small molecule based OSCs, at some point a bottleneck will be met making it harder and harder for further improvements in device performance to be obtained. Improving our understanding of fundamental operating mechanisms controlling device

performance is key to meet these challenges. The open-circuit voltage (V_{OC}) is one of the principle figures of merit that defines solar cell efficiency and its origin is understood to a certain degree, but its controlling factors can change on a case-by-case basis. The V_{OC} is the voltage at which no net-current flows in the device and is controlled by the balance between charge generation and charge recombination in the device. The recombination rate scales with the equilibrium charge carrier concentrations and therefore exponentially with the energy levels, with changes in energetics having a large influence on V_{OC}. Understanding the factors controlling the recombination and thus V_{OC} are therefore very important but are non-trivial, as the recombination kinetics may change from one material to the next,[4] or as a function of the microstructure of one material.[5] While recombination is often considered to happen at the internal donor:acceptor interface, charges may also recombine at the cathode or anode, especially when contacts are not optimized. In these cases, the V_{OC} might depend quite strongly on the work function of the anode or cathode.[6]

To date most of the studies on OSCs that take into account the energetics of the active layer together with the charge recombination kinetics are based on bulk-heterojunction (BHJ) devices. However, planar heterojunction (PHJ) devices have not received the same attention, with many reports describing the origin of V_{OC} in these devices using steady state measurements or else theoretical calculations. It has been shown first by ourselves and subsequently by others,[7,8] that there is a significant difference between PHJ and BHJ devices in terms of the distribution of charges within the device as well the interfacial non-geminate recombination dynamics. From previous studies of BHJ devices, the relationship between charge carrier density and recombination dynamics changes from material to material,[4] not to mention the selective contacts employed.[9]

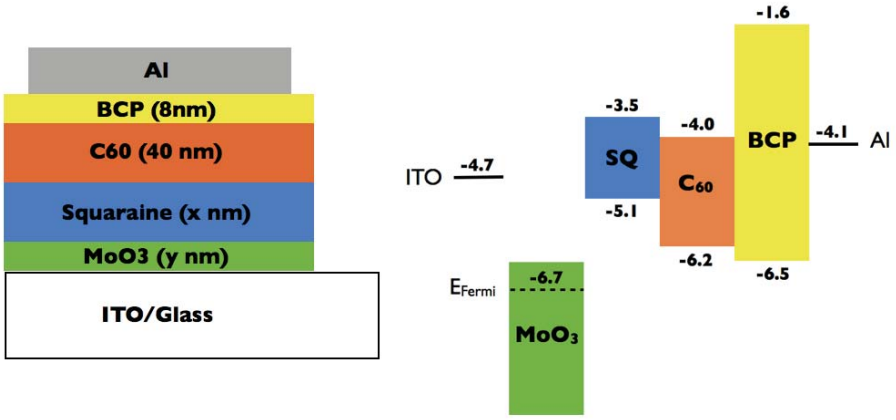

Figure 1 Device architecture and energy levels for the materials employed where the thickness of MoO_3 and SQ varied, with the thickness of MoO_3, y, equal to 0 or 8 nm and the thickness of SQ, x, equal to 6, 9 or 12 nm.

Squaraines are excellent NIR-absorbing dyes possessing high extinction coefficients, and high stability.[10-12] Several squaraine derivatives have been employed in organic solar cells recently,[13-19] with efficiencies of ~6% having been reported.[20,21] However, although squaraines posses excellent absorption properties, they are limited by inherently low exciton diffusion lengths, thus restricting their light-harvesting ability, especially in a PHJ device.[19,22] Here we study a bilayer structure based on 2,4-bis[4-(*N,N*-diisobutylamino)-2,6-dihydroxyphenyl] squaraine (SQ) donor and C_{60} acceptor, where we change the thickness of the SQ layer and notice a strong shift in V_{OC} with increasing thickness. Furthermore, for each thickness of SQ employed, the effect of employing a MoO_3 (HTL) transport layer was investigated (see Figure 1 for a schematic of the device architecture and relevant energy levels). We find that there is a strong influence on performance depending on the thickness of the SQ layer employed, with V_{OC} increasing with SQ thickness however there is a concomitant decrease in fill factor (FF). Furthermore the MoO_3 layer increases the V_{OC} of the device for SQ layers less than 9 nm but there it has no significant effect on the V_{OC} for higher SQ thicknesses. Transient

optoelectronic techniques were used to probe the effects of both SQ thickness and the MoO_3 interfacial layer on the charge density in the active layer under working conditions as well as quantifying the rate of non-geminate charge carrier recombination.

2. Experimental

2,4-bis[4-(*N,N*-diisobutylamino)-2,6-dihydroxyphenyl] squaraine was synthesized following the procedure of Tian *et al.*[12] Devices were fabricated with the architecture ITO/MoO_3(0 or 8 nm)/SQ(6, 9 or 12 nm)/C_{60}(40 nm)/BCP(8 nm)/Al(100 nm). ITO substrates (Psiotec, 5 Ohm/square) were sonicated in acetone and twice in isopropanol followed by 20 min of UV/O_3 treatment. All layers were deposited by vacuum sublimation at a pressure not exceeding 2 x 10^{-6} mbar. Devices were placed in an air-tight holder, sealed in a N_2 filled glovebox, and measured using an Abet Sun 2000 solar simulator (100 mW/cm^2, AM 1.5 G), calibrated with a silicon photodiode (NREL), attached to a Keithley 2400 digital source meter. Transient photovoltage (TPV) measurements were carried out using an array of LEDs and a nanosecond nitrogen laser, exciting the devices at 660 nm. Charge extraction experiments were done using a homebuilt system, where the steady state light source was generated by an array of LEDs and the transient decay of the charge stored in the device when switched from open to short-circuit was recorded using a Yokogawa oscilloscope.

3. Results

The current-voltage (*J-V*) characteristics of devices without a MoO_3 interfacial layer are shown first in Figure 2, which demonstrate a clear dependence of V_{OC} on the SQ thickness. An opposite trend is observed for the FF. Regarding the photocurrent, except for a small decrease in the short-circuit current density (J_{SC}) between devices employing MoO_3, there is no change in J_{SC} with increasing SQ thickness, as the thickness of the layers exceed the exciton diffusion length. The power conversion efficiency (η) does not differ too much due to the concomitant decrease of FF with increase in V_{OC}. Clearly, increasing the SQ thickness therefore has more influence on optimizing the donor/acceptor interface rather than increasing photocurrent. Employing a MoO_3 interfacial layer, an increase in V_{OC} was observed, but only for devices with the thinner 6 nm SQ layer. The thickness of MoO_3 did not alter results very significantly, even with films as thin as 1 nm or as thick as 50 nm (see Appendix Figure A1). This suggests that the MoO_3/SQ interaction is influencing the V_{OC} rather than MoO_3 simply acting as a buffer layer between ITO and SQ. MoO_3 improved the FF for the 6 and 12 nm devices but does not significantly affect the 9 nm devices. The improved FF can be in part explained by the increase in shunt (parallel) resistance (R_P) although the series resistance does increase with the addition of MoO_3 (Table 1). The dark *JV* measurements (Figure 3) show a reduction in dark current with increasing d_{SQ} (and in the case of the 6 nm devices, the addition of MoO_3), consistent with a decrease in electron leakage.[23]

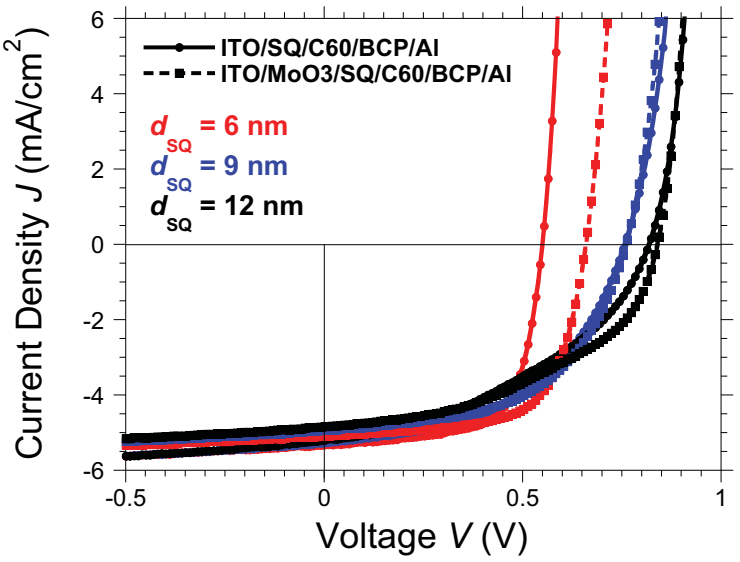

Figure 2 Current/voltage curves for devices measured under standard 1 sun conditions (AM 1.5 G, 100 mW/cm^2) Each device has the architecture ITO/SQ/C60/BCP/Al (●) or ITO/MoO3/SQ/C60/BCP/Al (■) with a the SQ thickness varied from 6 to 12 nm.

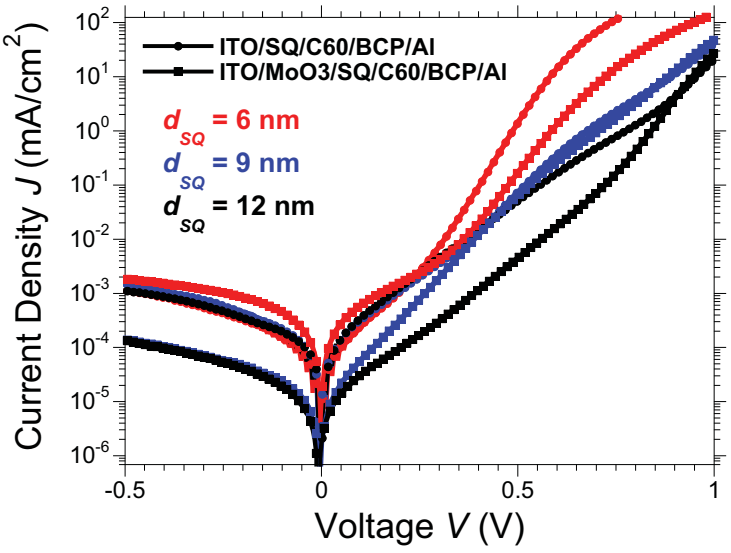

Figure 3 Semi-log plot of the dark current/voltage curves for each device shown in Figure 2. A noticeable decrease in the dark current with increasing d_{SQ} is noticeable.

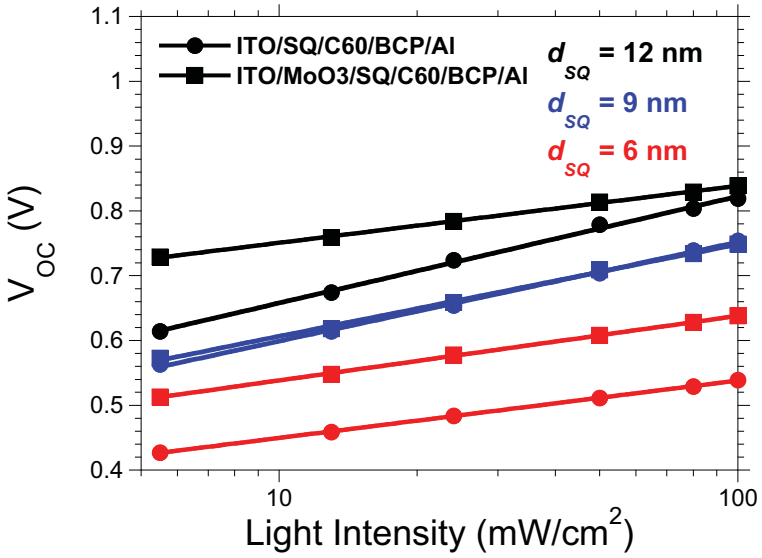

Figure 4 Light intensity dependence on the open-circuit voltage for each device. The data is fit using the linear relationship: V_{OC} = y + m(ln(LI)

In all cases, the device J_{SC} values showed a linear dependence with light intensity, with the power law relationship, $J_{SC} \sim LI^{\alpha}$, where α = 1, meaning none of the devices are limited by space charge. Plotting V_{OC} vs light intensity showed that it increased linearly with the log of light intensity, the slopes of these plots were then used to calculate the ideality factor based on the following relationship:

$$n_{id} = \frac{q}{kT}\frac{dV_{OC}}{dln(LI)} \qquad \textbf{(1)}$$

where q is the elementary charge, kT is the thermal energy. The ideality factor is an important parameter to understand how close to ideal the diode behaves and it also allows us to understand the influence of trap states on recombination.[24] In general the ideality factor is between 1 and 2, with an ideal trap-free device having n_{id} = 1. Increasing values of n_{id} correspond to the presence of trap states, with traps becoming deeper and more dominant as n_{id} gets closer to 2. Strangely in some

devices, the ideality factor supersedes 2, which has been described for inorganic devices to represent either coupled defect recombination or tunneling enhanced defect recombination,[25,26] both examples reflecting defect-induced recombination.

Table 1 Summary of the figures of merit for each device recorded under 1 Sun (100 mW/cm2) irradiation together with the ideality factor obtained from Equation1.

Device	V_{OC} V	J_{SC} mA/cm^2	FF	η %	R_S Ω/cm^2	R_P Ω/cm^2	n_{id}
ITO/SQ/C_{60}/BCP/Al							
d_{SQ} = 6 nm	0.55	5.34	0.67	1.97	96	7.7 x 10^7	1.49
d_{SQ} = 9 nm	0.76	5.27	0.49	1.96	81	5.7 x 10^7	2.56
d_{SQ} = 12 nm	0.82	5.20	0.41	1.77	96	5.8 x 10^7	2.76
ITO/MoO_3/SQ/C_{60}/BCP/Al							
d_{SQ} = 6 nm	0.66	5.09	0.66	2.22	154	2.6 x 10^7	1.67
d_{SQ} = 9 nm	0.76	4.93	0.55	2.05	117	3.9 x 10^8	2.38
d_{SQ} = 12 nm	0.84	4.83	0.47	1.95	114	5.7 x 10^8	1.47

Moving from steady state measurements to transient measurements we first look at the influence that the device architecture has on the charge generated in the active layers. Figure 4 shows the total charge per unit area (Q/cm^{-2}) in the device plotted *versus* bias. We see that the charge increases with increasing SQ thickness. The black line represents the average geometrical capacitive charges, which was calculated by carrying out CE under applied negative bias in the dark,[27] and corresponds to a geometrical capacitance of 67 nF/cm^2. For the thinnest devices, the total charge recorded is similar in magnitude to the charges at the electrode, meaning that the active layer builds up very little charge. Increasing the SQ thickness leads to a larger build up of active layer charge, implying an increase in the quasi-Fermi-level splitting at the SQ/C_{60} interface. Importantly, we see a change in the shape of the exponential between ITO and

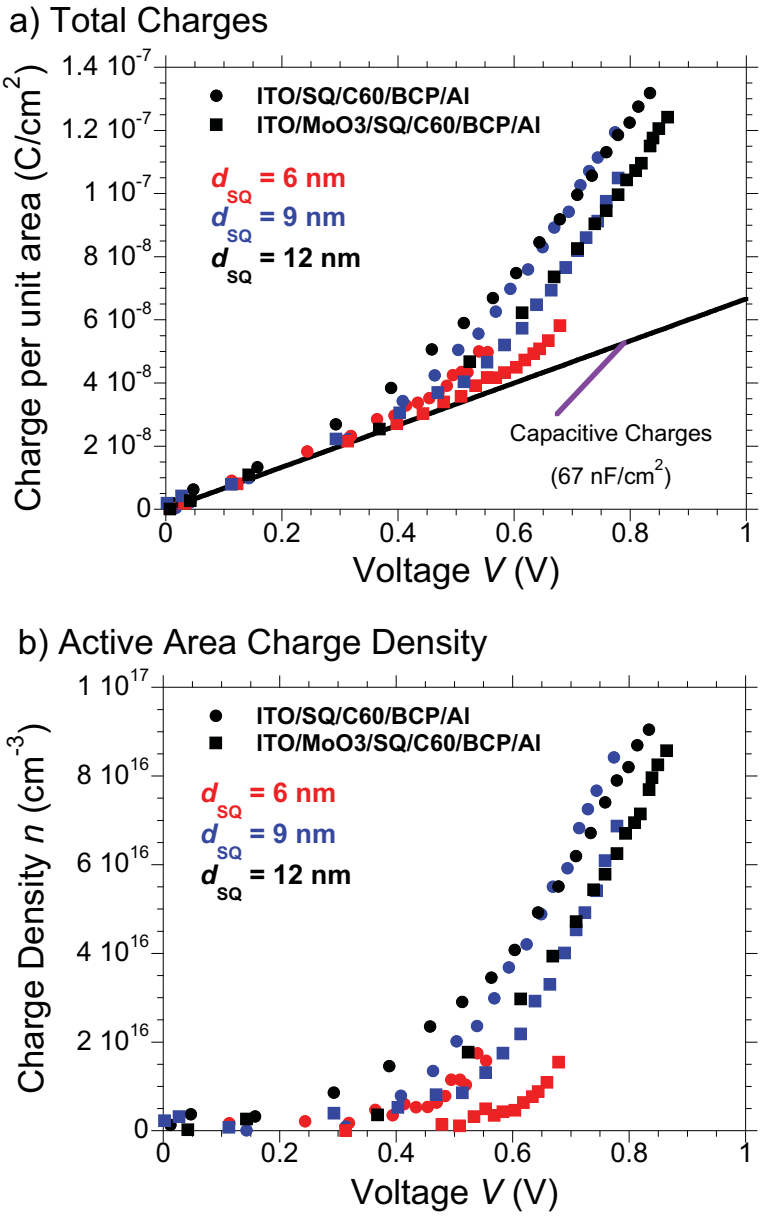

Figure 5 Charge extraction data showing the total charge stored in the device as a function of bias (a) and the charge carrier density present in the active layer (b).

MoO_3 devices, which we can relate to a shift in the density of states (DOS).[9] As mentioned above a 1 nm layer is sufficient to induce a change in the V_{OC} for the thin SQ films (d_{SQ} = 6 nm), and this coupled with the shift in the charge density *versus* bias provides further evidence that there is a chemical interaction between SQ and MoO_3 rather than MoO_3 simply acting as a physical barrier, consistent with previous studies on organic/MoO_3 intefaces.[28-30] Correcting for the geometrical charges,[27] the charge in the active layer, sometimes defined as the chemical charge,[31] is plotted in Figure 4 as a function of volume (*i.e.* charge carrier density). The data fit well to an exponential for values above 0.3 V with the following function:

$$n = n_0 e^{\gamma V_{OC}} \qquad \textbf{(2)}$$

with n being dependent on the applied bias (or splitting of quasi-Fermi levels).[32] The values of γ are very low suggesting no defined band edges as one would expect for an ideal semiconductor. The trend observed is that γ decreases with increasing SQ thickness, suggesting a more delocalized distribution of energy, we also see that there are slightly higher values of γ for the MoO_3 devices (see Table 2). However, due to the very thin nature of the active layer, the gradients of charge carrier concentration are very steep as a function of position that the effect of γ is difficult to interpret. The high charge density observed in these devices is interesting considering that many of the small molecule devices (BHJ and PHJ) reported in the literature and/or investigated in our lab tend to have very low chemical potentials, resulting in most of the charge density observed to arise from the geometrical capacitive charges.[7,8,27,33]

Small perturbation charge carrier lifetimes ($\tau_{\Delta n}$) are plotted versus bias in Figure 5, obtained from transient photovoltage (TPV) measurements and show an exponential decay with the function:

$$\tau_{\Delta n} = \tau_{\Delta n_0} e^{-\beta V_{OC}} \quad \textbf{(3)}$$

with, $\tau_{\Delta n_0}$ the lifetime of the charge carriers at short circuit, and β the decay constant. First looking at the d_{SQ} = 6 nm devices, we see that $\tau_{\Delta n}$ at ~1 Sun is shorter for the ITO device, consistent with the lower V_{OC} obtained for that device. The d_{SQ} = 9 nm devices have almost identical lifetimes, and are an order of magnitude longer lived than the d_{SQ} = 6 nm devices. Interestingly, the d_{SQ} = 12 nm devices have shorter lifetimes, suggesting the origin of the recombination may differ. Note the seemingly different slopes observed for the d_{SQ} = 12 nm ITO device. To fully understand this relationship we must compare the lifetimes to the charge density, because as we saw in Figure 4 the charge present in the device changes significantly. Correlating the lifetime and charge carrier density in Figure 5 has two important advantages, it decouples the charge recombination dynamics from the voltage highlighting the effect of the charge carrier distribution and it allows for devices of different architecture and materials to be compared. The ITO and MoO_3 devices with d_{SQ} = 6 nm, illustrate these points well, with a big difference evident when comparing their charge carrier density plotted *versus* voltage or charge density. While the device with the MoO_3 has a lower number of charges present in its active layer, the dependence of the carrier lifetime is far lower than that of the ITO device, which explains the higher V_{OC} observed in the *J-V* curve (Fig. 2a).

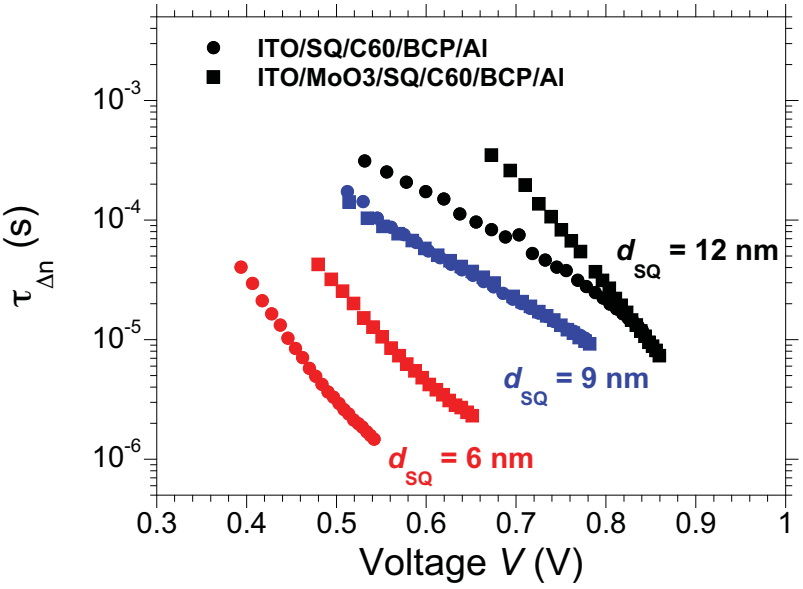

Figure 6 Small perturbation carrier lifetimes *versus* bias for each device recorded using the transient photovoltage method.

The exponential dependence of both charge density and carrier lifetime on voltage leads to the a power law relationship:

$$\tau_{\Delta n} \propto n^{-\lambda} \qquad \textbf{(4)}$$

with λ representing the power law relationship between the lifetimes of the charge carriers generated by the small perturbation and the charge density of the active area. A simple relationship exists between the kinetics of the small perturbation carrier lifetimes and the total carrier lifetime in the active layer which relies on λ; $\tau_n = \tau_{\Delta n}(\lambda + 1)$, where $\lambda + 1$ is the pseudo-first order rate of reaction.[34] In thick polymer:fullerene bulk heterojunctions, $\lambda + 1$ has been said to represent the empirical reaction order, and is on the order of 2, suggesting bimolecular recombination.[35] However, in the case of thin active layer devices, the relationship

between the order of reaction is always much higher than first or second order, due to a large gradient in carrier concentration, and other effects playing a role in determining λ, such as reactions at the contacts and energetic disorder.[24]

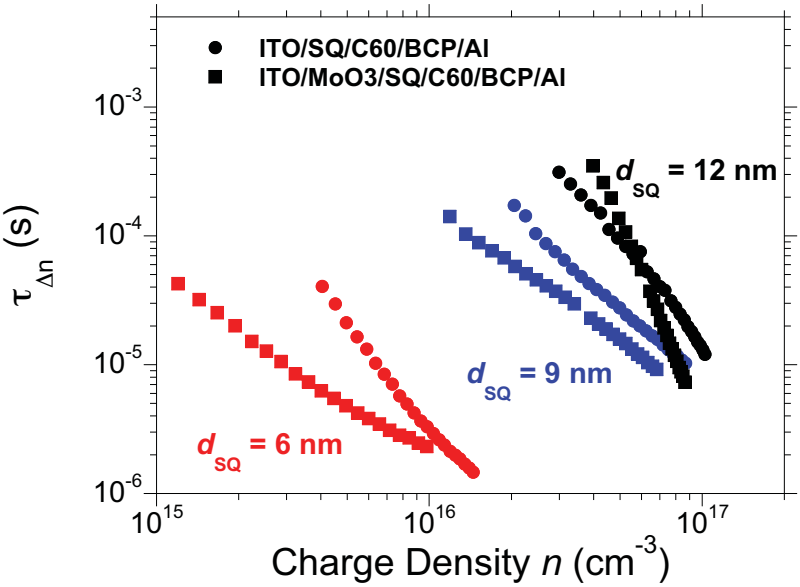

Figure 7 Small perturbation lifetimes plotted *versus* charge density by using the exponential fit obtained from the CE measurments for each device.

Device	n_0 (cm^{-3})	γ (V^{-1})	$\tau_{\Delta n_0}$ (s)	β (V^{-1})	λ
ITO/SQ/C_{60}/BCP/Al					
d_{SQ} = 6 nm	1.37 x 10^{-14}	8.60	0.034	18.37	2.14
d_{SQ} = 9 nm	1.35 x 10^{-15}	5.46	0.018	9.65	1.77
d_{SQ} = 12 nm	3.58 x 10^{-15}	3.99	0.99	13.44	3.67
ITO/MoO_3/SQ/C_{60}/BCP/Al					
d_{SQ} = 6 nm	3.38 x 10^{-12}	12.24	0.014	13.37	1.09
d_{SQ} = 9 nm	4.16 x 10^{-14}	6.52	0.045	10.85	1.66
d_{SQ} = 12 nm	2.44 x 10^{-15}	4.15	2445	22.83	5.50

The thin film morphology of SQ was also studied using atomic force microscopy (AFM) to see whether there was any significant change in the surface topography with increasing SQ thickness. No major change was observed between the films. The root mean square roughness of ITO is ~4 nm, and changes very little for the SQ films deposited on it, nor is there any difference of SQ topography on MoO_3.The rms roughness is on the same order as the thickness of the SQ film, and this topography illustrates that the SQ/C_{60} interface is not simply the ideal flat bilayer we imagine for a planar heterojunction device, but a rather rough, bulk-like heterojunction. Another point to consider is the thin nature of the SQ films deposited and it is easy to see that there are regions where the C_{60} may be in extremely close contact with the electrode; close enough for surface recombination to occur. Increasing the thickness of SQ, however reduces the possibility of electrons recombining at the wrong electrode and would help explain the higher V_{OC} observed.

4. Discussion

Changing the thickness of the SQ layer changed the V_{OC} significantly and through the transient optoelectronic measurements presented above we can explain this by considering two factors, one being the charge carrier density and the other being the charge carrier lifetime. Increasing the thickness of the SQ increases the charge density generated in the active layer of the devices, which is related to an improved splitting of the quasi-Fermi levels. Going from d_{SQ} = 6 nm to d_{SQ} = 9 nm, in addition to the increased potential difference between the SQ and C_{60} quasi-Fermi levels there is also a significant increase in the charge carrier lifetime and decrease in the decay order. Therefore, we have a higher number of charges, which also live longer and thus explain the higher V_{OC} observed. Increasing the SQ thickness further, we generate slightly more free charge carriers, which also have slightly longer lifetimes but a higher decay order, leading to an increase in V_{OC} but not as

significant as in the first increment. The changes in the order of decays observed from the TPV measurements hint at different recombination processes dominating the device. For the thin SQ layers, it is surface recombination that is limiting the V_{OC}, which becomes less significant through the addition of a MoO_3 layer and even less so when the thickness of the SQ layer is increased.

The effect of a MoO_3 hole transport layer (HTL) has been investigated in the past for several different donor materials, in particular for planar heterojunction devices and has been shown to increase the V_{OC} when certain donors have been employed but not for others.[23,36,37] Here, for the SQ/C_{60} devices, we see that MoO_3 only plays a significant role in improving the V_{OC} for the thin SQ layers. Comparing this finding with previous reports, most of the devices that showed improved V_{OC} by employing MoO_3 utilized donor molecules with low exciton diffusion lengths, which of course imposed a limit to how thick the films could be made. In our study, when we increase the SQ layer thickness to values much higher than the exciton diffusion length we are in effect creating a two tier film, where the one closest to ITO is simply acting to isolate the SQ/C_{60} interface from the electrode, preventing unwanted surface recombination; in other words an electron blocking layer (EBL). Therefore the MoO_3 is made almost redundant, although it does offer improved shunt resistance, which leads to better FF, which can be explained by providing a more homogeneous film as ITO films tend to be electrically quite inhomogeneous.[38]

The fact that the V_{OC} is dependent on the anode material (at least for the low SQ thicknesses) cannot be explained if we assume a perfect bilayer structure. To illustrate this, we performed drift-diffusion simulations of bilayers and varied the energetic distance φ_{an}between the Fermi level and the valence band edge at the

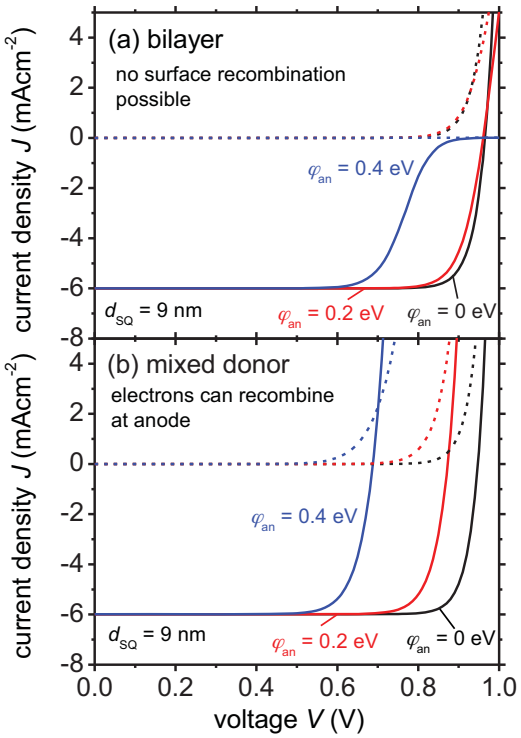

Figure 8 Drift-diffusion simulations to illustrate the effect of changing the anode workfunction on the current/voltage curve of (a) a bilayer solar cell and (b) as solar cell with a donor layer that allows electrons to travel efficiently to the anode. In the case of a perfect bilayer, recombination of electrons at the anode is impossible and therefore the V_{OC} is unaltered. However, S-shapes occur if φ_{an} (the distance from the Fermi-level to valence band edge at the anode) becomes too large, because charges have to diffuse against the electric field to be collected close to open circuit conditions. In case of a mixed donor layer that allows electron transport, surface recombination is possible and the V_{OC} will decrease when φ_{an} becomes too large.

anode to simulate the effect of changing the anode workfunction. From the simulations shown in Figure 8a, we can see that the open circuit voltage is not affected by the workfunction and therefore the value of φ_{an} at all. However, at sufficiently high values of φ_{an}, the V_{OC} will exceed the built-in voltage at some point and S-shaped current voltage curves are expected because the majority carriers have to diffuse against the electric field to be collected.[39] Yet, in the

experimental data, we neither observe S-shapes nor an insensitivity of V_{OC} on the anode material. Thus, we also studied the case where the donor material does not present a barrier for electron transport from the C_{60} to the anode. For this purpose we just align the conduction band in the nominally pure SQ layer to the conduction band of the C_{60}. Allowing the electrons to travel freely to the anode and recombine there will lead to a strong dependence of V_{OC} on the workfunction of the anode as seen in Figure 8b.[6] However, it will still not explain the strong dependence of V_{OC} on the thickness of the SQ layer. In fact the thickness should hardly affect the open-circuit voltage at all. In addition, it is still unclear why the FF of the devices with thicker SQ layers would be substantially worse than the ones with thinner SQ layers.

A tentative explanation for the observed trend with thickness is a transition between a device that behaves like a bilayer at high SQ thicknesses and a device where recombination of electrons at the anode is easily possible at low SQ thicknesses. The observed current/voltage curves could be understood as the parallel connection of a solar cell limited by surface recombination (low V_{OC} but good FF) and a solar cell that is not limited by surface recombination allowing a much higher V_{OC}. Normally, the parallel connection of two solar cells with different V_{OC} would lead to a combined current/voltage curve with a V_{OC} dominated by the lower of the two. However, the higher V_{OC} might dominate the total performance if the regions with high recombination are either electrically isolated with high series resistances,[40] or if they contribute only a small part to the total area of the device. In these cases, the areas with high surface recombination would act like a non-linear shunt for the rest of the device.

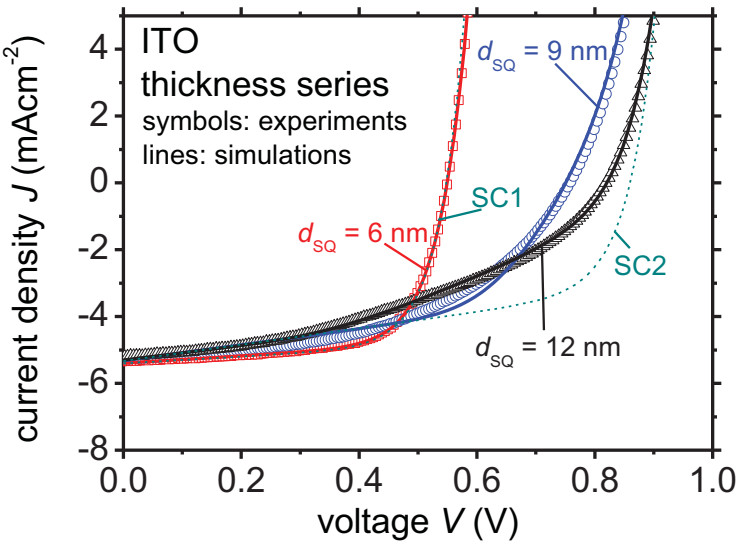

Figure 9 The changes in current/voltage curves observed with increased SQ thickness are explained here with a parallel connection of two diodes (see Eq. (5)) with different V_{OC} (SC1 and SC2) in different ratios and with different series resistances associated with each diode. In this interpretation of the data, the change in SQ thickness means that the influence of the shunt diode caused by surface recombination (SC1) that controls the device with d_{SQ} = 6 nm is more and more suppressed for higher d_{SQ}.

Figure 9 illustrates that using a parallel connection of two solar cells in different ratios and with different series resistances, it is possible to reproduce the experiment. For Figure 9, we used two illuminated diode equations of the type:

$$J = J_0 \left[\exp\left(\frac{q[V - JR_s]}{n_{id} kT} \right) - 1 \right] - J_{sc} + \frac{V - JR_s}{R_p} \qquad \textbf{(5)}$$

where R_s is the series resistance, R_p the parallel resistance and J_0 the saturation current density. The two diode equations are drawn in green dashed lines and are labeled SC1 and SC2. Here, SC1 represents the diode limited by surface recombination of electrons and the anode and SC2 represents the bilayer where no

surface recombination can occur. The experimental current/voltage curve for d_{SQ} = 6 nm can then be fitted by assuming that SC1 dominates the system. The experimental current/voltage for larger SQ thicknesses are fitted by assuming that we connect SC1 and SC2 in parallel and that we vary the series resistance of SC1 as well as the ratio of the area that is made up by SC2 and the area where electrons can reach the anode (SC1).

Because the model is quite a crude and simplistic approximation to reality and as the influence of series resistance and the ratio of areas are interchangeable to a certain degree, the parameters obtained from the fit are not particularly meaningful. However, the simple model suggests that the observed current/voltage curves can neither be understood using the picture of a perfect bilayer with suppressed surface recombination nor the picture of a bulk heterojunction, where surface recombination is allowed. Instead, the trends in thickness seem to originate from a transition between two limiting situations. While at low SQ thicknesses, the anode is able to limit V_{OC} due to high surface roughness and or some interdiffusion of C_{60} into the SQ layer, this loss pathway gradually disappears with increasing SQ thickness. While the influence of the shunt diode does not affect the V_{OC} much at high SQ thickness it still does affect the FF and therefore has an important influence on the device performance. Alternative explanations for the reduced FF at high SQ thicknesses would be field dependent geminate effects as discussed for instance in references [41-43]. These effects cannot be ruled out but they cannot alone be responsible for the observed trends. While geminate effects might have a slight effect on V_{OC} in theory, the changes in V_{OC} observed here are accompanied by changes in the dark current that could not be explained by geminate recombination.

5. Conclusions

Through tuning the SQ donor layer thickness we observed a large change in the open-circuit voltage. For the thinnest films studied, d_{SQ} = 6 nm, the V_{OC} was significantly improved by employing a MoO_3 hole transport layer. However, increasing the thickness of SQ, the MoO_3 did not improve the V_{OC}, evidence that the thin SQ/C_{60} devices suffer from surface recombination, i.e. electrons from C_{60} recombining with the ITO electrode. Once a sufficiently thick SQ layer is employed the C_{60} is isolated from ITO and thus the MoO_3 layer as an EBL is made redundant. Through transient optoelectronic techniques we could study the increased chemical potential in the device with increasing SQ thickness, and the consequent effect on charge carrier lifetime. Although V_{OC} could be improved significantly with increasingly thicker SQ layers the pay off was a lower FF. Through modeling the devices using drift-diffusion simulations we showed that the change in V_{OC} observed for d_{SQ} = 6 nm when adding a MoO_3 interfacial layer cannot be explained by assuming a planar heterojunction, but the behavior is more bulk-heterojunction like. A basic two diode model was also used, which illustrated the transition from a more BHJ -like active layer limited by surface recombination, and having low V_{OC}, towards a more PHJ-like with suppressed surface recombination and higher V_{OC}.

6. References

1. Z. He, C. Zhong, S. Su, M. Xu, H. Wu and Y. Cao, *Nature Photonics*, 2012, **6**, 591-595.
2. J. You, L. Dou, K. Yoshimura, T. Kato, K. Ohya, T. Moriarty, K. Emery, C.-C. Chen, J. Gao, G. Li and Y. Yang, *Nat Commun*, 2013, **4**, 1446.
3. A. K. K. Kyaw, D. H. Wang, V. Gupta, J. Zhang, S. Chand, G. C. Bazan and A. J. Heeger, *Advanced Materials*, 2013, **25**, 2397-2402.
4. D. Credgington and J. R. Durrant, *The Journal of Physical Chemistry Letters*, 2012, **3**, 1465-1478.

5. D. Credgington, R. Hamilton, P. Atienzar, J. Nelson and J. R. Durrant, *Advanced Functional Materials*, 2011, **21**, 2744-2753.
6. R. Xia, D.-S. Leem, T. Kirchartz, S. Spencer, C. Murphy, Z. He, H. Wu, S. Su, Y. Cao, J. S. Kim, J. C. deMello, D. D. C. Bradley and J. Nelson, *Advanced Energy Materials*, 2013, doi: 10.1002/aenm.201200967.
7. A. Sánchez-Díaz, L. Burtone, M. Riede and E. Palomares, *The Journal of Physical Chemistry C*, 2012, **116**, 16384-16390.
8. A. Foertig, A. Wagenpfahl, T. Gerbich, D. Cheyns, V. Dyakonov and C. Deibel, *Advanced Energy Materials*, 2012, **2**, 1483-1489.
9. M. Bolognesi, A. Sanchez-Diaz, J. Ajuria, R. Pacios and E. Palomares, *Physical Chemistry Chemical Physics*, 2011, **13**, 6105-6109.
10. L. Hu, Z. Yan and H. Xu, *RSC Advances*, 2013, **3**, 7667-7676.
11. A. Ajayaghosh, *Accounts of Chemical Research*, 2005, **38**, 449-459.
12. M. Tian, M. Furuki, I. Iwasa, Y. Sato, L. S. Pu and S. Tatsuura, *The Journal of Physical Chemistry B*, 2002, **106**, 4370-4376.
13. D. Bagnis, L. Beverina, H. Huang, F. Silvestri, Y. Yao, H. Yan, G. A. Pagani, T. J. Marks and A. Facchetti, *Journal of the American Chemical Society*, **132**, 4074-+.
14. L. Beverina, M. Drees, A. Facchetti, M. Salamone, R. Ruffo and G. A. Pagani, *European Journal of Organic Chemistry*, 2011, 5555-5563.
15. B. Fan, Y. Maniglio, M. Simeunovic, S. Kuster, T. Geiger, R. Hany and F. Nuesch, *International Journal of Photoenergy*, 2009, **2009**, Article ID 581068.
16. U. Mayerhoffer, K. Deing, K. Gruss, H. Braunschweig, K. Meerholz and F. Wurthner, *Angewandte Chemie-International Edition*, 2009, **48**, 8776-8779.
17. S. So, H. Choi, H. M. Ko, C. Kim, S. Paek, N. Cho, K. Song, J. K. Lee and J. Ko, *Solar Energy Materials and Solar Cells*, 2012, **98**, 224-232.
18. S. Y. Wang, E. I. Mayo, M. D. Perez, L. Griffe, G. D. Wei, P. I. Djurovich, S. R. Forrest and M. E. Thompson, *Applied Physics Letters*, 2009, **94**, 23304.
19. G. D. Wei, X. Xiao, S. Y. Wang, K. Sun, K. J. Bergemann, M. E. Thompson and S. R. Forrest, *Acs Nano*, 2012, **6**, 972-978.
20. G. D. Wei, X. Xiao, S. Y. Wang, J. D. Zimmerman, K. Sun, V. V. Diev, M. E. Thompson and S. R. Forrest, *Nano Letters*, 2011, **11**, 4261-4264.

21. G. Chen, H. Sasabe, Z. Wang, X.-F. Wang, Z. Hong, Y. Yang and J. Kido, *Advanced Materials*, 2012, **24**, 2768-2773.
22. G. Chen, D. Yokoyama, H. Sasabe, Z. Hong, Y. Yang and J. Kido, *Applied Physics Letters*, 2012, **101**, 083904.
23. N. Li, B. E. Lassiter, R. R. Lunt, G. Wei and S. R. Forrest, *Applied Physics Letters*, 2009, **94**, 023307.
24. T. Kirchartz and J. Nelson, *Physical Review B*, 2012, **86**, 165201.
25. S. Steingrube, O. Breitenstein, K. Ramspeck, S. Glunz, A. Schenk and P. P. Altermatt, *Journal of Applied Physics*, 2011, **110**, 014515.
26. U. Rau, *Applied Physics Letters*, 1999, **74**, 111-113.
27. D. Credgington, Y. Kim, J. Labram, T. D. Anthopoulos and J. R. Durrant, *The Journal of Physical Chemistry Letters*, 2011, **2**, 2759-2763.
28. T. Matsushima, G. H. Jin, Y. Kanai, T. Yokota, S. Kitada, T. Kishi and H. Murata, *Organic Electronics*, 2011, **12**, 520-528.
29. T. Matsushima, Y. Kinoshita and H. Murata, *Applied Physics Letters*, 2007, **91**, 253504.
30. M. C. Gwinner, R. D. Pietro, Y. Vaynzof, K. J. Greenberg, P. K. H. Ho, R. H. Friend and H. Sirringhaus, *Advanced Functional Materials*, 2011, **21**, 1432-1441.
31. J. Bisquert, *Physical Chemistry Chemical Physics*, 2003, **5**, 5360-5364.
32. A. Maurano, C. G. Shuttle, R. Hamilton, A. M. Ballantyne, J. Nelson, W. Zhang, M. Heeney and J. R. Durrant, *The Journal of Physical Chemistry C*, **115**, 5947-5957.
33. A. Sánchez-Díaz, R. Pacios, U. Muñecas, T. Torres and E. Palomares, *Organic Electronics*, **12**, 329-335.
34. B. C. O'Regan, J. R. Durrant, P. M. Sommeling and N. J. Bakker, *The Journal of Physical Chemistry C*, 2007, **111**, 14001-14010.
35. C. G. Shuttle, B. O'Regan, A. M. Ballantyne, J. Nelson, D. D. C. Bradley and J. R. Durrant, *Physical Review B*, 2008, **78**, 113201.
36. I. Hancox, P. Sullivan, K. V. Chauhan, N. Beaumont, L. A. Rochford, R. A. Hatton and T. S. Jones, *Organic Electronics*, 2010, **11**, 2019-2025.
37. Y. Kinoshita, R. Takenaka and H. Murata, *Applied Physics Letters*, 2008, **92**, 243309.

38. I. Hancox, K. V. Chauhan, P. Sullivan, R. A. Hatton, A. Moshar, C. P. A. Mulcahy and T. S. Jones, *Energy & Environmental Science*, 2010, **3**, 107-110.
39. T. Kirchartz, W. Gong, S. A. Hawks, T. Agostinelli, R. C. I. MacKenzie, Y. Yang and J. Nelson, *The Journal of Physical Chemistry C*, 2012, **116**, 7672-7680.
40. U. Rau, P. O. Grabitz and J. H. Werner, *Applied Physics Letters*, 2004, **85**, 6010-6012.
41. J. A. Barker, C. M. Ramsdale and N. C. Greenham, *Physical Review B*, 2003, **67**, 075205.
42. A. Petersen, A. Ojala, T. Kirchartz, T. A. Wagner, F. Würthner and U. Rau, *Physical Review B*, 2012, **85**, 245208.
43. C. Schwarz, S. Tscheuschner, J. Frisch, S. Winkler, N. Koch, H. Bässler and A. Köhler, *Physical Review B*, 2013, **87**, 155205.

7. Appendix

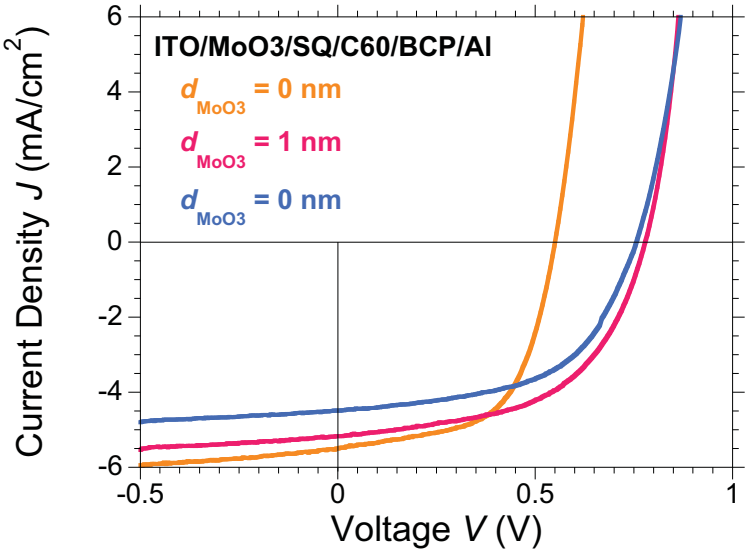

Figure A1 JV curves for devices with 6 nm SQ and different thicknesses of MoO_3. Using as thin as 1 nm MoO_3 we still get a large shift in V_{OC}. Increasing the thickness of MoO_3 to 50 nm produces a similar V_{OC} but the photocurrent does decrease significantly.

Chapter 4
Small Molecule Solar Cells Based on a Series of Water Soluble Zinc Phthalocyanine Donors

1. Introduction

Small molecule organic solar cells (SMOSCs) have made great strides in recent years,[1,2] especially in the case of solution processed devices,[3] with a record efficiency of 6.7%.[4] However, to date, the range of efficient small molecule donors described in the literature is quite limited due to the difficulty in first synthesising a soluble molecule with semiconductor properties followed by successfully retaining its optoelectronic properties when incorporated into a device.

Phthalocyanine (Pc) donors have been shown to produce relatively efficient SMOSCs,[5,6] with recent solution processed small molecule bulk heterojunctions utilising Pc donors showing efficiencies of 0.8% using a zinc Pc (ZnPc) derivative and 1.6% with a ruthenium Pc (RuPc) oligothiophene complex.[7,8] Pcs are ideal sensitisers, with outstanding absorption in the near IR region; yet their use in SMOSCs, as with any efficient SMOSCs, has involved organic chlorinated solvents to perform the deposition of the active layers. Ideally, organic films fabricated using solution process techniques should avoid the use of environmentally inconvenient solvents, such as chlorinated solvents (e.g.

chlorobenzene, dichloromethane, etc.) to reduce health risks and become even more environmentally friendly.[9,10]

Based on these factors, Jones and co-workers reported a significant finding based on a water-soluble tetrasulfonated copper Pc (CuPc-S4) that provides a route to removing chlorinated solvents in the fabrication of a SMOSCs.[11] Thus, they showed that it is possible to produce devices where part of the active area has been prepared from aqueous CuPc-S4 solutions, with the acceptor layer being prepared using moderate-vacuum deposition techniques due to the poor solubility of C_{60} molecules in water. The devices showed a light-to-energy conversion under standard conditions of 0.32%. Interestingly in the work mentioned above, there was no contribution of photocurrent from the CuPc-S4 donor, which severely limited the device photocurrent (*J*sc) and in turn the power conversion efficiency (η). Considering this lack of photocurrent, it seems obvious that a significant margin for improvement in device performance exists.

Krebs and co-workers have also shown encouraging results fabricating organic solar cells (OSCs) based on polymer–fullerene heterojunctions where some or all of the layers were processed using aqueous solutions, with efficiencies as high as 0.7%.[12-15] However unlike CuPc-S4, the active layers were not directly water soluble, and required the use of chlorinated solvents or fluorinated surfactants prior to dispersing them in an aqueous solution. Nonetheless this collection of work provides promising routes towards greener OSCs.

Following on from the work of Jones, we report on a series of anionic water-soluble ZnPc (wsZnPc) derivatives with varying numbers of sulfonate substituents at the periphery of the macrocycle (Figure 1). By altering the number of substituents we aimed to shift the frontier orbital energies and significantly alter

the device characteristics. First of all, we observed that the tetrasulfonated ZnPc (ZnPc-S4) fails to contribute to the photocurrent akin to the CuPc-S4 analogue. Nonetheless, by decreasing the number of substituents to two or three sulfonate groups, it was possible to observe a contribution of wsZnPc to the photocurrent. This increase in J_{SC} was accompanied by a noticeable decrease in open circuit voltage, V_{OC}. The best donor molecule is shown to be the disulfonated ZnPc (ZnPc-S2), recording an efficiency of up to 0.46% at 1 sun (100 mW using sun simulated AM 1.5 G spectrum), which represents a significant improvement.

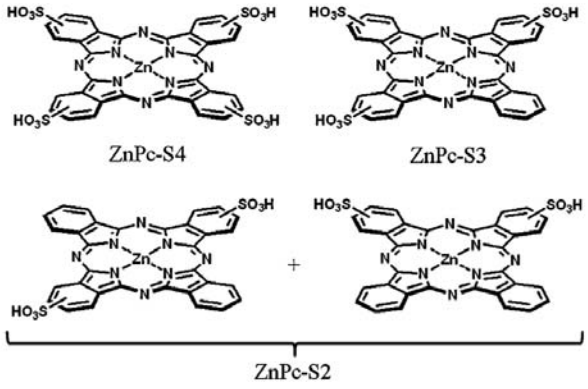

Figure 1 Chemical structures of the three sulfonated ZnPc derivatives studied: ZnPc-S4, ZnPc-S3 and ZnPc-S2, the latter being a mixture of ABAB and A2B2 regioisomers.

2. Experimental

The sulfonated derivatives ZnPc-S2, ZnPc-S3 and ZnPc-S4 were prepared by condensation of 4-sulfonatophthalate and (when required, i.e., for ZnPc-S2 and ZnPc-S3) phthalic anhydride in a 1:1 ratio, following modified procedures from the literature.[16,17]

UV-Vis measurements were carried out using a Shimadzu UV-2401PC spectrophotometer equipped with a photomultiplier detector, double beam optics,

and D2 and W light sources. Photoluminescence measurements were obtained using on an Aminco-Bowman Series 2 Luminescence spectrofluorimeter equipped with a high voltage PMT detector and continuum Xe Light source.

Differential pulse voltammetry (DPV) experiments were carried out using a CH Instruments 660c Electrochemical Workstation, with a standard three-electrode setup employed that utilized a Pt disc working electrode, Pt wire working electrode and SCE reference electrode. A 0.1 M solution of tetrabutylammonium phosphate in DMSO was used as the background electrolyte. To determine the HOMO of the respective molecules, we employed the following formula of D'Andrade *et. al*:[18]

$$E_{HOMO} = -(1.4 \pm 0.1) \times (qV_{CV}) - (4.6 \pm 0.08)\ eV \qquad \textbf{(1)}$$

where, V_{CV} corresponds to the electric potential of the substrate vs. the ferrocene/ferrocenyl couple (Fc/Fc+).

Devices were prepared on ITO substrates (5 ohm/square, Psiotech Ltd. U.K.). The substrates were cleaned by sonicating in acetone and isopropanol, following this they were exposed to UV/O_3 for 20 min. Thin films of the sulfonated ZnPc donors were prepared by spin-coating a 10 mg/ml solution (Mill-Q ultrapure water) of the respective donor, which had been left overnight stirring at 50 °C, and filtered using a 0.2 mm cellulose acetate membrane. The spin-coating conditions employed were 2000 rpm for 1 minute. Subsequently, the films were allowed to dry for 30 min in ambient conditions before transferring to a nitrogen rich glove box, where they were annealed at a temperature of 100 °C for 15 min in an attempt to remove any residual water. Finally the substrates were placed in the evaporator where the C_{60} (40 nm, MER Corp., 99.9+%), BCP (8 nm, Sigma Aldrich), and Al (100 nm, Sigma Aldrich) were deposited at a base pressure of 1 x 10^{-6} mbar. Device *J-V*

curves were recorded using a 150 W solar simulator (Abet Technologies) at 1 sun conditions (AM 1.5, 100 mW/cm^2). Incident to photon current efficiency (IPCE) studies were carried out using a home-built system utilising a 150 W Oriel Xenon lamp as the light source.

3. Results and Discussion

Figure 2 shows the absorption spectra for the three wsZnPc molecules in water, ZnPc-S4 differs from the other two molecules in that it has a more dominant peak at 680 nm, with ZnPc-S3 and ZnPc-S2 having a higher peak at 640 nm, suggesting more aggregation. The photoluminescence (PL) emission and excitation spectra are shown in Figure 3 for each molecule in water. Taking the overlap between excitation and emission and converting to eV, we obtained the optical band-gap of the molecules. Differential pulse voltammetry (Figure 4) was used to calculate the oxidation potential of each molecule and then the HOMO energy by applying Eq.1, which together with the PL data gave the optical LUMO. The energy levels are identical for ZnPc-S3 and ZnPc-S2, with the HOMO and LUMO of ZnPc-S4 100 mV lower in energy.

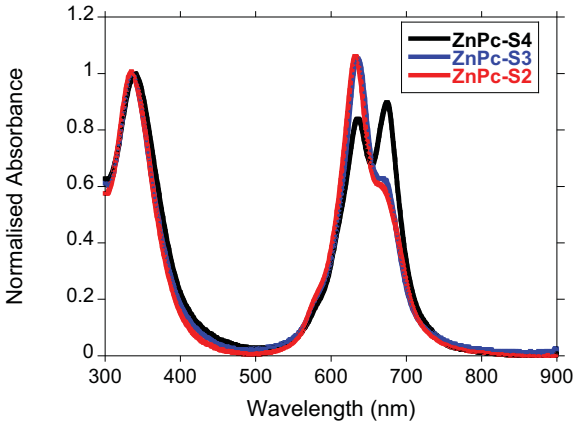

Figure 2 Absorption spectra for each molecule dissolved in water. The spectra are normalised at the Soret-band.

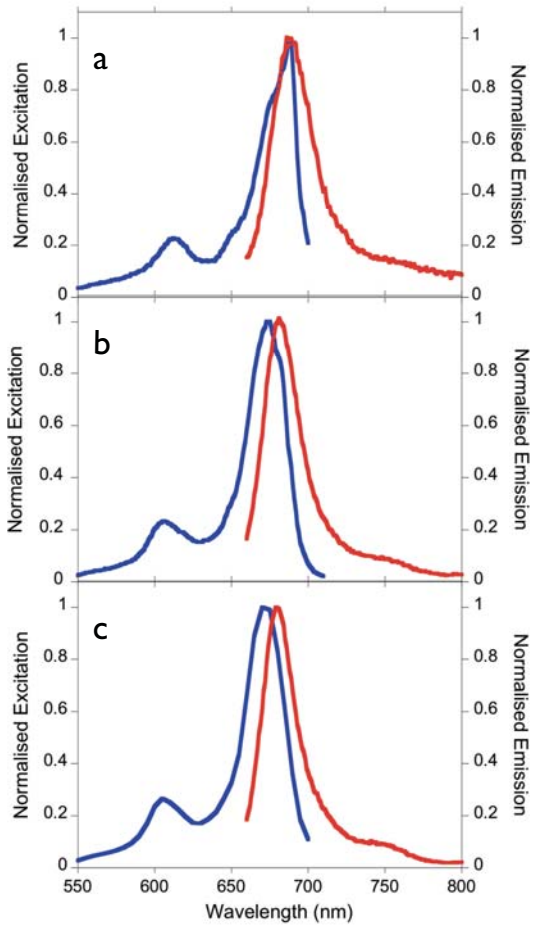

Figure 3 Photoluminescence emission (red) and excitation (blue) for ZnPc-S2 (a), ZnPc-S3 (b) and ZnPc-S4 (c)

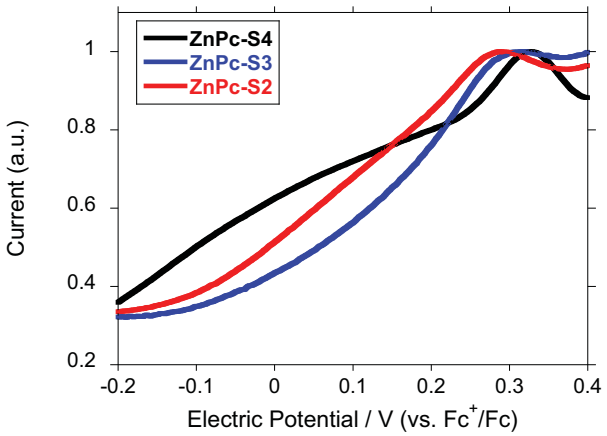

Figure 4 Differential pulse voltammetry for ZnPc-S2 (red), ZnPc-S3 (blue) and ZnPc-S4 (black), recorded *vs*. a Fc^{+}/Fc internal reference.

Turning to the device performance, the *J–V* curves for the respective devices differ significantly (Figure 5), resulting in very different V_{OC} and J_{SC} values. The standout result here is the significant increase in photocurrent with decreasing number of sulfonate substituents. The device comprising of ZnPc-S4 shows similar characteristics to those of the CuPc analogue (CuPc-S4) investigated by Jones and co-workers[11] (i.e. relatively high V_{OC} and very low J_{SC}), due to the inability of the device to extract the photogenerated charges from the donor layer. However, upon decreasing the number of substituents the photocurrent increases. The origin of the increase in photocurrent is clearly depicted in the incident photon to current efficiency (IPCE) spectra shown in Figure 6. For devices where ZnPc-S4 was employed the IPCE spectra show no photogenerated current in the spectral region where it absorbs. The di- and tri-sulfonated donor ZnPcs do however show a contribution to the device photocurrent. A similar effect of the degree of ZnPc sulfonation on photocurrent has been previously described for photo-electrochemical cells.[17]

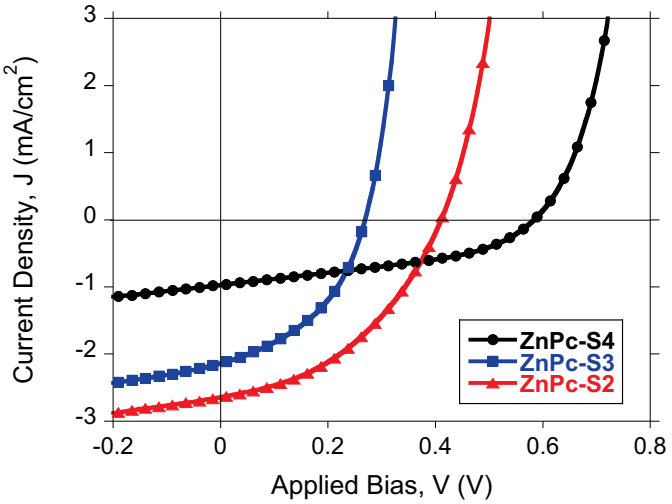

Figure 5 Current-voltage curves for devices comprising of ITO/wsZnPc/C_{60}/BCP/Al measured under standard conditions (AM 1.5 G, 100 mW/cm^2).

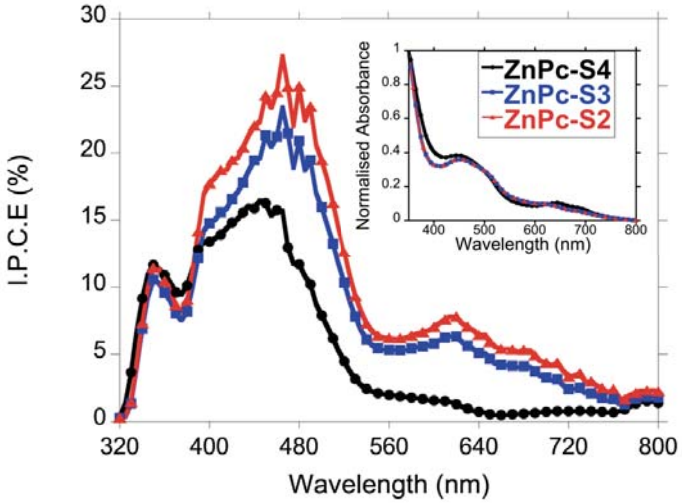

Figure 6 Incident photon to current efficiency (IPCE) spectra for each respective wsZnPc device. Inset shows the thin film absorption film spectra for bilayers of each wsZnPc with C_{60}, prepared in the same manner as the active layer for devices.

Table 1 Energy Levels and device performances for the series of water-soluble sensitisers. Device and architectures are all equal, with the structure ITO/wsZnPc/C_{60}/BCP/Al

Molecule	HOMO /eV	LUMO/eV	V_{OC}/V	J_{SC}/mA cm^{-2}	FF	η (%)
ZnPc-S4	-5.1	-3.3	0.57	0.97	0.40	0.22
ZnPc-S3	-5.0	-3.2	0.27	2.11	0.43	0.25
ZnPc-S2	-5.0	-3.2	0.46	2.66	0.42	0.46

One probable explanation for the lack of photocurrent from ZnPc-S4 arises from the small difference in energy between the Lowest Unoccupied Molecular Orbital (LUMO) of the ZnPc-S4 and the C60 LUMO. In OSCs, the photogenerated electron–hole pair (exciton) are bound by a Coulombic force, which is on the order of 0.3 eV. In order to separate charges, the general process requires excitons to travel to the donor–acceptor interface where the difference in donor and acceptor LUMO levels must exceed the Coulombic attraction force, i.e., the difference in donor and acceptor LUMO levels, ΔE_{LUMO}, has to exceed 0.3 eV. In the case of ZnPc-S4, the LUMO energy is 3.3 eV, whereas ZnPc-S3 and ZnPc-S4 both have LUMO energies of 3.2 eV (Table 1). Comparison of these values with the energy of the C60 LUMO, 3.5 eV,[19] shows that the photocurrent differences observed may simply be explained by a lack of free energy at the ZnPc-S4–C_{60} interface. Here however, the values we present for the LUMO energies are for isolated molecules, which do not represent the interfacial electronic interactions present in the device.[20] A more detailed study on each wsZnPc–C_{60} interface is therefore required to confirm this hypothesis.

Studying the morphology of the wsZnPc films using atomic force microscopy (AFM) provides further insights into the role sulfonation plays in controlling device performance. The AFM measurements on films prepared on ITO in exactly

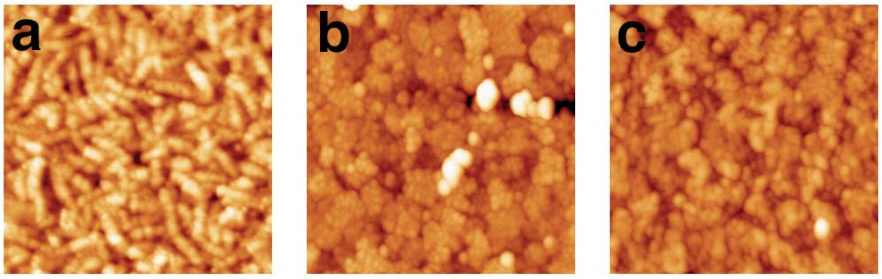

Figure 7 AFM images (2 x 2 μm) for ZnPc-S4 (a), ZnPc-S3 (b) and ZnPc-S2 (c) thin films on ITO with route-mean square roughness values of 3.0, 9.3 and 5.8 nm, respectively. The *Z*-scale is 20 nm for (a) and 50 nm for both (b) and (c).

the same we prepared them for devices, are presented in Figure 6. A clear difference between the morphology of ZnPc-S4 and the di- and tri-sulfonated ZnPc films is seen, with ZnPc-S4 forming large crystalline domains as opposed to the more 'grainy' morphology of ZnPc-S2 and ZnPc-S3. The roughness of the former is also much lower, with a route-mean square roughness (RMS) of 3.0 nm as opposed to 5.8 and 9.3 nm for the di- and tri-sulfonated ZnPc films. The high RMS of ZnPc-S3 films may explain the low V_{OC} as they are on the order of the film thickness and may lead to contact between ITO and C_{60}. The trends made here regarding morphology correlate well with the device performance values and suggest that morphology plays a key role in determining the photocurrent in these devices, as well as the photovoltage. The morphology of the thin-films may also affect the interfacial electronic interactions with C_{60}, which would tie in with our earlier hypothesis that the problem with photocurrent generation in ZnPc-S4 is a thermodynamic one. We would like to remark that increasing the thickness of the wsZnPc layers led to a decrease in performance (data not shown) in agreement with the case of tetra-sulfonated CuPc,[11] suggesting a low exciton diffusion length for these molecules.

Turning to the relationship between the degree of sulfonation and the device V_{OC}, it is important to note that it is not directly related with the degree of sulfonation, being highest for ZnPc-S4, lowest for ZnPc-S3 and ZnPc-S2 having a value in between. It is worth mentioning that the 100 mV difference in energy between the Highest Occupied Molecular Orbital (HOMO) of ZnPc-S2 and ZnPc-S3 does correspond well to the 110 mV difference in V_{OC} (Table 2). Nonetheless, the origin of the device V_{OC} in OSCs is still under active debate, with many attempts at understanding it being reported in recent years.[21-24] In general, the device V_{OC} is proportional to the difference in energy between the HOMO of the donor and the LUMO of the acceptor, ΔE_{DA}, yet the molecules used here all possess very similar HOMO energies. In this respect we would expect the device V_{OC} to be lowest for ZnPc-S2, as it possesses the lowest ΔE_{DA}. Therefore, we speculate several loss processes to exist that lead to the lower device V_{OC} observed for ZnPc-S2 and ZnPc-S3, especially considering the very different morphologies observed with the AFM study. Further characterisation of the charge transfer processes occurring in the device, under working conditions, is still under active investigation and is out of the scope of this communication. Here we have focused on prototyping a more effective SMOSC that employs a water-soluble donor sensitiser capable of contributing to the device photocurrent.

4. Conclusions

In conclusion, we have shown that the role of the substituents in ZnPc molecules is paramount for tuning the performance of OSCs based on water-soluble Pcs. This finding has led to a significant improvement in device performance by tuning the energy levels of the donor ZnPc to achieve a more energetically favourable photooxidation of the C60 acceptor layer, resulting in maximum efficiencies of 0.46% under standard conditions. Also, the number of substituents controls the morphology of the thin films, which in turn affects device performance. Having

successfully demonstrated our first goal, the next step will be to develop a water-soluble acceptor molecule, in order to provide both an environmentally friendly and an inexpensive route towards functional OSCs.

5. References

1. Y.-q. Zheng, J. William J. Potscavage, T. Komino, M. Hirade, J. Adachi and C. Adachi, *Applied Physics Letters*, 2013, **102**, 143304.
2. G. Wei, R. R. Lunt, K. Sun, S. Wang, M. E. Thompson and S. R. Forrest, *Nano Letters*, 2010, **10**, 3555-3559.
3. B. Walker, C. Kim and T.-Q. Nguyen, *Chemistry of Materials*, 2011, **23**, 470-482.
4. Y. Sun, G. C. Welch, W. L. Leong, C. J. Takacs, G. C. Bazan and A. J. Heeger, *Nature Materials*, 2012, **11**, 44-48.
5. G. Bottari, G. de la Torre, D. M. Guldi and T. Torres, *Chemical Reviews*, 2010, **110**, 6768-6816.
6. M. Victoria Martinez-Diaz, G. de la Torrea and T. Torres, *Chemical Communications*, 2010, **46**, 7090-7108.
7. M. K. R. Fischer, I. Lopez-Duarte, M. M. Wienk, M. V. Martinez-Diaz, R. A. J. Janssen, P. Baeuerle and T. Torres, *Journal of the American Chemical Society*, 2009, **131**, 8669-8676.
8. A. Sanchez-Diaz, R. Pacios, U. Munecas, T. Torres and E. Palomares, *Organic Electronics*, 2011, **12**, 329-335.
9. S. Hellweg, U. Fischer, M. Scheringer and K. Hungerbuhler, *Green Chemistry*, 2004, **6**, 418-427.
10. A. M. Ruder, in *Living in a Chemical World: Framing the Future in Light of the Past*, eds. M. A. Mehlman, M. Soffritti, P. Landrigan, E. Bingham and F. Belpoggi, 2006, vol. 1076, pp. 207-227.
11. S. Schumann, R. A. Hatton and T. S. Jones, *Journal of Physical Chemistry C*, 2011, **115**, 4916-4921.

12. T. R. Andersen, T. T. Larsen-Olsen, B. Andreasen, A. P. L. Bottiger, J. E. Carle, M. Helgesen, E. Bundgaard, K. Norrman, J. W. Andreasen, M. Jorgensen and F. C. Krebs, *Acs Nano*, 2011, **5**, 4188-4196.
13. T. T. Larsen-Olsen, T. R. Andersen, B. Andreasen, A. P. L. Bottiger, E. Bundgaard, K. Norrman, J. W. Andreasen, M. Jorgensen and F. C. Krebs, *Solar Energy Materials and Solar Cells*, 2012, **97**, 43-49.
14. T. T. Larsen-Olsen, B. Andreasen, T. R. Andersen, A. P. L. Bottiger, E. Bundgaard, K. Norrman, J. W. Andreasen, M. Jorgensen and F. C. Krebs, *Solar Energy Materials and Solar Cells*, 2012, **97**, 22-27.
15. R. Sondergaard, M. Helgesen, M. Jorgensen and F. C. Krebs, *Advanced Energy Materials*, 2011, **1**, 68-71.
16. H. Ali, R. Langlois, J. R. Wagner, N. Brasseur, B. Paquette and J. E. Vanlier, *Photochemistry and Photobiology*, 1988, **47**, 713-717.
17. A. Siejak, D. Wróbel, P. Siejak, B. Olejarz and R. M. Ion, *Dyes and Pigments*, 2009, **83**, 281-290.
18. B. W. D'Andrade, S. Datta, S. R. Forrest, P. Djurovich, E. Polikarpov and M. E. Thompson, *Organic Electronics*, 2005, **6**, 11-20.
19. R. Schwedhelm, L. Kipp, A. Dallmeyer and M. Skibowski, *Physical Review B*, 1998, **58**, 13176-13180.
20. H. Ishii, K. Sugiyama, E. Ito and K. Seki, *Advanced Materials*, 1999, **11**, 605-+.
21. J. Bisquert and G. Garcia-Belmonte, *Journal of Physical Chemistry Letters*, 2011, **2**, 1950-1964.
22. C. Deibel, T. Strobel and V. Dyakonov, *Advanced Materials*, 2010, **22**, 4097-4111.
23. A. Maurano, R. Hamilton, C. G. Shuttle, A. M. Ballantyne, J. Nelson, B. O'Regan, W. Zhang, I. McCulloch, H. Azimi, M. Morana, C. J. Brabec and J. R. Durrant, *Advanced Materials*, 2010, **22**, 4987-+.
24. C. W. Schlenker and M. E. Thompson, *Chemical Communications*, 2011, **47**, 3702-3716.

Chapter 5
The Origin of the Open-Circuit Voltage in Hybrid PbS Quantum Dot/C60 Bilayer Solar Cells

1. Introduction

Organic solar cells (OSCs) are one of the most promising next-generation photovoltaic technologies and have improved their power conversion efficiency (PCE) significantly in recent years. More recently, inorganic colloidal quantum dots (CQDs) have also shown themselves to be promising candidates for next-generation photovoltaics. Both approaches offer important characteristics for low-cost and high-throughput fabrication such as low-temperature fabrication and compatibility with solution processing. However with each approach there lie limitations. A hybrid organic-inorganic approach is promising as it offers the possibility of maximizing the benefits of each material as well as minimizing the drawbacks and limitations of each respective compound. OSCs, *for e.g.,* have now exceeded power conversion efficiencies of 10% and are edging closer to the production line. However, some limitations still exist, with one being their inability to obtain very high photocurrent due to their intrinsic low exciton diffusion lengths. Furthermore, it is difficult to have efficient organic semiconductors that can extend their absorption far into the NIR, limiting their ability to cover the entire spectrum.

Colloidal quantum dot (CQD) based solar cells however, can extend their absorption further into the NIR with PbS or PbSe nanocrystals and have recently shown high efficiencies exceeding 7%.[1,2] CQDs have several advantages over organic semiconductors in particular their optical properties, with the ability to tune their absorption characteristics simply by changing the nanocrystal size,[3,4] and also posses the capability of multiple exciton generation.[5] Another advantage is that they have higher dielectric constants meaning in comparison to organic semiconductors, allowing spontaneous generation of free charge carriers under light irradiation. Several approaches have already been demonstrated in the literature utilizing quantum dots such as Schottky devices,[6] depleted heterojunctions,[7] quantum dot sensitized solar cells (QDSSC),[8] bulk heterojunction (BHJ) QD:polymer,[9] and bilayer CQD/small molecule solar cells.[10]

Pb-based nanocrystals have shown the best device efficiencies due to the their excellent optical properties in that they posses the characteristic of being panchromatic with the ability to extend their absorption into the infrared through increasing their diameter,[4,11] allowing a larger portion of the solar spectrum to be harvested compared to Cd-based CQDs *for e.g*; this leads to devices with extremely high photocurrents.[2] However, the further one wishes to extend the absorption of the CQDs into the NIR, the lower the band-gap becomes, which in turn affects the open-circuit voltage (V_{OC}).[12] The device architecture can also limit the V_{OC}, *for e.g.*, the maximum achievable V_{OC} for a Schottky or depleted heterojunction device is limited by the work functions of the electrodes. A method to decouple the influence of the contacts on the V_{OC} is to employ a donor-acceptor type-II heterojunction where the V_{OC} is instead determined by the difference in the donor HOMO (valence band) and the acceptor LUMO (conduction band) of the organic (inorganic) semiconductors. The V_{OC} is simply the point at which no-net current flows in a device, where the flux of charge generation is equal to the flux of

charge recombination. PbS CQD devices have also used this heterojunction approach with PbS acting as the donor, and either a metal oxide (ZnO),[13] CQD (Bi_2S_3),[14] or organic (C_{60}),[10] acting as the acceptor. Hybrid inorganic CQD/organic devices are particularly interesting, especially considering the difficulty in designing efficient NIR chromophores that can absorb at wavelengths beyond 800 nm. Using CQDs together with organic semiconductors therefore offers exciting prospects for single junction solar cells with absorption extending much further into the NIR than is possible using a pure organic active layer. Furthermore, this approach also opens the door to tandem solar cells.

Previously we have studied the charge transfer kinetics and non-geminate charge recombination dynamics for a number of QDSSC and QD:polymer solar cells through the use of transient optical and optoelectronic techniques,[15-18] and we now extend the analysis to bilayer PbS quantum dot/C_{60} devices to quantify the rate of non-geminate recombination with respect to the charge density in the device, and to use this information to understand the role non-geminate recombination has on the V_{OC} in these devices. An added advantage of choosing a bilayer architecture is that we can control the interface rather than have a disordered BHJ morphology that is common for QD:polymer devices. We employ transient optoelectronic techniques, namely charge extraction (CE) and transient photovoltage (TPV), to quantify the charge density and non-geminate recombination rate, of PbS/C_{60} planar heterojunction solar cells under working conditions (device architecture and typical energy levels of the materials are shown in Figure 1). Correlating the charges present in the device with the charge carrier lifetime allows us to accurately reconstruct the experimental current-voltage curve using the model introduced for organic solar cells,[19] which to the best of our knowledge is the first time it has been reported for hybrid organic-inorganic solar cells based on CQDs.

2. Experimental

PbS CQDs were prepared following a slightly modified procedure described by Sargent *et al*.[20] 35 ml of 1-octadecene (ODA) was heated at 80 °C under vacuum for 9 hours. Following this, 0.45 g of PbO, 1.3 ml of oleic acid and 3 ml of distilled ODE was placed under vacuum for 16 hours at 95 °C. The colour of the solution changed from yellow to transparent and subsequently the temperature was raised to 120 °C and a degassed solution of 210 μl of bis(trimethylsilyl)sulphide (TMS) in 10 ml of ODE was steadily injected. The solution was then allowed to cool to room temperature. The solution was precipitated with acetone and re-dispersed in toluene to remove the reaction side-products. The dried product was then dispersed in 3 ml of toluene and 1 ml of distilled oleyamine was added. This solution was stored in a glove-bod under a N_2 atmosphere for two days without disturbing. The CQD solution was then precipitated with methanol and re-dispersed in toluene three times. Finally, the CQDs were dispersed in anhydrous octane at a concentration of 10 mg/ml.

Devices were fabricated with the following structure: ITO/PbS(15 nm)/C60(40 nm)/BCP(8 nm)/Al(100 nm). First ITO (Psiotech Ltd., 5 Ω/square) substrates were cleaned by three sonication cycles, the first in acetone followed by two cycles in isopropanol, each cycle lasting 15 min. Following this the substrates were subjected to 20 Uv/O_3 treatment. PbS CQD films were grown using a layer-by-layer spin-coating procedure with 10 mg/ml PbS CQD solution that included a ligand exchange process after depositing each layer, whereby the bulky oleyamine ligands were replaced by 3-mercaptopropionic acid (MPA), by spin coating a solution of MPA dissolved in methanol (10% v/v). After each ligand exchange step, excess ligands were washed away using first methanol followed by octane. Finally the substrate was briefly annealed at 470 °C through the use of a heat gun, with the next PbS layer then ready to be deposited. Each layer corresponded to

approx. 2 monolayers (5 nm), and 3 layers were grown producing films of 15 nm as measured by transmission electron microscopy. Following this, the films were transferred to a high vacuum chamber where C60 (40 nm), BCP (8 nm) and Al (100 nm) were deposited by thermal evaporation at a base pressure not exceeding 1 x 10^{-6} mbar.

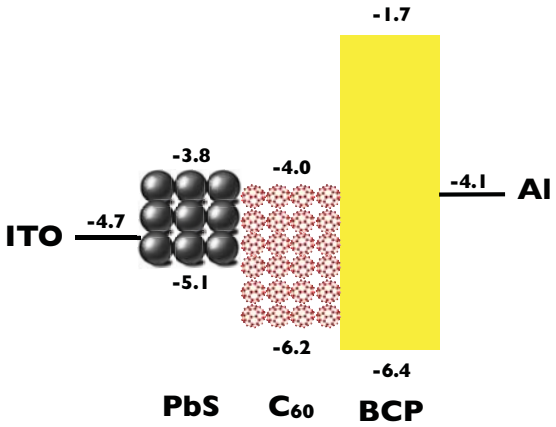

Figure 1 Energy levels of the materials employed with the device architecture ITO/PbS/C60/BCP/Al

3. Results and Disucssion

The current/voltage (*J-V*) curve of the device under various light intensities measured using a calibrated solar simulator (AM 1.5 G, 100 mW/cm^2) is shown in Figure 2. The device shows a short circuit current, J_{SC}, of 8.26 mA/cm^2, a V_{OC} of 0.38 V and FF of 0.64, corresponding to a power conversion efficiency, η = 2.04% at 1 Sun.

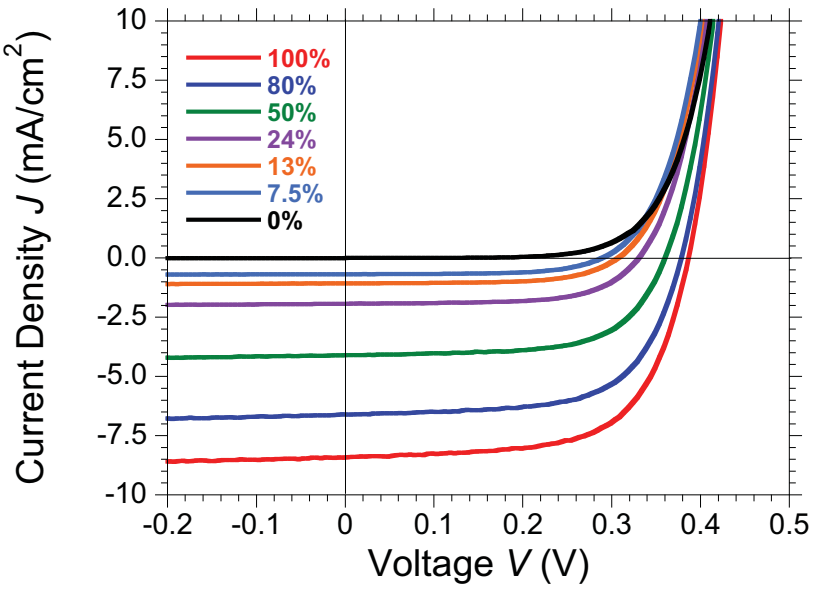

Figure 2 Current/voltage curves for devices measured under standard AM 1.5 G conditions (100 mW/cm^2), where the intensity of irradiance was fixed using neutral density filters. The legend shows the % of irradiance with respect to 1 Sun illumination, calculated using a calibrated silicon diode.

Figure 3(a) shows the relationship between J_{SC} and light intensity (LI), which has a power law behavior with the relationship $P \propto LI^{\alpha}$, with $\alpha = 1.01$, signifying that non-geminate recombination at short circuit is negligible and also that there is no significant space charge buildup.[21,22] The correlation between V_{OC} with LI is also shown in Figure 3(b), showing a linear increase of V_{OC} with the logarithmic of LI. The slope of the curve in an ideal diode would correspond to the thermal voltage k_BT, the deviation from ideal behavior is termed the ideality factor and is calculated

from the following equation:

$$n_{id} = \frac{q}{k_B T} \frac{dV_{OC}}{dln(LI)} \qquad \textbf{(1)}$$

where, q is the elementary charge, k_BT is the thermal energy, with n_{id} = 1.47. Generally, the ideality factor ranges from 1 to 2 and it provides information on the origin of the charge recombination that occurs in a device. An ideality factor increasing from 1 indicates the presence of trap states, with higher values corresponding to the presence of deeper and more abundant traps. The ideality factor also gives an indication of what process is determining the charge carrier recombination dynamics, n_{id} = 1 signifying bimolecular recombination and n_{id} = 2 indicating Shockley-Read-Hall (SRH) recombination.[23] [24] Therefore, the rather high value obtained for PbS/C_{60} suggests that there is a significant concentration of trap states, which will affect the non-geminate recombination dynamics. In related studies, trap states (mid-gap states) have been shown to affect non-geminate recombination and furthermore the V_{OC} in PbS/methano-fullerene bilayer, although no relationship with charge carrier density was shown.[25]

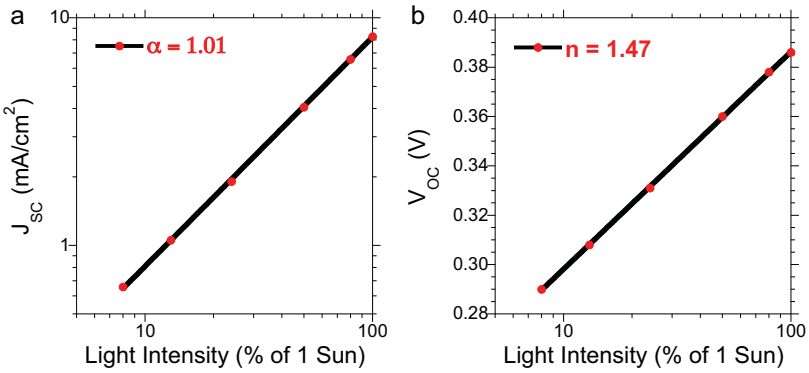

Figure 3 J_{SC} (a) and V_{OC} (b) plotted versus light intensity. In (a) α corresponds to the power law fit where $P \propto LI^{\alpha}$ and in (b) n corresponds to the ideality factor obtained from Equation (1).

To quantify the charge present in the device under illumination, we employed the charge extraction technique, as used in previous publications by our group as well as others.[26,27] For this experiment, the device is held at open-circuit by applying either a light or electrical bias through a set of LEDs or external power source until steady state is reached (1-2 s) and then switched from open circuit to short circuit while simultaneously switching off the LEDs. Sweeping the bias from values higher than V_{OC} at 1 sun (V_{OC}=0.38V at 1 sun in this case) to dark conditions allows a good estimate of the charge present in the device under working conditions to be obtained. Figure 4 shows the charge density plotted *versus* light bias, which increases linearly to begin with before becoming exponential at higher applied bias (red curve). The geometrical capacitance was calculated by carrying out CE measurements in the dark and under negative bias, as reported before,[21] and was found to be 83 nF/cm^2. The linear dependence of charge *versus* bias at low light intensity is similar to the geometrical charges signifying that there is very little chemical charge built up in the active layer at low light bias, with the charges mostly present at the electrodes. At increased forward bias the charges in the device begin to increase exponentially to values higher than the corresponding capacitive charges. The charges can therefore be related to excess charge carriers generated in the photoactive region. This exponential increase has been previously attributed to the splitting of the quasi-Fermi levels in donor and acceptor molecules in organic bulk-heterojunction solar cells.[19] We can fit the data in Figure 2 according to the following equation that correlates the charges in the device with the V_{OC}:

$$n = n_0 e^{\gamma V_{OC}} \qquad \textbf{(2)}$$

where, n_0 ~ 2.77 x 10^{15} carriers/cm^3 and γ ~ 7.12 V^{-1}, if we consider the total charge in the device. The parameter γ provides an estimate of the tail of the density

of states (DOS), and is considerably lower than an ideal semiconductor ($\gamma < 19$ V $^{-1}$ for 2kT). This points towards the system having a high density of trap states and is consistent with the ideality factor measured from Figure 3b.[28] Our observations here of a low number of carriers and a low γ is similar to previous charge extraction measurements of planar heterojunction solar cells,[21,27,29] and is due to the thin nature of the films and high energetic disorder.[19,30]

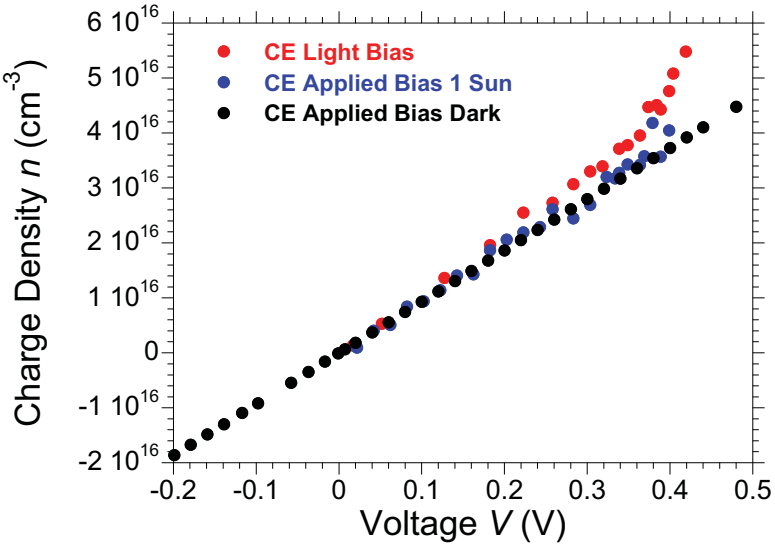

Figure 4 Charge extraction data for the same device measured under light bias and applied bias (dark and 1 Sun illumination). Charge losses during extraction are accounted for.

TPV measurements provide a direct measurement of the charge carrier lifetimes in the device. The TPV experiment consists of holding the device at open-circuit under steady state conditions by applying a light bias *via* a ring of LEDs, akin to CE. Next a small perturbation is applied to the device by, in this case, a laser. The small perturbation (5-10 mV) generates extra charges in the device that cannot be extracted, as the system is being held at open-circuit, forcing the charges to recombine. An added advantage of this technique is that the small excess charge

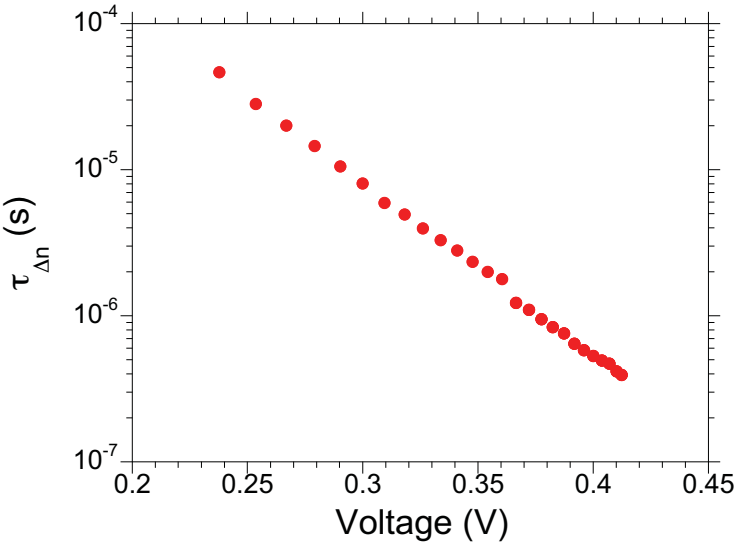

Figure 5 Small perturbation lifetime *versus* lifetime obtained from TPV measurements

generated decay mono-exponentially making it easy to calculate the excess charge carrier lifetime:

$$\Delta n = \Delta n_0 e^{-t/\tau_{\Delta n}} \quad \textbf{(3)}$$

where, t is the time, Δn_0 is the photogenerated charge at t = 0 and $\tau_{\Delta n}$ is the lifetime of the transient. For each point on the current-voltage curve we can obtain a specific lifetime. Plotting the measured small perturbation lifetimes, $\tau_{\Delta n}$ as a function of V_{OC} is shown in Figure 5, which shows a non-linear relationship between charge carrier lifetime and applied bias. The charge carriers in fact decay exponentially with bias with the function:

$$\tau_{\Delta n} = \tau_{\Delta n_0} e^{-\beta V_{OC}} \quad \textbf{(4)}$$

where, $\tau_{\Delta n_0}$ ~ 0.012 s, and β, the decay constant, is ~ 24.94 V^{-1}. This exponential decay is consistent with the behavior of organic solar cells. At 1 Sun conditions $\tau_{\Delta n}$ is < 1 μs; these lifetimes are very short in comparison to higher V_{OC} OSCs, which already suggests the reason for the low device V_{OC}.

Having now obtained the relationship between $\tau_{\Delta n}$ and applied bias as well as the behavior of n with applied bias, we can correlate $\tau_{\Delta n}$ with n by interpolating the applied bias with the exponential fit obtained from CE under light bias. Figure 6 shows the lifetime *versus* charge density, which displays a power law behavior :

$$\tau_{\Delta n} \propto n^{-\lambda} \qquad \textbf{(5)}$$

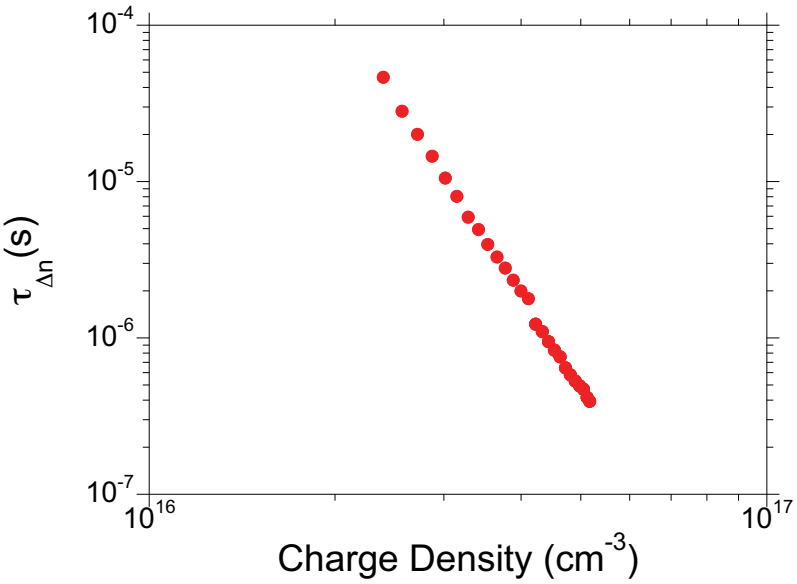

Figure 6 Small perturbation *versus* charge density, using the exponential relationship between charge density and bias obtained from CE under light bias.

The power law, λ, can also be calculated simply by considering the exponential decay of $\tau_{\Delta n}$ *versus* bias (β) and the exponential growth of charge density *versus* bias (γ): β/γ = λ. This thus provides us with a relationship between charge density the small perturbation charge carrier lifetime, as opposed to the total charge carrier lifetime, τ_n. Correcting for this is rather simple and has been shown to apply to both OSCs and dye-sensitized solar cells, with the total charge carrier lifetime:

$$\tau_n = \tau_{\Delta n}(\lambda + 1) \qquad \textbf{(6)}$$

It has been shown for organic solar cells that the relationship between *n* and τ_n gives the empirical reaction order, Φ (Φ = λ+1) of the free charge carriers, with some values suggesting bimolecular recombination.[19,31,32] For the measured PbS/C_{60} devices here, we obtain an empirical reaction order of 5.8. This is simply too high to be related to bimolecular recombination, but is not uncommon for such a thin active layer. For OSCs, many devices have shown high reaction orders too and in particular when the active layer thickness is very thin.[33,34] One of the reasons for the high values of Φ is due to a large gradient in carrier concentration,[33] due to energetic disorder, surface recombination and trap-assisted recombination. What is important here however is that the relationship still gives us accurate information on the rate at which the charges are recombining within the device, even though the origin of the recombination is not clear, and is most likely a convolution of different events occurring at the PbS/C_{60} interface, within each respective layer, or at the contacts.

Having determined the correlation between charge density and charge carrier lifetime in the active layer, we attempt to reconstruct the *J-V* behavior of the hybrid PbS/C_{60} device under 1 Sun conditions. Durrant and coworkers have shown that using a simple model that takes into account the flux of photo-generated charges

(J_{gen}) and the flux of non-geminate recombination (J_{loss}) that it is possible to reconstruct the *J-V* curve accurately,[34] using the relationship:

$$J = J_{gen} + J_{loss} \quad \textbf{(7)}$$

$$J_{loss} = \frac{edn}{\tau_n} \quad \textbf{(8)}$$

where d is the thickness of the active layer, n is the charge density and τ_n the charges lifetime. In this approximation it is assumed that the loss processes are simply due to non-geminate recombination and are negligible close to short-circuit. Increasing the bias closer to V_{OC}, the non-geminate recombination begins to increase significantly and at V_{OC} the flux of non-geminate recombination equals that of J_{gen}, Carrying out CE under 1 Sun illumination conditions (Figure 4) and applied electrical bias allows n to be calculated each point across the *J-V* curve. To reconstruct the *J-V* curve to the experimental one shown at 1 Sun in Figure 2, we allow $J_{gen} = J_{SC}$, and calculate J_{loss} using Equation 8. An additional correction to account for the small photoshunt is applied too. This correction does not affect the calculated V_{OC} and any non-geminate recombination causing it can be ruled out based on the relationship between J_{SC} and LI having a power law = 1.01 (see Figure 3a). The voltage in cell is corrected for considering: $V_{cell} = V_{appl} - IR_s$, where $R_s$is the series resistance. The experimental and reconstructed *J-V* curves are shown in Figure 7 and are in good agreement, with the reconstructed V_{OC} = 0.383 mV exactly matching the experimental V_{OC} of 0.383 mV. In other similar devices that we measured there was a small fluctuation between the calculated VOC and the experimental VOC, consistent with the trend observed for a range of different organic solar cells.[34] The fact that the 1 Sun *J-V* behavior can be reproduced using

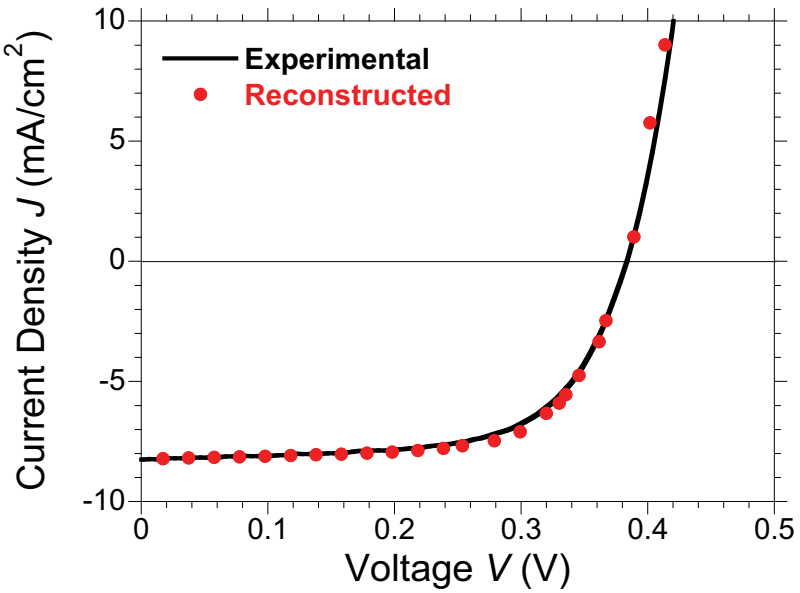

Figure 7 Comparison between the reconstructed *JV* curve using Equation 7 and the experimental *JV* curve as presented in Figure 2.

this simple relationship between generation and recombination signifies that the origin the V_{OC} in these devices is field-independent and is controlled by non-geminate recombination. Knowing that non-geminate recombination is the key loss mechanism affecting the V_{OC} thus provides a route towards optimizing device performance further. Reducing the concentration of trap states is perhaps the most significant step with regards to optimization. CQDs in particular tend to have a high distribution of mid-gap states that trap charges and thus push the ideality factor higher; reducing these trap states will see more ideal diode behavior, longer charge carrier lifetime and thus higher V_{OC}. Recently, CQD solar cells have seen improvements in V_{OC} with either a reduction in trap states or through doping the transition metal acceptor. It will be interesting to see if the same procedure to reconstruct the *J-V* curve can be be applied to other CQD-basd solar cells such as depleted heterojunction devices, which have different working mechanism but like

organic semiconductors tend to have a large degree of energetic disorder, unlike their bulk properties.

4. Conclusions

In summary, we have studied the optoelectronic performance of PbS/C_{60} devices through both steady state *J-V* characterization and transient optoelectronic measurements. From the data obtained we see that the open-circuit voltage increases linearly with the logarithm of LI, evidence for the increased splitting of quasi-Fermi levels with LI and correlated their relationship to obtain an ideality factor of 1.47, meaning that there is quite a large density of traps that affect non-geminate recombination. Furthermore, based on the relationship between J_{SC} and LI, non-geminate recombination is negligible at short circuit, suggesting that the origin of the photoshunt is a field dependent generation process. The charge carrier lifetime in the films is short, on the order of 1 x 10^{-6} s, with a steep decay order of 24.94, meaning charge carrier lifetime decreases rapidly with increasing bias. The charge density in the active layer is very low, as seen for similar organic bilayer devices, with most of the charges residing at the electrodes under low bias conditions, and increasing exponentially close to V_{OC}. Using the relationship between J_{gen} and J_{loss} we could accurately reconstruct the *J-V* curve proving that V_{OC} here is field independent and can be improved by reducing the rate of non-geminate recombination. More important, our results clearly point out that, increasing the lifetime of the charge carriers through improving the selective contacts and reducing the trap states present at the PbS/C_{60} interface will lead to higher V_{OC} and thus improved efficiencies. Thus, the biggest room for improvement lies with the PbS CQD synthesis and choice of ligands/passivation layer.

5. References

1. I. J. Kramer and E. H. Sargent, *ACS Nano*, 2011, **5**, 8506-8514.
2. A. H. Ip, S. M. Thon, S. Hoogland, O. Voznyy, D. Zhitomirsky, R. Debnath, L. Levina, L. R. Rollny, G. H. Carey, A. Fischer, K. W. Kemp, I. J. Kramer, Z. Ning, A. J. Labelle, K. W. Chou, A. Amassian and E. H. Sargent, *Nature Nanotechnology*, 2012, **7**, 577-582.
3. A. P. Alivisatos, *Science*, 1996, **271**, 933-937.
4. I. Moreels, K. Lambert, D. Smeets, D. De Muynck, T. Nollet, J. C. Martins, F. Vanhaecke, A. Vantomme, C. Delerue, G. Allan and Z. Hens, *ACS Nano*, 2009, **3**, 3023-3030.
5. O. E. Semonin, J. M. Luther, S. Choi, H.-Y. Chen, J. Gao, A. J. Nozik and M. C. Beard, *Science*, 2011, **334**, 1530-1533.
6. J. Tang, X. Wang, L. Brzozowski, D. A. R. Barkhouse, R. Debnath, L. Levina and E. H. Sargent, *Advanced Materials*, 2010, **22**, 1398-1402.
7. A. G. Pattantyus-Abraham, I. J. Kramer, A. R. Barkhouse, X. Wang, G. Konstantatos, R. Debnath, L. Levina, I. Raabe, M. K. Nazeeruddin, M. Graetzel and E. H. Sargent, *ACS Nano*, 2010, **4**, 3374-3380.
8. P. K. Santra, P. V. Nair, K. G. Thomas and P. V. Kamat, *Journal of Physical Chemistry Letters*, 2013, **4**, 722-729.
9. Y. Zhou, M. Eck, C. Veit, B. Zimmermann, F. Rauscher, P. Niyamakom, S. Yilmaz, I. Dumsch, S. Allard, U. Scherf and M. Krüger, *Solar Energy Materials and Solar Cells*, 2011, **95**, 1232-1237.
10. E. J. D. Klem, C. W. Gregory, G. B. Cunningham, S. Hall, D. S. Temple and J. S. Lewis, *Applied Physics Letters*, 2012, **100**, 173109.
11. J. Tang and E. H. Sargent, *Advanced Materials*, 2011, **23**, 12-29.
12. K. Szendrei, W. Gomulya, M. Yarema, W. Heiss and M. A. Loi, *Applied Physics Letters*, 2010, **97**, 203501.
13. J. J. Choi, Y.-F. Lim, M. E. B. Santiago-Berrios, M. Oh, B.-R. Hyun, L. Sun, A. C. Bartnik, A. Goedhart, G. G. Malliaras, H. c. D. Abruña, F. W. Wise and T. Hanrath, *Nano Letters*, 2009, **9**, 3749-3755.

14. A. K. Rath, M. Bernechea, L. Martinez, F. Pelayo Garcia de Arquer, J. Osmond and G. Konstantatos, *Nature Photonics*, 2012, **6**, 529-534.
15. J. Albero, Y. Zhou, M. Eck, F. Rauscher, P. Niyamakom, I. Dumsch, S. Allard, U. Scherf, M. Krueger and E. Palomares, *Chemical Science*, 2011, **2**, 2396-2401.
16. E. Martinez-Ferrero, I. Mora Sero, J. Albero, S. Gimenez, J. Bisquert and E. Palomares, *Physical Chemistry Chemical Physics*, 2010, **12**, 2819-2821.
17. M. Shalom, J. Albero, Z. Tachan, E. Martinez-Ferrero, A. Zaban and E. Palomares, *Journal of Physical Chemistry Letters*, 2010, **1**, 1134-1138.
18. T. Zewdu, J. N. Clifford, J. P. Hernandez and E. Palomares, *Energy & Environmental Science*, 2011, **4**, 4633-4638.
19. C. G. Shuttle, R. Hamilton, B. C. O'Regan, J. Nelson and J. R. Durrant, *Proceedings of the National Academy of Sciences*, 2010, **107**, 16448-16452.
20. J. Tang, L. Brzozowski, D. A. R. Barkhouse, X. Wang, R. Debnath, R. Wolowiec, E. Palmiano, L. Levina, A. G. Pattantyus-Abraham, D. Jamakosmanovic and E. H. Sargent, *ACS Nano*, 2010, **4**, 869-878.
21. D. Credgington, Y. Kim, J. Labram, T. D. Anthopoulos and J. R. Durrant, *The Journal of Physical Chemistry Letters*, 2011, **2**, 2759-2763.
22. L. J. A. Koster, V. D. Mihailetchi, H. Xie and P. W. M. Blom, *Applied Physics Letters*, 2005, **87**, 203502.
23. C. v. Berkel, M. J. Powell, A. R. Franklin and I. D. French, *Journal of Applied Physics*, 1993, **73**, 5264-5268.
24. K. Szendrei, W. Gomulya, M. Yarema, W. Heiss and M. A. Loi, *Applied Physics Letters*, 2010, **97**, 203501-203505.
25. N. Zhao, T. P. Osedach, L.-Y. Chang, S. M. Geyer, D. Wanger, M. T. Binda, A. C. Arango, M. G. Bawendi and V. Bulovic, *ACS Nano*, 2010, **4**, 3743-3752.
26. G. F. A. Dibb, T. Kirchartz, D. Credgington, J. R. Durrant and J. Nelson, *The Journal of Physical Chemistry Letters*, 2011, **2**, 2407-2411.
27. A. Sánchez-Díaz, L. Burtone, M. Riede and E. Palomares, *The Journal of Physical Chemistry C*, 2012, **116**, 16384-16390.
28. A. Maurano, C. G. Shuttle, R. Hamilton, A. M. Ballantyne, J. Nelson, W. Zhang, M. Heeney and J. R. Durrant, *The Journal of Physical Chemistry C*, 2011, **115**, 5947-5957.

29. A. Foertig, A. Wagenpfahl, T. Gerbich, D. Cheyns, V. Dyakonov and C. Deibel, *Advanced Energy Materials*, 2012, **2**, 1483-1489.
30. J. Bisquert and G. Garcia-Belmonte, *The Journal of Physical Chemistry Letters*, 2011, **2**, 1950-1964.
31. A. Maurano, R. Hamilton, C. G. Shuttle, A. M. Ballantyne, J. Nelson, B. O'Regan, W. Zhang, I. McCulloch, H. Azimi, M. Morana, C. J. Brabec and J. R. Durrant, *Advanced Materials*, 2010, **22**, 4987-4992.
32. C. G. Shuttle, B. O'Regan, A. M. Ballantyne, J. Nelson, D. D. C. Bradley and J. R. Durrant, *Physical Review B*, 2008, **78**, 113201.
33. T. Kirchartz and J. Nelson, *Physical Review B*, 2012, **86**, 165201.
34. D. Credgington and J. R. Durrant, *The Journal of Physical Chemistry Letters*, 2012, **3**, 1465-1478.

Chapter 6
Towards Low-Temperature Preparation of Hybrid Light-Emitting Diodes

1. Introduction

Organic light-emitting diodes (OLEDs) are the leading contenders in next generation lighting and have already entered the market in devices such as mobile phones and media players since they offer several benefits over current technology such as low material consumption and high efficiency.[1] However, OLEDs use low work function electrodes that are susceptible to degradation from both air and water,[2] leaving them reliant on a costly encapsulation process. Recently hybrid organic–inorganic light-emitting diodes (HyLEDs) have been reported as a low-cost alternative, offering a route to encapsulation free devices.[3] HyLEDs use an inverted architecture, relying on metal oxide (MO) transport layers, which allow the use of high work function, air-stable top electrodes. The MO layers are the key feature of these devices as they increase the stability under ambient conditions. The general architecture of a HyLED consists of an emissive conjugated polymer layer sandwiched between an electron transport layer, ETL, (i.e. TiO_2, ZnO, ZrO_2) and a hole transport layer, HTL (MoO_3) with indium-doped tin oxide (ITO) serving as the bottom electrode and Au as the top electrode (Figure 1).[4,5] The versatility of the device structure has allowed the use of different conjugated light-emitting polymers

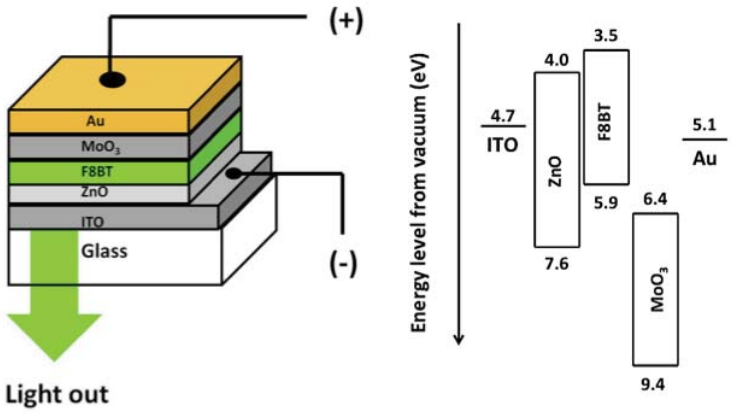

Figure 1 Device architecture (left) and respective energy level diagram (right) for the materials investigated.

(LEPs), typically the green emitting poly(9,9-dioctylfluorene-co-benzothiadiazole) (F8BT), as well as different fluorenes (i.e. PFO, Red-F, or the Lumation series), the poly(phenylenevinylene) derivative Super Yellow and even host–guest blends to obtain white light devices.[5-7] Considering that the materials used to fabricate HyLEDs are all solution processable, a low-cost, high-speed and large-scale fabrication route can be envisioned, without the need for a costly encapsulation step. With regards to the solution processing of the MO layer, advantages include speed, cost and the ability to chemically tune the films' properties with respect to solid source routes such as rf-magnetron sputtering, pulsed laser deposition, chemical vapour deposition, and thermal evaporation, which require high energy and vacuum conditions. For the preparation of MOs several solution processable methods are possible such as dip-coating and spin-coating that can produce quite homogenous films but are not scalable to industry and are severely limited by high material loss. They are, however, very useful techniques for prototyping. One favourable method for depositing MOs is by spray pyrolysis deposition (SPD), which uses a metal salt precursor solution deposited on a heated substrate and is suitable to large-scale processing.

However, SPD may be limited in one respect, the preparation of MO thin films by this method generally requires high T_s (400–500 °C) with several studies reporting that lower T_s results in poorer film quality.[8,9] However, these studies usually test the films in isolation without considering their performance in a functioning device. Although optimum conditions may lead to optimum performances of devices we must consider the other implications imposed by using high temperatures. For example, ITO is known to lower its conductivity through heating.[10] More importantly high temperatures are not favoured in industrial fabrication, especially with roll-to-roll (R2R) methods where substrates must be heated and cooled. Here, we test and compare the performance of simple HyLED architectures fabricated using a ZnO ETL prepared at substrate temperatures between 150 °C and 450 °C by spray pyrolysis deposition, with ZnO being chosen since it is a non-toxic semiconductor that shows high mobility, environmental stability and high transparency.[11] Working devices were characterised by recording luminance current–voltage values simultaneously. The results of the optoelectronic characterisation were then compared and correlated with structural characterisation of the ZnO films by X-ray Diffraction (XRD) and Atomic Force Microscopy (AFM). This combination of experimental data thus allowed the relationship between processing conditions, MO quality, and device performance to be derived.

2. Experimental

Thin films of ZnO were deposited by air blast spray pyrolysis deposition from a precursor solution of zinc acetate dihydrate in methanol (80 g L^{-1}, materials bought at Alfa Aesar and SDS, respectively) onto pre-patterned ITO glass substrates (4 Ω/square, obtained from Ikerlan) for device fabrication or on Si wafers for structural characterisation. The precursor solution was sprayed onto the conductive ITO substrate at different temperatures ranging from 150 to 450 °C using compressed air as the carrier gas. Subsequently the films were annealed in a

furnace for 20 min at the same temperature applied during deposition. The emissive F8BT layer (obtained from American Dye Source) was spin coated from a chlorobenzene solution (10 mg mL^{-1}) at a rate of 2000 rpm for 30 s. The polymer was annealed at 85 °C for 20 min in a nitrogen rich atmosphere to improve F8BT morphology. Finally, the samples were transferred to a thermal evaporation chamber where the MoO_3 (10 nm, obtained at Sigma Aldrich) and Au (50 nm, Kurt Lesker) layers were deposited under high vacuum (1 $x10^{-6}$ mbar).

Current density and luminance versus applied voltage were recorded using a Keithley 2400 combined with a Konica Minolta LS100 luminance meter. The instruments were controlled and the data captured using in- house software. Roughness Mean Square (RMS) values were measured by Atomic Force Microscopy (AFM), performed on tapping mode on a Molecular Imaging model Pico SPM II (Pico +). X-ray diffraction was done on ZnO films deposited on Si (001) substrates at different temperatures using a Bruker-AXS D8-Discover diffractometer equipped with parallel incident beam (Göbel mirror), vertical θ-θ goniometer, XYZ motorized stage and with a GADDS (General Area Diffraction System. The X-ray diffractometer was operated at 40 kV and 40 mA to generate Cukα radiation. The GADDS detector was 30x30 cm with a 1024x1024 pixel sensor. We collected one frame (2D XRD pattern) covering 20-50º 2θ in grazing incidence mode (ω: 1º, 2θ: 34º) at a distance of 15cm from the sample to the detector. The exposition time was 300s per frame and it was chi-integrated to generate the conventional 2θ vs. intensity diffractogram.

3. Results and Discussion

First we consider the luminance vs. applied bias, Figure 2a, for devices prepared using ZnO ETL processed at T_s from 150 to 450 °C. For devices prepared between 250 °C and 450 °C, almost identical luminance turn-on voltages are observed, 2 V,

while the voltage dependence differs slightly. Interestingly the highest luminance values of 12000 cd m^{-2} are found for devices processed at 250 °C. By increasing the substrate temperature to 350 °C a decrease in luminance to 9000 cd m^{-2} is observed, while a further increase in the substrate temperature by 100 °C again leads to a decrease in luminance to 7000 cd A^{-1}. Furthermore, the maximum luminance value is attained at different applied bias, increasing 0.5 V with every increase of 100 °C (Table 1). On the other hand, lower luminance values are obtained for HyLEDs when ZnO is prepared at 150 °C, together with a higher turn-on voltage, 2.5 V. Differences in luminance may be explained by the higher current density observed for T_s 250 °C and 350 °C, one order of magnitude higher than T_s 450 °C (Figure 2b). As reported previously,[12] the operational mechanism of the devices is hole-dominated. Holes are injected into the LEP through the Au and MoO_3 layers and transported towards the negative biased electrode. Due to the difference between the LEP-HOMO and the ZnO-Valence Band energy values, the holes accumulate at the ETL/LEP interface creating a built-in electric field. This field reduces the barrier for electron injection into the LEP, where charge recombination will occur. However, the current leakage through the metal oxides provides the origin of the high current density values obtained.[6] In this sense, the T_s influences the values of the current density, probably due to the better crystallinity of the film (*vide infra*). Current efficiency values data, which relates the luminance to current density are shown in Figure 3. The large difference in current density contributes largely to the resulting current efficiencies with 450 °C being significantly better. However, if we consider the values of devices prepared at 350 °C and more importantly 250 °C the values are still respectable and compare well with previous work on HyLEDs with identical architecture (Table 1). The same trend is also evident for the luminous efficacy with devices using ZnO films prepared at 450 °C reaching 1 lm W^{-1} (see Table 1).

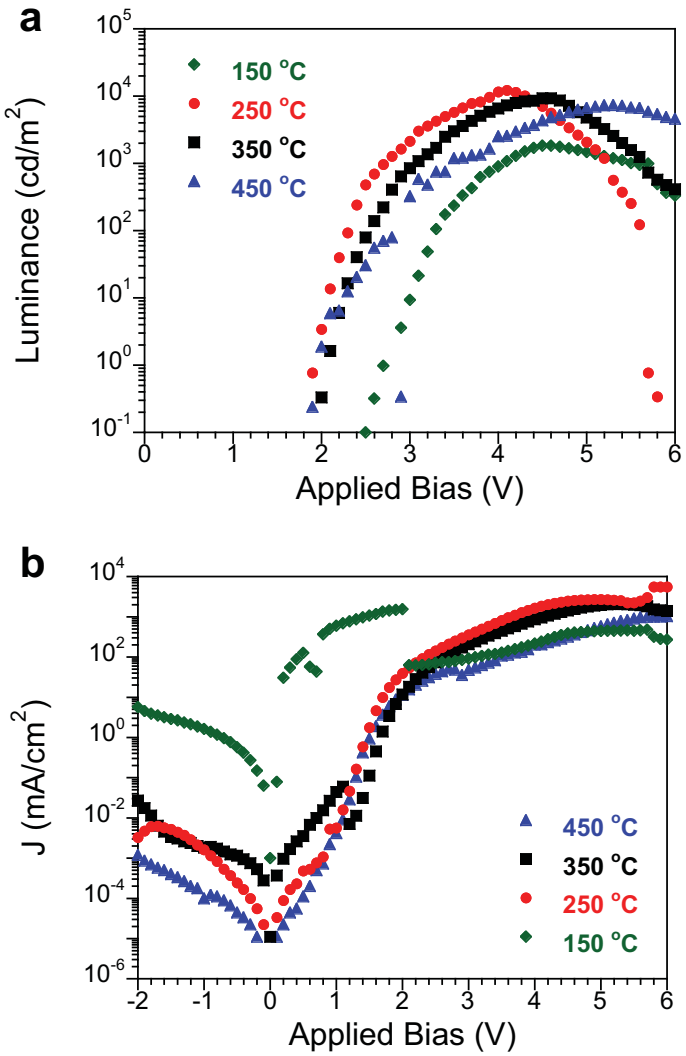

Figure 2 Luminance (a) and current density (b) *versus* applied bias for HyLEDs with the ZnO ETL prepared at various substrate temperatures.

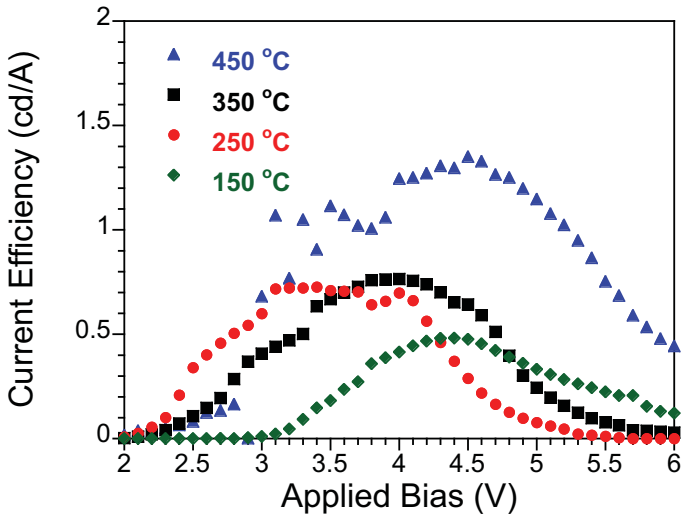

Figure 3 Current efficiency versus applied bias for HyLEDs prepared with ZnO ETL prepared at various substrate temperatures.

Table 1 Device characteristic of the samples containing ZnO films prepared at differed T_s and their morphological parameters

Ts (°C)	Maximum luminance (cd m^{-2}) (at voltage, V)	Maximum current efficiency (cd A^{-1}) (at luminance, cd m^{-2})	Maximum luminous efficicacy (lm W^{-1}) (at luminance, cd^{-2})	RMS (nm)
150	1835 (4.6)	0.48 (1708)	0.35 (1511)	0.14
250	12 260 (4.1)	0.73 (5014)	0.72 (3028)	0.31
350	9259 (4.6)	0.76 (6572)	0.63 (5116)	0.74
450	7384 (5.3)	1.35 (4343)	0.98 (2533)	0.77

Data on the crystallinity and morphology obtained from XRD and AFM shed light on the above observations, especially with respect to the current density values. XRD measurements (Figure 4) show that T_s determines the orientation of the crystal growth in the ZnO films as well as determining the crystallite size; increasing with increasing temperature (see Table 2). In each case, the films are polycrystalline, however, the ratio of crystal orientation varies at each temperature, in agreement with previous findings.[13] At 250 °C the ZnO shows a preferred orientation (100) with high contributions from both (002) and (101) orientations.

As the temperature film structure that shows a preferred orientation at (002) while the (100) and (101) peaks are almost diminished and the secondary peak for (102) is still present. This change to a preferred (002) orientation may explain the lower current density observed for devices prepared at T_s 450 °C. Moreover, comparing the crystal orientation in the ZnO films and current density recorded for the devices where ZnO was prepared at 250 and 350 °C there is very little difference in both cases. Please note the shift observed between the expected and experimental position of the peaks is due to the low thickness of the films and the characteristics of the technique. In fact, previous observations in ZnO-containing thin-film field-effect transistors (TFTs) demonstrated that the most favourable crystal orientation is the (002) c-axis when it is perpendicular to the substrate.[14] When this occurred, TFTs showed higher mobilities. On the other hand, experiments with ambipolar organic FETs containing ZnO deposited at different temperatures showed that the quality of the ZnO as electron injecting layer was determined by the surface roughness of the MO which depends on the deposition temperature.[8] All the ZnO films used in this work present Roughness Mean Square (RMS) values, measured by AFM, lower than 1 nm (Table 1). The RMS increases with the deposition temperature, although we cannot clearly correlate this increase with the device performance, probably due to the fact that all the films are quite flat. Focusing on the XRD data, ZnO films prepared at 250 °C and 350 °C both contain multiple orientations and give rise to devices with similar efficiency values. Films prepared at 450 °C show a preferred (002) orientation giving the highest efficiency values and lower current densities.

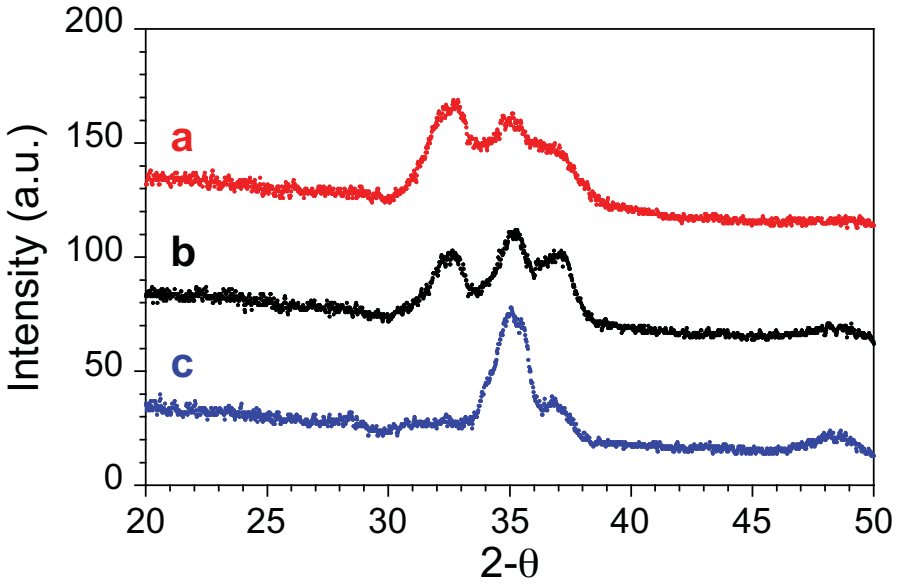

Figure 4 XRD diffractogram of ZnO films on Si prepared at (a) 250 °C, (b) 350 °C and (c) 450 °C. Red lines indicate the position of the diffraction peaks of ZnO.

Table 2 Crystallite size derived from XRD measurements

Substrate temperature (°C)	Orientation	Crystallite size (nm)
450	(100)	-
450	(002)	6.4
450	(101)	11.5
450	(102)	5.5
350	(100)	5.6
350	(002)	6.0
350	(101)	7.3
350	(102)	3.9
250	(100)	5.2
250	(002)	4.8
250	(101)	4.8
250	(102)	-

Therefore, we can conclude that T_s does influence both material and electronic properties of ZnO films in HyLEDs. Interestingly the device performances are quite efficient even as low as 250 °C. This is an important finding for fabrication as a decrease of 200 °C offers much reduced costs as less heating is required, reducing heating and cooling times thus offering faster processing times. It must be noted that the results presented here are of single devices, which reflect the average performance of HyLEDs prepared at each respective T_s. But it is worthy to note that devices prepared at 450 °C have achieved record efficiencies of 3.3 cd A^{-1} and2.6 l m W^{-1}, although giving lower values of luminance and current density. In order to test the influence of the ETL on the overall performance of the device, we prepared devices without ZnO, i.e. ITO/F8BT/MoO3/Au. The results (Figure 5) show that the current density is an order of magnitude higher without ZnO, has a turn-on voltage 1 V higher and significantly lower luminance. These parameters lead to a very low current efficiency of 0.08 cd A^{-1} and demonstrate the need of an ETL/HBL to lower both the turn-on voltage and current densities. In this sense, similar observations have been made when comparing conventional OLED (structure: ITO/PEDOT:PSS/F8BT/Ca/Al) to HyLEDs constructed with the same LEP: ITO/ZnO/Cs2CO3/F8BT/MoO3/Au.[12,15] Although in both cases the current is limited by the better injecting electrode, the conventional OLED showed higher operating voltages and lower luminance values due to the better built-in field obtained at the ZnO/F8BT interface than at the F8BT/Ca/Al.

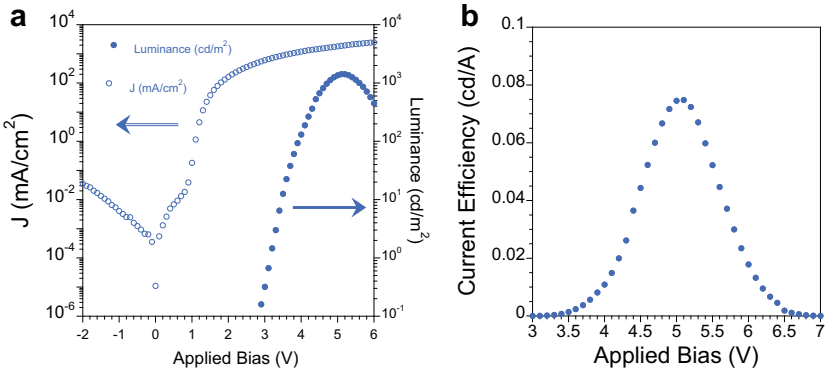

Figure 5 Current density (a) and current efficiency (b) *versus* applied bias for the devices prepared without a ZnO ETL

4. Conclusions

In summary, we have correlated device performance with structural parameters of the ETL films showing that the substrate temperature during the deposition of ZnO influences the performance of HyLEDs. The most important finding is that even at temperatures as low as 250 °C relatively efficient HyLEDs can be obtained. Also, we have confirmed the value of the ZnO ETL in these devices as without this layer the efficiencies are severely lowered. The obtained results provide a promising route for industrial processing of metal oxide thin films. Not only this but the results are applicable to the deposition of inorganic and organic thin films using SPD for a wide range of applications such as transistors and photovoltaic devices.

5. References

1. K. T. Kamtekar, A. P. Monkman and M. R. Bryce, *Advanced Materials*, 2010, **22**, 572-582.
2. F. So and D. Kondakov, *Advanced Materials*, 2010, **22**, 3762-3777.
3. K. Morii, M. Ishida, T. Takashima, T. Shimoda, Q. Wang, M. K. Nazeeruddin and M. Graetzel, *Applied Physics Letters*, 2006, **89**, 183510.

4. D. Kabra, M. H. Song, B. Wenger, R. H. Friend and H. J. Snaith, *Advanced Materials*, 2008, **20**, 3447-3452.
5. N. Tokmoldin, N. Griffiths, D. D. C. Bradley and S. A. Haque, *Advanced Materials*, 2009, **21**, 3475-3478.
6. H. J. Bolink, E. Coronado, J. Orozco and M. Sessolo, *Advanced Materials*, 2009, **21**, 79-82.
7. H. J. Bolink, E. Coronado and M. Sessolo, *Chemistry of Materials*, 2009, **21**, 439-441.
8. M. C. Gwinner, Y. Vaynzof, K. K. Banger, P. K. H. Ho, R. H. Friend and H. Sirringhaus, *Advanced Functional Materials*, 2010, **20**, 3457-3465.
9. G. Reyna-Garcia, M. Garcia-Hipolito, J. Guzman-Mendoza, M. Aguilar-Frutis and C. Falcony, *Journal of Materials Science-Materials in Electronics*, 2004, **15**, 439-446.
10. K. F. Huang, T. M. Uen, Y. S. Gou, C. R. Huang and H. C. Yang, *Thin Solid Films*, 1987, **148**, 7-15.
11. I. Gonzalez-Valls and M. Lira-Cantu, *Energy & Environmental Science*, 2009, **2**, 19-34.
12. H. J. Bolink, E. Coronado, D. Repetto, M. Sessolo, E. M. Barea, J. Bisquert, G. Garcia-Belmonte, J. Prochazka and L. Kavan, *Advanced Functional Materials*, 2008, **18**, 145-150.
13. J. L. vanHeerden and R. Swanepoel, *Thin Solid Films*, 1997, **299**, 72-77.
14. B. S. Ong, C. Li, Y. Li, Y. Wu and R. Loutfy, *Journal of the American Chemical Society*, 2007, **129**, 2750-2751.
15. D. Kabra, L. P. Lu, M. H. Song, H. J. Snaith and R. H. Friend, *Advanced Materials*, 2010, **22**, 3194-3198.

Chapter 7
Conclusions and Outlook

This principle goal of the thesis was to understand the key loss mechanisms in organic and hybrid organic-inorganic solar cells. A secondary goal was consider lower cost and more environmentally friendly methods of fabricating efficient organic and hybrid optoelectronic devices. In both respects, the work presented here has achieved the goals it set out to.

Chapter 3 described the effect of changing the thickness of a squaraine (SQ) donor in a bilayer organic solar cells, and made several interesting observations on the role of MoO_3 in bilayer organic solar cells (OSCs) and suggests that there is a chemical interaction between it and SQ. It was seen that although we fabricated a bilayer device, it actually behaved like a bulk-heterojunction device as opposed to a planar-heterojunction. This implies that care should be taken when studying and modeling bilayer devices, especially those that employ very thin active layers. Regarding the open-circuit voltage (V_{OC}) we found that controlling the thickness of SQ is vital for controlling the V_{OC}. However, increasing thickness also leads to decreasing the fill factor (FF) and short-circuit (J_{SC}) current. The charge density in the active layers observed was very high compared to previous studies on SMOSCs, which could be why SQ chromophores perform so well in OSCs. In our laboratory we have been studying the molecular packing of SQ recently, and it will be interesting to compare these studies with the results presented here, as well as

expand the study to understand the role of molecular properties, in particular morphology, on the electrochemical properties of the molecules when utilized in optoelectronic devices.

Chapter 4 focused on providing a route to removing the use of organic solvents in solution processed organic solar cells. By decreasing the number of peripheral substituents in a water-soluble ZnPc sensitizer, we successfully improved the electronic properties of the molecule allowing charge injection into the C_{60}. This was the first example of a water-soluble donor in organic solar cells, and demonstrates the potential for a cleaner approach to solution processed OSCs. This opens the door for the use of water-soluble molecules in optoelectronic devices and the possibility of processing films from an abundant, low-cost and non-toxic solvent. However certain problems exist that need to be better understood and hopefully overcome. In particular, the absorption of a molecule dissolved in water is significantly less than if it is dissolved in an organic solvent. It seems that this manifests itself in the thin film absorption properties too. To gain more fundamental insights regarding this issue, further detailed study would be highly valuable. Ideally, the latter efforts would also incorporate a incorporate a water-soluble acceptor molecule to form a bulk-heterojuction.

Chapter 5 studied a new and interesting class of hybrid solar cell; quantum dot/organic planar heterojunction devices and set out upon quantitatively measuring the non-geminate recombination dynamics through the use of transient optoelectronic techniques. From the obtained data we applied a model used originally for organic solar cells to reconstruct the current/voltage behavior of the device under illumination. The close fit of the data obtained in comparison with the experimental results illustrates that the open-circuit in these devices is electric field independent and that fast non-geminate recombination is the reason for the low

open circuit voltages observed. Improving the synthesis and film processing of the quantum dots is key to realize higher open-circuit voltages and thus better performing devices. A drawback of the devices employed here is that they use Pb-based quantum dots. Removing the use of Pb from the device is a must for due to its toxicity, but will be challenging as most colloidal quantum dots utilize toxic elements.

Chapter 6 is based on hybrid organic-inorganic light emitting diodes (HyLEDs) employing a ZnO electron transport layer. This ZnO layer had previously been processed using spray pyrolysis at high temperatures, but at these temperatures it is too costly for industry to efficiently and timely produce devices commercially. Therefore we studied the effect of lowering the temperature on the optoelectronic properties of the device and found that it is possible to reduce the temperature by 200 °C and still have rather efficient devices. Although this chapter focused on using the ZnO films for HyLEDs the results are valid for OSCs as well as other technologies utilizing transition metal films. In this study the effect of temperature on the crystalline properties of ZnO was also illustrated and is interesting to consider how the electronic properties also change.

Organic solar cells are continuing to grow in efficiency at a fast rate. In fact, the record OSC efficiency at the time of writing this (May 2013) is double what the record efficiency was when I began my doctoral studies (September 2009). It will be interesting to see how far they can progress in the next four years. One of the deciding factors on this will depend on advancing our knowledge of the fundamental operating principles, as they are still not fully understood. In order for OSCs to reach their full potential then further studies and approaches are therefore required. As described in the introduction and demonstrated in the thesis, organic semiconductors do not behave like inorganic semiconductors and different ways of

characterizing them are thus required. One key factor to be considered is that it is the electrochemical potential (which is the sum of the electrical and chemical potentials) that drives the current-voltage of a solar cell. In a conventional solar cell, the electrical potential drives the cell while in a dye-sensitized solar cell it is the chemical potential that drives the device. Interestingly in OSCs, there seems to be a combination of both the electrical and chemical potential that controls device performance. To what degree each potential influences the cell is still not clearly understood and most likely changes depending on the materials employed, e.g., the choice of electrodes, donor and acceptor molecules, fabrication steps, device architecture, thickness of the active layer, and the choice of selective contacts. We observed some changes in the distribution of charge density in the active layer of the SQ/C_{60} devices in Chapter 3 through increasing the thickness of SQ and also through the addition of a MoO_3 film. Further exploration of the influence of a metal oxide layer on the energetics of the organic active layer could lead to some very interesting observations.

The rapid advances in OSCs has brought the technology ever closer to the market, and will see research shift from more fundamental research to technological research as has happened with organic light emitting diodes (OLEDs). One of the key factors that will need to be addressed as OSCs edge closer to the market is the use of organic solvents in device fabrication. Reducing this need will improve reduce waste managements costs as well as the impact on the environment. Furthermore, encapsulation is another process that adds significant costs to the fabrication of OLEDs and OSCs. The use of an inverted structure that allows the high work function top contacts to be used is extremely interesting from an industrial point of view.

In summary, in the thesis presented here a range of bilayer solar cells were investigated, each with their own intrinsic problems. In each case, insights into the limiting factors were presented and routes towards improved devices efficiencies. Hybrid organic-inorganic devices were also studied, with emphasis on lowering the fabrication temperature in order to realize low-cost fabrication methods. The results of the final study can also be related to organic solar cells and other similar thin film devices.

Acknowledgements

Firstly, I would like to thank my supervisor Prof. Emilio Palomares for allowing me to join his research group four years ago and carry out some new and exciting research. In particular I am grateful for the faith and trust placed in me to go about my business and follow my research interests, even when they involved going to Japan. The experiences gained from the four years at ICIQ will be of great benefit to me when I set out on my independent career in the next few years. For funding I am grateful to ICIQ for providing me with an ICIQ Fellowship.

Moltes gracies to my colleagues in the group for their help and support. It has been a pleasure to share the same lab and clean room as you. Special thanks to the first generation who had the task of setting up everything in the lab. In particular, a special thanks to Josep and Toni for showing me the ropes. On the HyLEDs work, thank you to Eugenia for her supervision and to Amparo for her help and assistance in the experiments (spray pyrolysis, never again). Also thanks Amparo for the Spanish conversation lessons. Regarding language, thanks Laia for helping me learn a bit of Catalan. For the PbS work, a big thanks to Josep and Beloqui, cero punto cero you came good in the end, hopefully when you finish you can become diez punto algo. A big cheers pal to Aurélien for his help in the small molecule projects, I learned a lot about crystal packing as well as growing vegetables. Dani too for the small molecule work and general conversations about everything and nothing. John, thanks for you thoughts, comments and advise during the PhD, it was always good to have an Irish opinion on things. Vijay, thanks for your conversations on small molecule synthesis and round bottom flasks. A massive thank you to our assistants, Eva and Bea for all their support throughout the years. I wouldn't have been able to deal with the endless bureaucratic things alone, that's for sure.

I am very grateful to the research support staff in ICIQ for all there help. Javíer in particular, for setting up, maintaining and improving all the instruments in photophysics that I used during my PhD. Also, thanks for helping me with the problems I had understanding a technique or idea. Fernando in spectroscopic and kinetics, thanks for your assistance with the instruments and offering helpful advice when needed. Yvette and the other members of CRTU, thanks for taking care of the clean room and diligently getting problems sorted, it made my job a lot easier. In the URV, special thanks to Lukas and the girls in the microscopy unit for training me in several of the techniques and for helping me when required. Also, thank you Francesc for your help with us on XRD.

I have had the good fortune to collaborate with several groups, in ICIQ, Spain and abroad during my time at ICIQ. In each case I learned a lot and became a more rounded scientist. I am grateful to Dr. Oscar Custance at NIMS, Japan for hosting me twice in his lab. It was something different and I gained better insights into how molecules behave at the molecular scale. Thank you to Sasha, and Fang-san also. At UAM, thank you Prof. Tomas Torres, Andrés and Eduardo for the work on the water soluble Pcs. At Imperial College, a special thanks to Dr. Thomas Kirchartz and Prof. Jenny Nelson for the help on the SQ study. Also at Imperial, Prof. James Durrant for insightful conversations during the different occasions we met. In UCD, I am indebted to Prof. Gareth Redmond for his advice prior to coming to Spain among and am glad I could help with some measurements here.

To my friends here in Tarragona, two names have to be mentioned first and in alphabetical order to avoid any confrontation.....Monsant and Priorat.....only joking, Danny and Giovanni, the stalloni. You guys kept me sane and allowed me to maintain some sort of social life. I think I may have even become less bitter over time. We had some good nights out and trips away. Danny, now that you are on the verge of earning a big Swiss salary I hope your generosity won't go astray and we can enjoy some more of the dolce vita when you visit me in Japan. Now that you are a fully-fledged member of the best club in town you will have to visit me often. Giovo, you have had to put up listening to me for almost four years, congratulations. There are not many who could do it. Thanks for all the nice food, wine, and taxi rides. I must owe you a fortune. Although, I did help you meet some new "friends" so lets call it quits. So men, I hope we continue our bromage a trois and can manage to meet up often enough.

Those who didn't make it as stalloni for being too old or always in Cullera are Ivan, John, Kian, and Sergio. It was a pleasure to share a house, or a drink and/or travel with you (Torino, Ireland and Krutyn). I'd like to also like to thank John and Ivan for sharing an apartment with me for so long. Although I enjoy my solitude it was good to have some company in general. Really glad we got out of the first house, it was a state (thanks Danny!). Champions league nights (unless Man Utd were playing) were also fun. Also, I'd like to say a bit thanks to all my other friends in Tarragona, in particular the Italian mafiosas, Margherita and Moira. We had some good times, especially in the Cau and at Moira's parties. A special mention to the other Italians girls too that I didn't know as well but still shared some good times with; Caterina, Sara and CarMELA.

To the second group of friends here, ICIQ friends 2.0, thanks for all the fun times and the excellent dinners. Alice, Asraa, Bazzo, Chris, John Murphy, Katya and Ricarda. Chris, your fluency was much appreciated. John had you arrived earlier, Kennedy's might be still open.

During my stay in Japan I also had the pleasure of spending time with my bakas and wagas, Bates, Iain, Momoko and Risa. Can't beat a good night out with you guys, as long we take care to mind the gap or avoid keeping up with Johnboy. They were also fun as usual and I look forward to continuing them. I also appreciate my furture in-laws hospitality at the weekends, making me feel right at home.

Also, I'd like to thank my friends back in Greystones, who I didn't get home enough to see, especially the lads from St. David's, Chris, Conor, David and Richard, for all the laughs and piss taking over the years. I think when we are old men sitting in Dann's we will still be talking the same rubbish.

If it wasn't for my parents love and support, not to mention the endless hours of Lego when I was a child, then I would not be here writing acknowledgements at the end of a thesis. I was always made feel clever and that I can achieve anything if I put my mind to it. Well I learned that is not always the case, as I should be playing for Man Utd now, or earning a living on the PGA tour.....But when it came to academic things I always felt confident and as though nothing was beyond me. Thank you for always being there for me and for believing in me! To my brother Paul, thanks for being a good brother to me, even when I didn't deserve it (after winning three games in a row in Fifa, for example). You have a big task this year to show me that you are the best man. I am sure you will be.

To finish, Asami thanks for sticking with me all these years. It's been a long wait but finally it is done and we can focus on the next chapter of our lives together.

Scientific Contributions

Published Articles

J. W. Ryan, E. Palomares and E. Martinez-Ferrero, *Journal of Materials Chemistry*, 2011, **21**, 4774-4777

J. W. Ryan, E. Anaya-Plaza, A. d. l. Escosura, T. Torres and E. Palomares, *Chemical Communications*, 2012, **48**, 6094-6096.

A. Viterisi, F. Gispert-Guirado, J. W. Ryan and E. Palomares, *Journal of Materials Chemistry*, 2012, **22**, 15175-15182.

Articles Ready for Submission

J.W. Ryan, J.M Marin-Beloqui, J. Albero, E. Palomares, "On the origin of the open-circuit voltage in hybrid PbS quantum dot / C60 bilayer solar cells"

J.W. Ryan, T. Kirchartz, A. Viterisi, J. Nelson, E. Palomares "The Effect of Donor layer thickness and a MoO_3 transport layer on device performance in squaraine/C_{60} bilayer solar cells"

J.C. Nolasco, J.W. Ryan, M. Rodriguez, G.R. Ortiz, J.L Maldonado, O. Barosa-Garcia, E. Palomares "Organoboron donor-π-acceptor based small molecule organic solar cells"

D.Fernandez Pinto, A. Viterisi, J.W. Ryan, S. Fillipone, N. Martin, E.Palomares, "DPM-based DPP(TBFu)2 small molecule BHJ solar cells: linking morphology, transport and crystallinity"

Scientific Meetings

J.W. Ryan, E.A. Plaza, A. de la Escosura, T. Torres, E. Palomares, "Small molecule solar cells based on water soluble ZnPc donors",
Personal presentation to *Nobel Laureate* Prof. Ryoji Noyori, *CEICS Nobel Campus*, La Pineda, Spain, 2012

J.W. Ryan, E.A. Plaza, A. de la Escosura, T. Torres, Emilio Palomares, "Small molecule solar cells based on water soluble ZnPc donors", *VIII International Summer School Krutyn,* 2011

J.W. Ryan, E. Palomares, "Hybrid organic-inorganic electronics", National Institute of Material Science, Japan, 2010

J.W. Ryan, E. Martinez-Ferrero, E. Palomares, "Hybrid organic-inorganic light-emitting diodes, *VII International Summer School Krutyn,* 2010

UNIVERSITAT ROVIRA I VIRGILI
ORGANIC AND HYBRID OPTOELECTRONIC DEVICES: UNDERSTANDING KEY LOSS MECHANISMS.
James William Ryan
Dipòsit Legal: T 277-2015

UNIVERSITAT ROVIRA I VIRGILI
ORGANIC AND HYBRID OPTOELECTRONIC DEVICES: UNDERSTANDING KEY LOSS MECHANISMS.
James William Ryan
Dipòsit Legal: T 277-2015